

# g12 Analysis Procedures, Statistics and Systematics

Z. Akbar      R.A. Badui      J. Bono      C. Bookwalter      S. Chandavar  
V. Crede      P. Eugenio      J.T. Goetz      L. Guo      K. Hicks      V. Kubarovskiy  
M.C. Kunkel      M. Paolone      W. Phelps      J.W. Price      M. Saini  
C. Salgado      D. Schott      D.P. Weygand      C. Zeoli

July 19, 2016

## Contents

<b>1</b>	<b>Summary of Running Conditions</b>	<b>3</b>
1.1	Trigger Configurations	4
1.2	Lists of Runs	7
<b>2</b>	<b>Calibration and Detector Performance</b>	<b>12</b>
2.1	Trigger Rates	12
2.2	Tagger Timing Calibration	13
2.3	Target Density	13
2.4	Start Counter Calibration and Resolution	16
2.4.1	Start Counter Efficiency	21
2.5	Drift Chamber Calibration and Resolution	24
2.5.1	Drift Chamber Wire Efficiency	24
2.6	Cerenkov Calibration and Performance	26
2.6.1	Cerenkov Efficiency	26
2.7	Time-of-Flight Counter Calibration and Resolution	28
2.7.1	Time-of-Flight Counter Efficiency and Bad Paddles	29
2.7.2	ADC and TDC Values	31
2.7.3	Time-of-Flight Paddle Resolution	38
2.8	Electromagnetic Calorimeter Calibration and Resolution	40
2.8.1	Electromagnetic Calorimeter Efficiency and Bad Paddles	42
2.9	Beam Polarization	58
<b>3</b>	<b>Procedure for Data Analysis</b>	<b>62</b>
3.1	“Pass1” Cooking and Data Reconstruction	63
3.2	Obtaining Reconstructed Data	63
3.3	g12-Specific Corrections	65
3.3.1	Final-State Particle Momentum Corrections	65

3.3.2	Photon Tagger Calibration and Beam Energy Corrections . . . . .	69
3.4	General Features of Lepton Data in <i>g12</i> . . . . .	82
3.4.1	CC Comparison . . . . .	83
3.4.2	EC Comparison . . . . .	85
<b>4</b>	<b>Flux Determination</b>	<b>88</b>
4.1	Beam Trips . . . . .	90
4.2	Normalized Yields for Different Beam Conditions . . . . .	90
4.3	Run-by-run Stability and Systematic Uncertainty of Flux . . . . .	90
<b>5</b>	<b>Simulations</b>	<b>93</b>
5.1	Generating Events for Digitization . . . . .	94
5.2	Digitization and Smearing . . . . .	95
5.3	Fiducial Region Selection . . . . .	101
5.4	Reconstruction of Simulated Data . . . . .	105
5.5	Simulating the Lepton Trigger . . . . .	106
5.5.1	Validity of Trigger Simulation . . . . .	107
<b>6</b>	<b>Comparison of Data to Known States and Cross Sections</b>	<b>107</b>
6.1	Track dependent inefficiency correction . . . . .	107
6.2	Comparison of Data to Known Cross Sections . . . . .	114
<b>References</b>		<b>124</b>

## Abstract

This document serves to summarize all information needed to process and analyze data from the CLAS *g12* experiment taken in the summer of 2008. This was a high-luminosity, high-energy real-photon run with a 65 nA circularly polarized beam, 40 cm unpolarized  $\ell\text{H}_2$  target and an  $E_{\text{beam}}$  up to 5.7 GeV. The associated proposals, and therefore the trigger, focused on the high-energy part of the tagger, and though it was not part of the original proposals, the Cerenkov was active for most of the run.

## 1 Summary of Running Conditions

This document is organized as follows. Section 1 has basic information about the *g12* run, including the physics goals. Section 2 describes the calibrations; it is quite long and uses standard CLAS procedures. One item of note is that the beam current was high for CLAS, typically about 60 nA. Of course, the background rate goes quadratically with beam current, and so the *g12* data have more background yet the calibration procedures still work. Section 3 provides the cooking procedures, as well as the momentum and beam-energy corrections. Since *g12* also had a lepton trigger, Section 3.4 gives additional information relevant to the lepton detection using the CC and EC. Section 4 has a straight-forward description of the beam flux, using the `gf1ux` method with the `-c` option (clock-based DAQ). Section 5 provides the procedures for simulations, including all command-line options (some `a1c` options are specific to BOS files made from simulations). This section also has specific information for *g12*, such as the fiducial cuts and simulations of the *g12* trigger. Finally, Sections 6 and 6.2 together present a few selected cross section results which agree well with previously reported world data. This gives us confidence that the calibrations, energy corrections, beam flux and simulations are being done correctly.

The goal of this document is to provide a basis for individual analyses of *g12* data to undergo a shortened analysis review. In other words, if the procedures here are followed also in individual analyses, then the review committees can focus on the cuts and systematics specific to the final state of an individual analysis, with confidence that the calibrations, corrections, etc., have already been reviewed.

The *g12* experiment contained several analyses where the main goal was to search for resonances in the multi-particle final state by performing partial wave analysis. These analyses[1, 2] do not require absolute normalization and therefore several steps discussed below were skipped. For a general discussion of the PWA procedure by *g12* Ref. [3]. We do however provide details for analyses that do want this normalization for cross sections and upper limits later in this document.

The *g12* experiment was a high-luminosity, high-energy real-photon run for CLAS. The electron beam current was 60–65 nA on the 40 cm  $\ell\text{H}_2$  target. A total of  $26 \times 10^8$  triggers were recorded using several of the 12 available trigger bits. The “production trigger” required two prongs (start-counter and time-of-flight coincidence) in two different sectors and in coincidence with a tagger hit at or above 3.6 GeV. There was secondary trigger which required three prongs, again in different sectors, regardless of tagger hits. The running conditions are summarized in Table 1. There were three proposals associated with this experiment which are listed here:

- P. Eugenio et al. *Search for New Forms of Hadronic Matter in Photoproduction*. Tech. rep. CLAS Analysis Proposal PR04-005, 2003
- D. Weygand et al. *Study of Pentaquark States in Photoproduction off Protons*. Tech. rep. CLAS Analysis Proposal PR04-017, 2004

- W. Chen et al. *The  $\gamma p \rightarrow \pi^+ n$  Single Charged Pion Photoproduction*. Tech. rep. CLAS Analysis Proposal PR08-003, 2008

In addition to this document, there is a wealth of information to be found in the wiki pages at

<http://clasweb.jlab.org/rungroups/g12/wiki>

which has served as a repository for all things related to the *g12* experiment. The dissertations associated with this experiment contain a lot of information as well:

- John T. Goetz. “ $\Xi$  Hyperon Photoproduction from Threshold to 5.4 GeV with the CEBAF Large Acceptance Spectrometer”. PhD thesis. University of California Los Angeles, 2010
- Craig Bookwalter. “A Search for Exotic Mesons in  $\gamma p \rightarrow \pi^+ \pi^+ \pi^- n$  with CLAS at Jefferson Lab”. PhD thesis. Florida State University, 2012
- Diane Schott. “A Search for an Exotic Meson in the  $\gamma p \rightarrow \Delta^{++} \pi^- \eta$  Reaction”. PhD thesis. Florida International University, 2012
- Mukesh Saini. “Search for New and Unusual Stangonia using CLAS”. PhD thesis. Florida State University, 2013
- Jason Bono. “First Time Measurements of Polarization Observables for the Charged Cascade Hyperon in Photoproduction”. PhD thesis. Florida International University, 2014
- Michael C. Kunkel. “Photoproduction of  $\pi^0$  on hydrogen with CLAS from 1.1 GeV - 5.45 GeV using  $e^+ e^- \gamma$  decay”. PhD thesis. Old Dominion University, 2014
- Shloka Chandavar. “Photoproduction of Scalar Mesons Using the CEBAF Large Acceptance Spectrometer (CLAS)”. PhD thesis. Ohio University, 2015

## 1.1 Trigger Configurations

The *g12* experiment was the first Hall *B* run-period to implement field programmable gate array (FPGA) processors to handle the trigger logic of the CLAS detector. With this new FPGA-powered triggering system, came the ability to modify the trigger quickly during the experiment. While potentially dangerous — these changes must be accounted for in total-cross-sectional analyses for example — this allowed the group to tune the trigger to get the highest possible rate of physical events.

The trigger bits used during the *g12* running period are defined in Tables 2, 3 and 4. They generally consisted of a number of tracks which were the coincidence of any one of the four start counter paddles and any of the 57 time-of-flight paddles in a given sector. The hardware and configuration did not allow triggering on two tracks in the same sector because there were only six signals coming from the TOF — one for each sector. The coincidence of these tracks with the photon tagger, called the “Master-OR,” is defined in Table 5.

There were two sets of thresholds for the EC labeled *photon* and *electron*. These labels did not mean photon or electron specifically, but were considered a first-order approximation. The actual particle identification was done much later in the analysis of the reconstructed data. The thresholds for the CC and EC during the *g12* running period are shown in Table 6.

**Table 1:** The running conditions of the *g12* experiment.

$E_{\text{beam}}$ of photon	5.715 GeV
Beam Polarization	Circular
e <sup>-</sup> Current	60–65 nA
Tagger Range	5% - 95% of e <sup>-</sup> energy
Tagger Trigger Range	3.6–5.441 GeV
Torus Magnet	$\frac{1}{2}B_{\max}$ (1930 A)
Target Length	40 cm
Target Center ( <i>z</i> location)	−90 cm
Target Material	$\ell\text{H}_2$
Target Polarization	None
Start Counter Offset	0 cm
Radiator Thickness	$10^{-4}$ radiation lengths
Collimator Radius	6.4 mm

**Table 2:** Trigger configuration for *g12* runs from 56363 to 56594 and 56608 to 56647.  $(\text{ST}\times\text{TOF})_i$  indicates a single *prong* which is a trigger-level track defined as a coincidence between a start counter and time-of-flight hit in the *i*<sup>th</sup> sector or any sector if the subscript index, *i*, is not specified. An added  $\times 2$  or  $\times 3$  indicates the coincidence of multiple *prongs* which are not in the same sector. MORA and MORB represent coincidences with tagger hits within a certain energy range as specified in Table 5.

g12 runs 56363–56594, 56608–56647			
bit	definition	L2 multiplicity	prescale
1	MORA·( $\text{ST}\times\text{TOF})_1$ ·( $\text{ST}\times\text{TOF}$ )	—	1
2	MORA·( $\text{ST}\times\text{TOF})_2$ ·( $\text{ST}\times\text{TOF}$ )	—	1
3	MORA·( $\text{ST}\times\text{TOF})_3$ ·( $\text{ST}\times\text{TOF}$ )	—	1
4	MORA·( $\text{ST}\times\text{TOF})_4$ ·( $\text{ST}\times\text{TOF}$ )	—	1
5	MORA·( $\text{ST}\times\text{TOF})_5$ ·( $\text{ST}\times\text{TOF}$ )	—	1
6	MORA·( $\text{ST}\times\text{TOF})_6$ ·( $\text{ST}\times\text{TOF}$ )	—	1
7	ST×TOF	—	1
8	MORA·( $\text{ST}\times\text{TOF}$ ) $\times 2$	—	1
11 <sup>a</sup>	MORB·( $\text{ST}\times\text{TOF}$ ) $\times 2$	—	1
12	( $\text{ST}\times\text{TOF}$ ) $\times 3$	—	1

<sup>a</sup>bit 11 and MORB were included in the trigger starting with run 56519.

**Table 3:** Trigger configuration for  $g12$  runs from 56595 to 56607 and 56648 to 57323. (EC $\times$ CC) represents a coincidence between the electromagnetic calorimeter and the Čerenkov subsystems within a single sector using the thresholds as described in Table 6. ECP represents the *photon* threshold trigger from the EC. See Table 2 for other explanatory details.

$g12$ runs 56595–56607, 56648–57323			
bit	definition	L2 multiplicity <sup>a</sup>	prescale
1	MORA·(ST $\times$ TOF)	1	1000/300 <sup>b</sup>
2	MORA·(ST $\times$ TOF) $\times 2$	2/ <sup>c</sup>	1
3	MORB·(ST $\times$ TOF) $\times 2$	2	1
4	ST $\times$ TOF	1	1000/300
5	(ST $\times$ TOF)·ECP $\times 2$	1	1
6	(ST $\times$ TOF)·(EC $\times$ CC)	2	1
7	MORA·(ST $\times$ TOF)·(EC $\times$ CC)	—	1
8	MORA·(ST $\times$ TOF) $\times 2$	—	1
11	(EC $\times$ CC) $\times 2$	—	1
12	(ST $\times$ TOF) $\times 3$	—	1

<sup>a</sup>Level 2 triggering was turned off on all bits for runs 56605, 56607 and 56647.

<sup>b</sup>Prescaling for bits 1 and 4 were 1000 for runs prior to 56668 at which point they both were changed to 300.

<sup>c</sup>Level 2 triggering of bit 2 was set to 2 for runs prior to 56665 at which point it was turned off.

**Table 4:** Trigger configuration for the single-sector runs of  $g12$ . Trigger bits 7–12 were not used for these runs. See Table 2 for explanatory details.

bit	definition	L2 multiplicity	prescale
1	MORA·(ST $\times$ TOF) <sub>1</sub>	sector 1	1
2	MORA·(ST $\times$ TOF) <sub>2</sub>	sector 2	1
3	MORA·(ST $\times$ TOF) <sub>3</sub>	sector 3	1
4	MORA·(ST $\times$ TOF) <sub>4</sub>	sector 4	1
5	MORA·(ST $\times$ TOF) <sub>5</sub>	sector 5	1
6	MORA·(ST $\times$ TOF) <sub>6</sub>	sector 6	1

**Table 5:** Master-OR definitions for *g12*. The TDC counters were used in the trigger and since each of these corresponds to several energy paddles, the energies given here are approximate. *T*-counter number 1 corresponds to the highest energy photon of approximately 5.4 GeV. Both MORA and MORB are referenced in terms of the trigger logic in Tables 2, 3 and 4. The *single-sector* runs are listed in Table 8.

run range	MORA		MORB	
	<i>T</i> -counters	energy (GeV)	<i>T</i> -counters	energy (GeV)
56363–56400	1–47	1.7–5.4	–	–
56401–56518	1–25	3.6–5.4	–	–
56519–57323	1–19	4.4–5.4	20–25	3.6–4.4
<i>single-sector</i>	1–31	3.0–5.4	–	–

**Table 6:** Threshold values for the electromagnetic calorimeter (EC) and Čerenkov counter (CC) during the *g12* running period. EC thresholds are shown as *inner/total*, and CC thresholds are shown as *left/right*.

EC		CC
<i>photon</i>	<i>electron</i>	
50/100 mV	60/80 mV	20/20 mV
150/300 MeV	180/240 MeV	~0.4 photo-electrons

## 1.2 Lists of Runs

The runs for this experiment range from 56855 to 57317 inclusive. The runs that made it into Tables 7 and 8 qualified upon success of reconstructing final-state hadrons using the cooking program’s default particle identification in coordination with the hand-written notes by the shift takers. Other runs of note include those used specifically for calibration in Table 9 and normalization, zero-field and empty-target runs in Table 10.

**Table 7:** List of successfully reconstructed production runs and their beam currents in nA.

runs current (nA)	runs current (nA)	runs current (nA)
56363 20	56605 60	56900–56908 60
56365 30	56608–56612 60	56914–56919 60
56369 30	56614–56618 60	56921–56922 60
56384 5	56620–56628 60	56923 65
56386 20	56630–56636 60	56924 70
56401 50	56638–56644 60	56925 80
56403 70	56646 60	56926–56930 60
56404 60	56653–56656 60	56932 60
56405 50	56660–56661 60	56935–56940 60

continued on next page.

continued from previous page.

runs current (nA)	runs current (nA)	runs current (nA)
56406 40	56665-56670 60	56948-56956 60
56408 80	56673-56675 60	56958 60
56410 90	56679-56681 60	56960-56975 60
56420-56422 5	56683 60	56977-56980 60
56435 5	56685-56696 60	56992-56994 60
56436 15	56700-56708 60	56996-57006 60
56441 35	56710-56724 60	57008-57017 60
56442 30	56726-56744 60	57021-57023 60
56443 20	56748-56750 60	57025-57027 60
56445-56450 60	56751-56768 65	57030-57032 60
56453-56459 60	56770-56772 65	57036-57039 60
56460-56462 70	56774-56778 65	57062-57069 60
56465 70	56780-56784 65	57071-57073 60
56467-56472 70	56787-56788 65	57075-57080 60
56478-56483 70	56791-56794 65	57095-57097 60
56485-56487 70	56798-56802 65	57100-57103 60
56489-56490 70	56805-56815 65	57106-57108 60
56499 70	56821-56827 65	57114-57128 60
56501 60	56831-56834 65	57130-57152 60
56503 57	56838-56839 65	57159-57168 60
56504 56	56841-56845 65	57170-57185 60
56505-56506 40	56849 65	57189-57229 60
56508-56510 60	56853-56862 65	57233-57236 60
56513-56517 60	56864 65	57249-57253 60
56519 60	56865-56866 60	57255-57258 60
56521-56542 60	56870 65	57260-57268 60
56545-56550 60	56874-56875 60	57270-57288 60
56555-56556 60	56877 60	57290-57291 60
56561-56564 60	56879 60	57293-57312 60
56573-56583 60	56897-56898 60	57317 60
56586-56593 60	56899 65	

**Table 8:** A list of the single-sector runs using the trigger configuration described in Table 4.

run	current (nA)	run	current (nA)
56476	24	56910	35
56502	24	56911	30
56520	24	56912	25
56544	24	56913	24
56559	24	56933-4	24
56585	24	56981-3 <sup>a</sup>	24
56619	24	56985 <sup>a</sup>	15
56637	24	56986	15
56663-4	24	56989	24
56697	24	57028	24
56725	24	57061	24
56747	24	57094 <sup>b</sup>	24
56769	24	57129	24
56804	24	57155-6	24
56835	24	57237-8	24
56869	5		

<sup>a</sup>No Level-2 trigger was used for runs 56981-56985<sup>b</sup>A shorter ST ADC gate was implemented starting with run 57094.

**Table 9:** A list of the runs which were calibrated for the subsystems: tagger (TAG), start counter (ST), and time-of-flight (TOF). The calibrations were committed into the database for the range starting with the run shown and ending with the run just prior to the next listed run. A brief reason for calibration is given in the last column.

run	systems affected	reason
56363	TAG, ST, TOF	start of run
56503	ST	ST adjustment
56508	"	" "
56661	TAG, ST, TOF	trigger and ST changes
56663	"	" "
56665	"	" "
56666	"	" "
56670	TAG	vacuum problem in tagger fixed
56673	TAG, ST, TOF	trigger change
56732	"	RF related problems fixed by Accelerator group
56765	TAG	T20 left HV problem
56766	"	T20 left HV adjusted
56782	TAG, ST, TOF	changes in calibration database
56855	"	" "
56923	"	start of intensity studies
57094	"	changes in calibration database
57154	ST	adjusted ST ADC timing in gate

**Table 10:** List of special calibration runs done during the *g12* experiment.

run	current (nA)	description
56397	0.05	normalization
56475	10	zero-field
56511	0.05	normalization, tagger TDC-left
56512	0.05	normalization, tagger TDC-right
56584	0.05	normalization
56682	0.05	normalization
56790	0.05	normalization
56931	0.05	normalization
56947	0.05	normalization

continued on next page.

continued from previous page.

run	current (nA)	description
57169	0.05	normalization
57239	24	empty-target, single-sector
57241	80	empty-target, production
57248	0.05	normalization

A script named “g12runs” was created to provide a list of the runs which were fully reconstructed without errors. It can also provide a lot of information about each run including the beam current, the number of good scalar intervals, and the run type such as production, calibration, or single-sector. The script resides in the *clasg12* user’s home directory here:

```
/home/clasg12/local/scripts/g12runs
```

and has an extensive help message with the “-h” as shown here:

```
>/home/clasg12/local/scripts/g12runs -h
Usage:      usage: g12runs [options]

example to get all good data runs:
g12runs -t prod -t single -x calib

to get all data runs (prod and single) that have
been completely cooked, sorted and have complete
flux information:
g12runs -t pass1 -t flux -i

Options:
-h, --help          show this help message and exit
-r RANGE, --range=RANGE
                    range of runs to print out (inclusive from:to) To get
                    the six-digit run numbers, use this range:
                    557313:557316. Can also be a single run number.
                    default: 56363:557316
-c CURRENT, --current=CURRENT
                    range of currents to print out (inclusive from:to).
                    examples: 40:80, 20:35 default: 0:90
-t RUNTYPE, --run-type=RUNTYPE
                    Type of runs to print out. can be any of the
                    following, and may be specified more than once: prod
                    single calib cc dc norm pass1 flux Note: calib
                    includes all norm runs. Use prod, single and calib to
                    get all runs. default: prod, single
```

```

-x EXCLUDE, --exclude-type=EXCLUDE
    excludes types from being printed out. may be
    specified more than once.

-i, --intersect
    require all run types specified with the -t option to
    be valid. Note: "g12runs -tprod -tsingle -i" will
    result in no output since prod and single run types
    are mutually exclusive. Typical usage is to get runs
    that have complete pass1 and flux data: "g12runs
    -tpass1 -tflux -i".

-e, --extra-info
    print extra information for each run.

-m, --max-ind
    print maximum index for each run printed.

-n, --nfiles
    print number of files for each run printed.

-s SET, --set=SET
    print runs which correspond to one (or all by default)
    of ten groups: 1 - 10. These groups represent
    approximately 10% of the whole run period.

-a, --scalar
    Print out the number of scalar intervals in the form:
    good/total.

-d, --dump
    Dump all info about all runs.

```

## 2 Calibration and Detector Performance

The calibration of the raw data was done through seven incomplete but representative passes labeled `pass0_v1` through `pass0_v7` though only the last three of these is still available via JLab’s mass storage system (`mss`). All calibration constants were put into the `calib_user.RunIndexg12` run index with the exception of certain lepton-specific numbers as discussed in Sec. 3.4.

### 2.1 Trigger Rates

In the first few weeks of *g12*, during “commissioning,” an attempt to determine the efficiency of the two-track trigger (bit 8 in Tables. 2 and 3) was made. The rate of this main production trigger rose quadratically with the beam current while the physical event rate increased linearly. The number of accidentals, which must be cut from any analysis, increased with increasing current and at a certain point, the majority of the events taken were accidentals. The trigger rate as a function of the beam current is shown in Fig. 1. An estimate of the linear part of the trigger rate shows that approximately 60% of the events recorded during the *g12* experiment (which ran at 60–65 nA beam current) were accidentals.

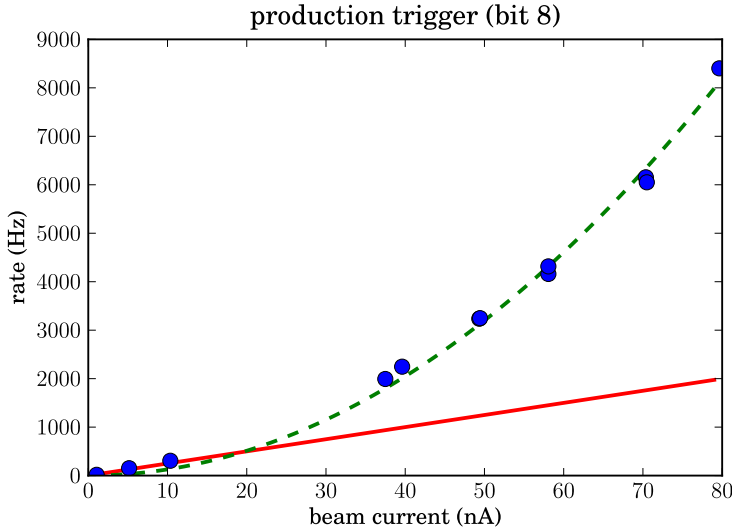


**Figure 1:** The production trigger rate (bit 8 in Tables 2 and 3) was measured for various beam currents shown by the blue dots. The rates below 10 nA are roughly linear and are extrapolated via the red solid line to show an estimate of the physical event rate. The actual trigger rate is fitted with a quadratic shown by the green dashed line. By this estimate, the accidental rate is shown to equal the physical event rate at approximately 40 nA. The *g12* experiment was done at 60–65 nA.

## 2.2 Tagger Timing Calibration

The timing calibration of the tagger system was performed using the standard procedures. Overall, the quality of the calibration is excellent, showing an overall timing resolution of about 130 ps, when the tagger time is compared with the RF time. The counter-by-counter alignment can be seen on Fig. 2. The calibration was checked on a run by run basis (Fig. 3), and new constants were commissioned when major changes were noticed.

Notice the steps in resolution for the tagger timing is 160 ps before about run 56650 and 130 ps afterwards. This is due to a change in the production trigger, which shifted trigger preference to higher energy photons. The high energy T-counters have better resolutions which explains this shift.

## 2.3 Target Density

We need to know the target density to calculate the differential cross-section. The procedure for determining the density of  $\ell\text{H}_2$  target in CLAS has already been established[12]. In the *g12* experiment, the target temperature and pressure was measured periodically during each run. Each run contained at least 3 measurements of the pressure and temperature. The formula for calculating the target density is:

$$\rho = a_1 T^2 + a_2 P + a_3, \quad (1)$$

where  $T$  and  $P$  represent the temperature and pressure respectively and  $a_1$ ,  $a_2$ ,  $a_3$  are constants given in Tab. 11 taken from Ref. [12]. Fig. 4 shows the average target density,  $\bar{\rho}$ , for each run along with the  $\sqrt{\sigma^2}$ .

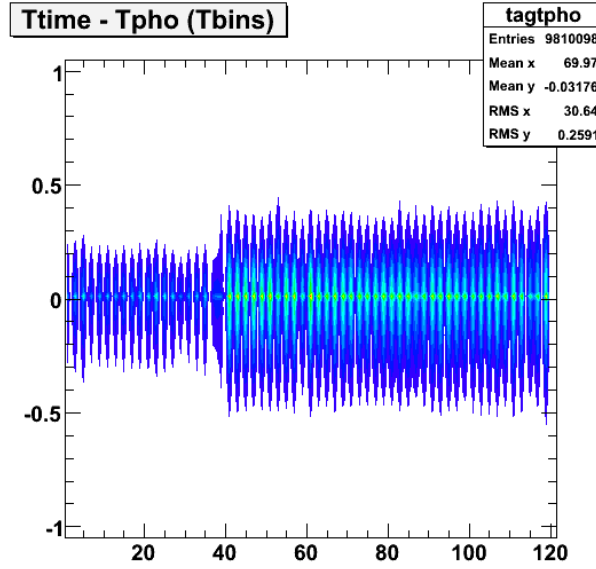


**Figure 2:** An example of the tagger timing calibration and the T-counter alignment, comparing the difference between photon time determined from the tagger elements (T-counters, in this particular plot), and photon timing according to the RF. The relative intensity of the paddles shown are due to the trigger configuration, see Tables. 3 and 5.

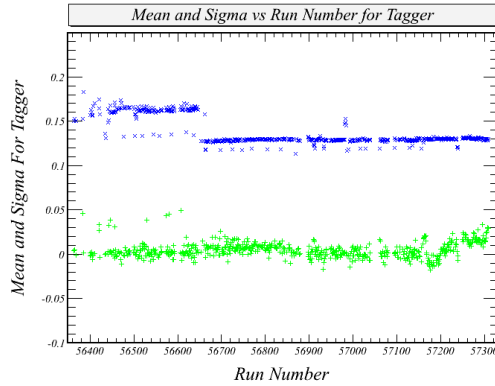


**Figure 3:** The run-by-run behavior of the tagger timing calibration where the mean is in green and the sigma is in blue. Overall, the tagger timing resolution is about 130 ps for the production runs, and the mean behaves stably throughout the running period.

**Table 11:** Constants used in target density measurements

Parameter	Value
$a_1$	$-2.89 \cdot 10^{-5} \frac{g}{cm^3 K^2}$
$a_2$	$1.0 \cdot 10^{-7} \frac{g}{cm^3 mbar}$
$a_3$	$8.249 \cdot 10^{-2} \frac{g}{cm^3}$

The average density, for each run, was calculated as;

$$\bar{\rho}_{run} = \frac{1}{N} \sum_i^N \rho_i, \quad (2)$$

while the variance  $\sigma^2$  is calculated, for each run, as;

$$\sigma^2 = \frac{1}{N - 1} \sum_i^N (\rho_i - \bar{\rho})^2. \quad (3)$$

Once the target density was calculated for each run, the average target density for all *g12* runs was calculated using;

$$\bar{\rho}_{tot} = \frac{1}{N_{run}} \sum_i^{N_{run}} \bar{\rho}_{run} = 0.0711398 \pm 1.74 \cdot 10^{-5}, \quad (4)$$

while the variance  $\sigma^2$  is calculated, for all *g12* run, as;

$$\sigma_{tot}^2 = \frac{1}{N_{run} - 1} \sum_i^{N_{run}} (\bar{\rho}_{run} - \bar{\rho}_{tot})^2 = 0.00024. \quad (5)$$

Since the uncertainty,  $\sigma$ , in the target density is lower than the uncertainty of the physical dimensions in the target materials, the target density uncertainty will not be a factor in the total systematic uncertainties.

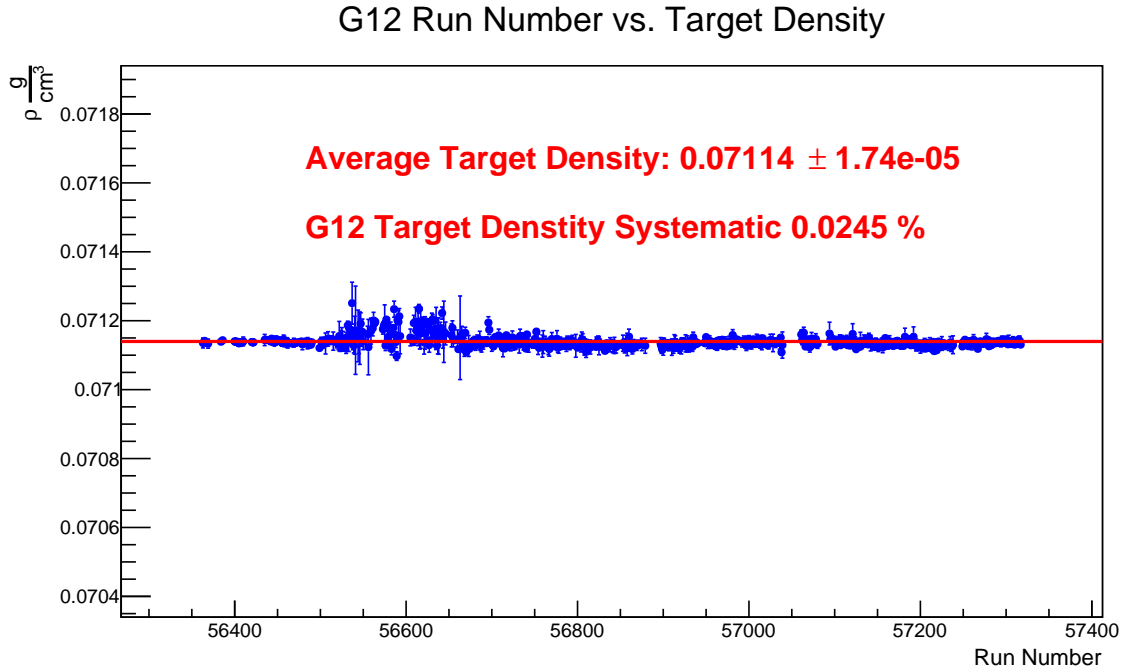
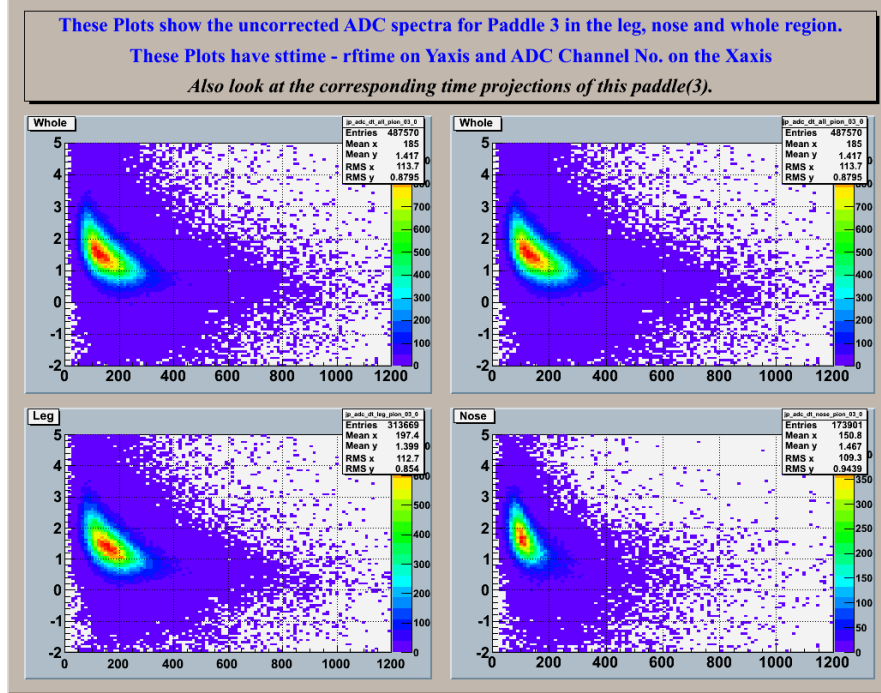


**Figure 4:** Target density for g12. Image source: [10]

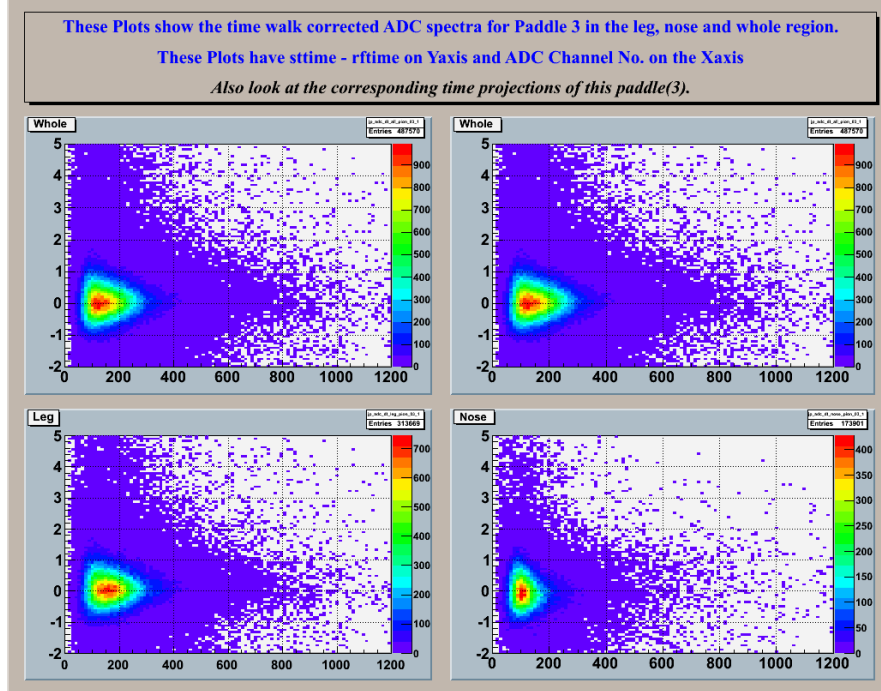
The systematic uncertainties relating to the target in fact also must account the effect such as the contraction, length, etc. Prior experiments such as eg2 have already established that the overall related effect is about 1% [13], which is also what g12 would use for the overall systematic uncertainty related to target. We do not see that there is any statistical significant data from the target cell walls, and do not subtract a background from the target cell walls. Standard g12 analysis should choose events from within the target, taking into account the contraction. If a particular analysis chose to cut outside of the target, they would have to do the systematics study accordingly.

## 2.4 Start Counter Calibration and Resolution

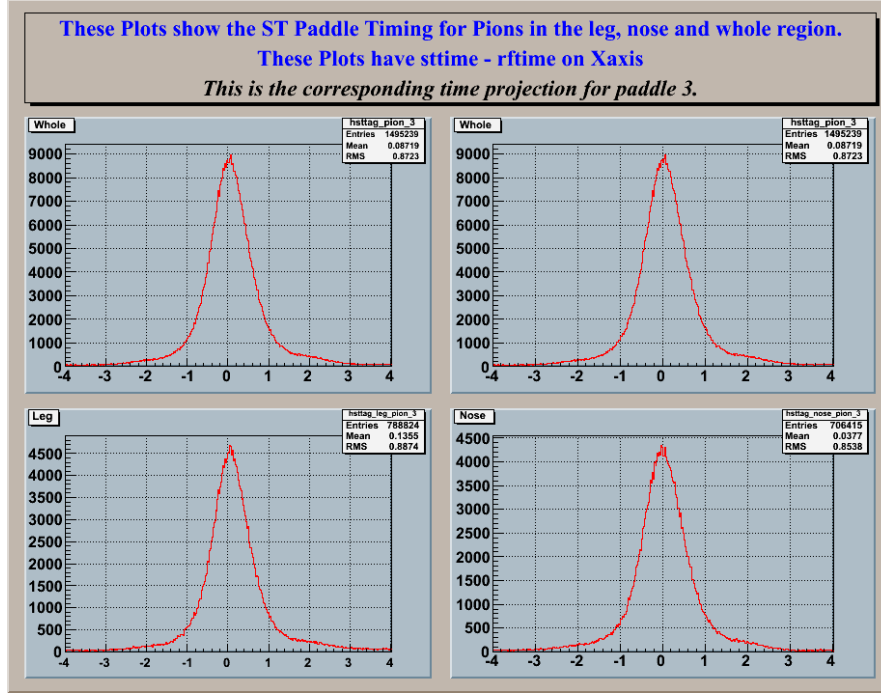
The start counter time-walk calibration took into account the varying geometry of the paddles. Fig. 5 shows the uncorrected timing difference for paddle 3 (of 24) as a function of ADC while Fig. 6 shows the corrected timing. This was done for each paddle and the resulting resolutions can be seen in Fig. 7 for pions, Fig. 8 for protons, Fig. 9 for pions and all paddles, Fig. 10 for pions a function of beam energy and Fig. 11 for pions as a function of geometry. The run-by-run resolution can be seen in Fig. 12. This shows that the start counter was calibrated properly.



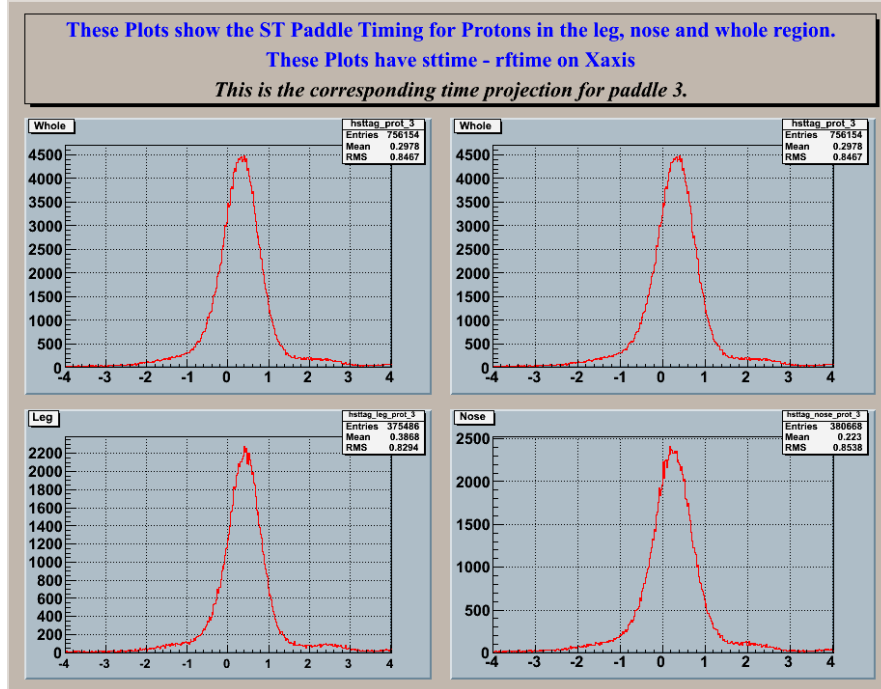
**Figure 5:** ADC spectra for a paddle in the start counter. The top two plots are identical and show the all hits in the paddle. The bottom left plot shows hits in the “leg” of the counter and the bottom right shows hits in the “nose.”



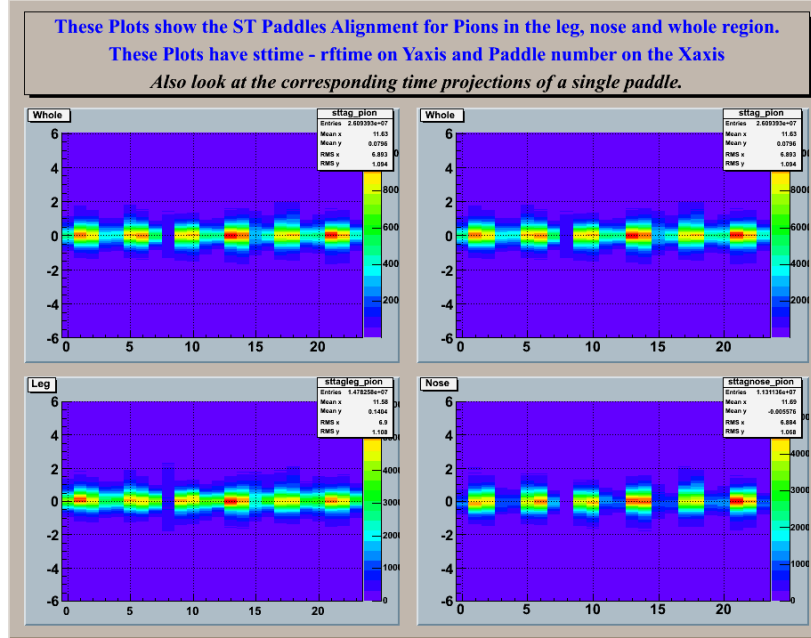
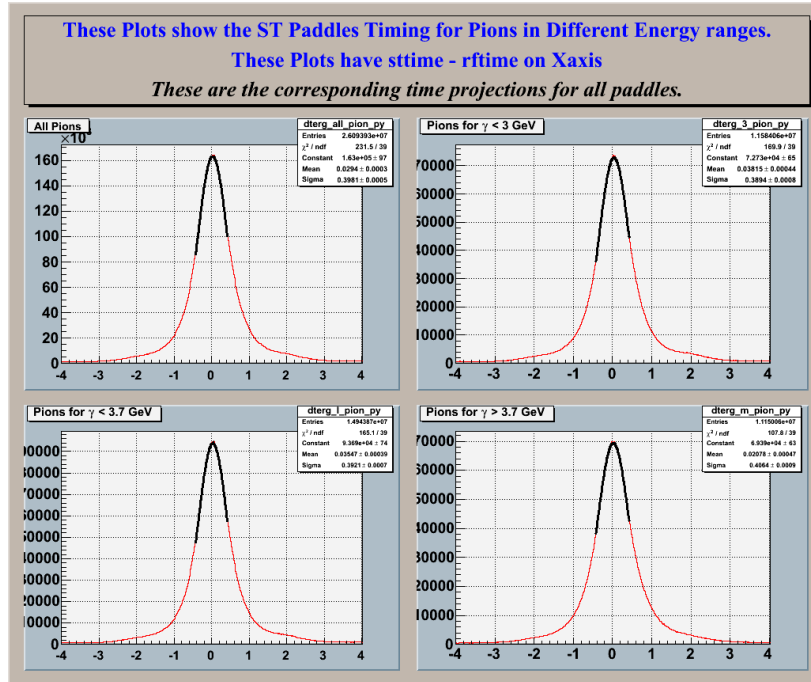
**Figure 6:** See caption above and caption in Fig. 5.

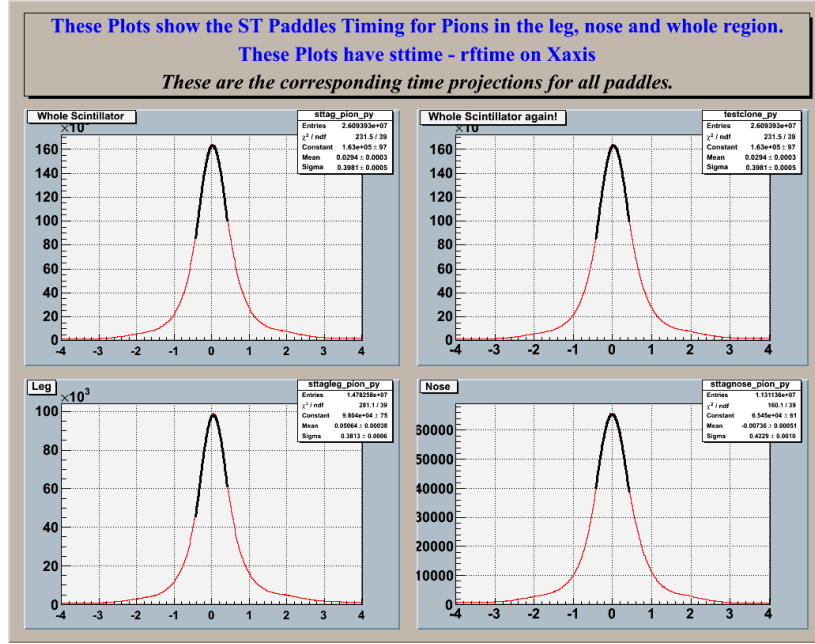
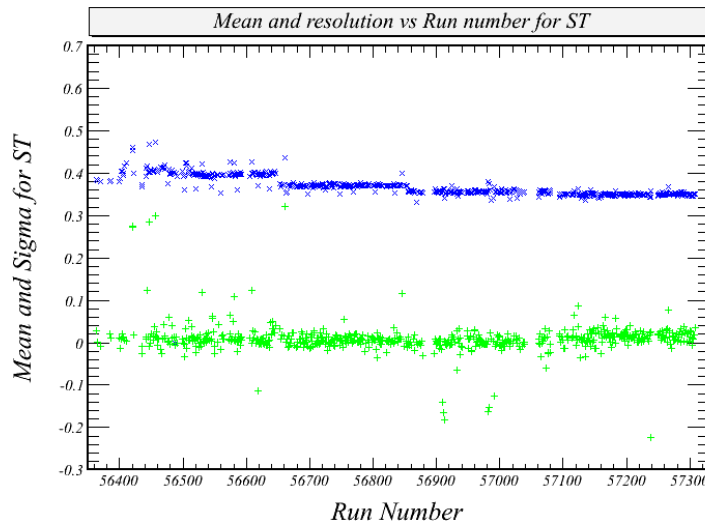


**Figure 7:** Difference of timing in a paddle of the start counter and the RF time for pions. The top two plots are identical and show the all hits in the paddle. The bottom left plot shows hits in the “leg” of the counter and the bottom right shows hits in the “nose.”



**Figure 8:** Same as Fig. 7 for protons.

**Figure 9:** See caption above.**Figure 10:** See caption above.

**Figure 11:** See caption above.**Figure 12:** Calibrated difference in time between the start counter and RF as a function of run. The mean (green) and  $1\sigma$  resolution (blue) are shown.

As a check on the timing resolution of the start counter, we used data containing at least two  $K^+$  (this was part of the cascade baryon search) to look at kaons, pion and protons at the same time. The momenta ( $p$ ) of the tracks was given by the drift chamber and tracking algorithm found in the TBTR bank, and the energy ( $E_{\text{PID}}$ ) of the particle was set by particle identification. This allowed us to calculate the speed of the particle:

$$\beta_{\text{PID}} = \frac{p}{E_{\text{PID}}}. \quad (6)$$

This was used to calculate the vertex time of the particle:

$$t_{\text{vtx}}^{\text{TOF}} = t_{\text{TOF}} - \frac{\ell_{\text{TOF}}}{c\beta_{\text{PID}}}, \quad (7)$$

where  $t_{\text{TOF}}$  and  $\ell_{\text{TOF}}$  are the time and path length of the track at the TOF plane as obtained from the TDPL bank. This time was converted to a “photon time” ( $t_{\text{photon}}$ ) by subtracting the photon propagation time ( $t_{\text{prop}}$ ) from the center of the target:

$$t_{\text{photon}}(\text{TOF}) = t_{\text{vtx}}^{\text{TOF}} - t_{\text{prop}}, \quad (8)$$

where

$$t_{\text{prop}} = \frac{1}{c} (z_{\text{tgt}} - z_{\text{vtx}}), \quad (9)$$

where  $z_{\text{tgt}}$  is the center of the target’s z-position (−90 cm in the CLAS coordinate system), and  $z_{\text{vtx}}$  is the z-coordinate of the track’s vertex position – in this case, the intersection of the two kaons where the covariance matrices of the estimated momenta are taken into account through the standard MVRT vertexing algorithm. This photon time,  $t_{\text{photon}}(\text{TOF})$ , was compared to the RF-corrected tagger times ( $t_{\text{TAG,RF}}$ , shown in Figs. 13 and 14) of each hit in the photon tagger as obtained from the TAGR bank. The resulting data indicates a timing resolution of 310 ns for protons, 400 ns for pions, and 430 ns for kaons.

#### 2.4.1 Start Counter Efficiency

The efficiency of the start counter was calculated by examining the number of tracks with a ST hit after track reconstruction. The ST fired 91.6% of the time, this was calculated from run 57000 since it is a good run and included in production data. **This percentage was calculated for the start counter as a whole. Any analysis that uses associated start counter hits with identified tracks must take this efficiency into account.** Note, however, that this effect is very small (< 1%) for many-particle final states where only a single start counter is required.

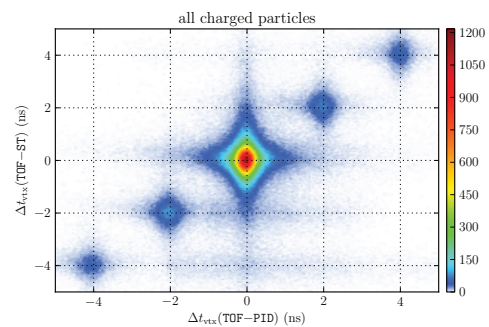


**Figure 13:** Difference in vertex times for each track for the two calculations made above. Represents 1.5% of the total statistics.

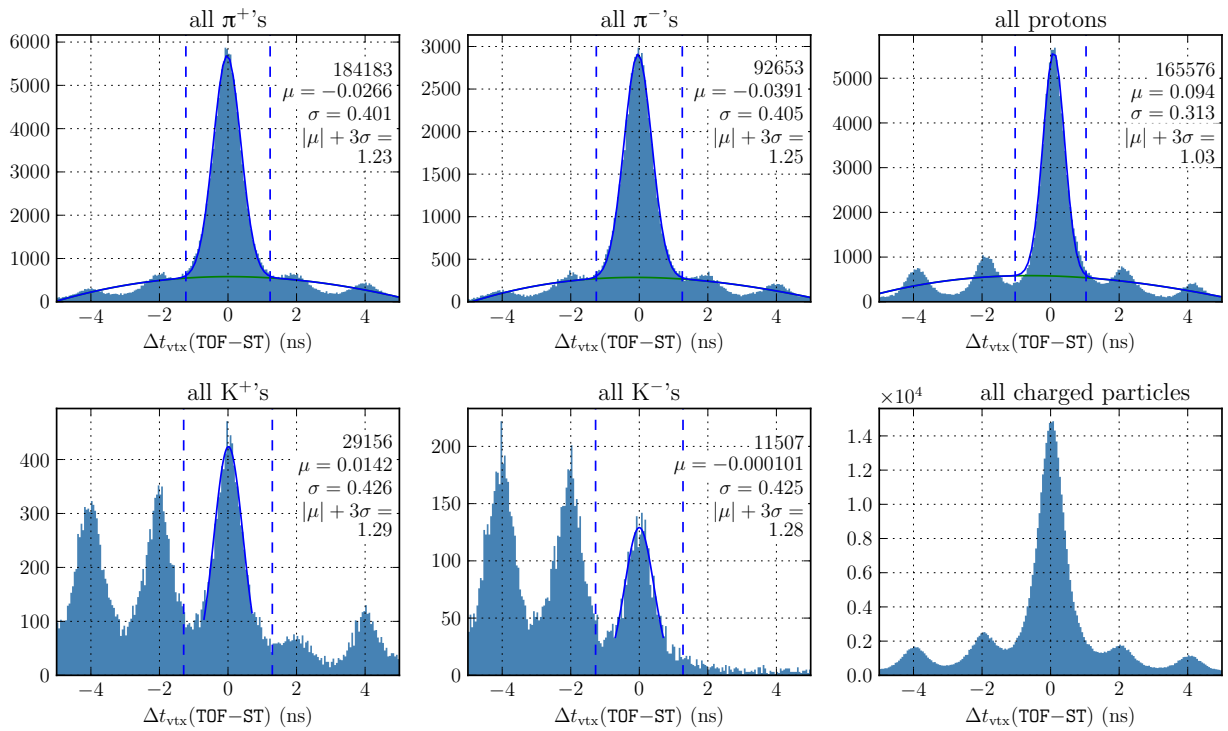


**Figure 14:** Difference in vertex time between that of the photon and of the tracks based on start counter and time-of-flight times. Represents 1.5% of the total statistics.

## 2.5 Drift Chamber Calibration and Resolution

Tracking in the Drift Chamber of a CLAS Sector is performed using the six superlayers of the DC. A good measure of the quality of tracking are the DC residuals for each superlayer. After a track is identified using the hit elements in the DC superlayer, It's DC residual is calculated using the TBLA bank as follows:

```
fabs(TBLA->tbla[i].fitdoca) - fabs(TBLA->tbla[i].calcdoca)
```

The Drift Chamber alignment was done by correcting the mean of the residuals and the results are shown in Fig. 15. The values of the DC residuals in the CLAS data are empirically found to be a good fit to a convolution of 2 Gaussians - a narrow Gaussian and a broad Gaussian. During DC calibrations efforts were made to minimize this residual to have maximum reconstruction efficiency. The mean and width of the residuals as a function of superlayer and run number are shown in Figs. 16 and 17 respectively.

### 2.5.1 Drift Chamber Wire Efficiency

To generate the wire map for *g12*, the utility pdu, available in SVN, was used. Maurizio Ungaro made the wire-maps for *g12* with the root files [A01 and A02] for each run. These output files are at [/home/mukesh/work/pdu\\_hbook](#) at JLAB. Root files needed are at [/home/mukesh/work/pdu\\_root](#). The values were added to the *g12* database. The results of the wire map are plotted in for each sector and can be found here:

[http://www.jlab.org/~ungaro/maureepage/proj/dceff/dc\\_periods/g12.html](http://www.jlab.org/~ungaro/maureepage/proj/dceff/dc_periods/g12.html)

An example plot from this site is shown in Fig. 18. The DC wire efficiencies were computed for each wire using the whole data set, using the CLAS utility pdu. An example of this is shown in the beginning of DC calibration section. Simulation data all use the gpp to apply this efficiency map. Comparison of the real data and MC data depends on the topology and model.

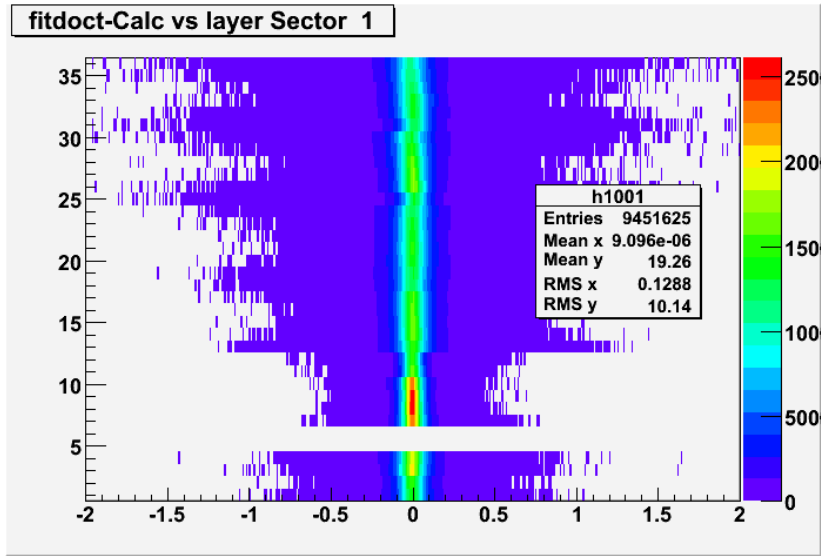


**Figure 15:** Alignment of the Drift Chambers in sector 1. All other sectors show very similar results.

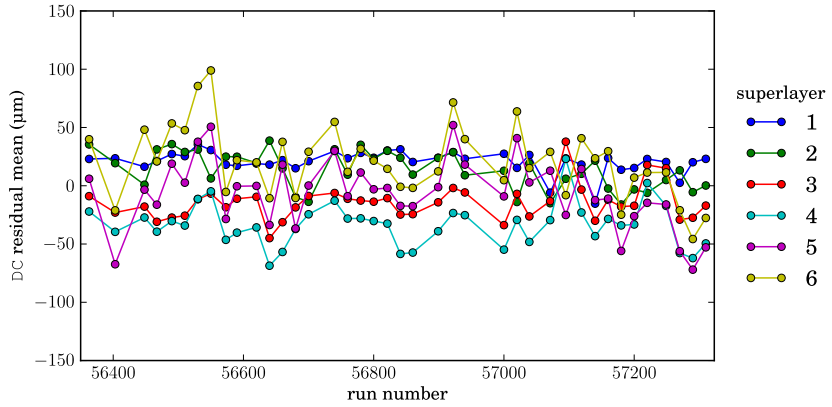


**Figure 16:** Mean of residuals for the drift chambers by superlayer and by run.

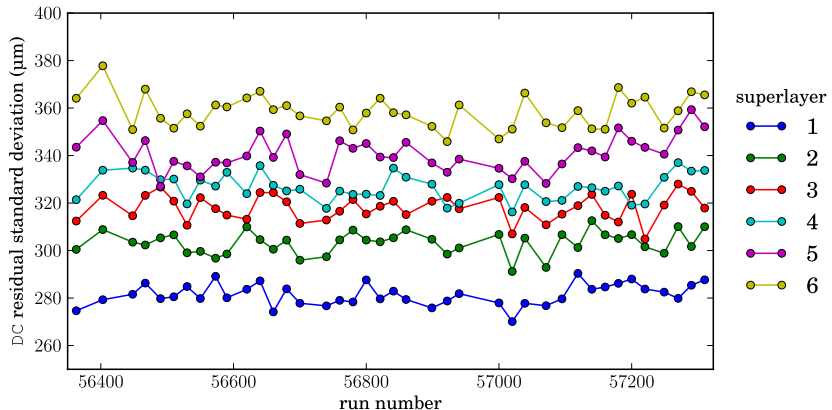


**Figure 17:** Gaussian width of residuals for the drift chambers by superlayer and by run.

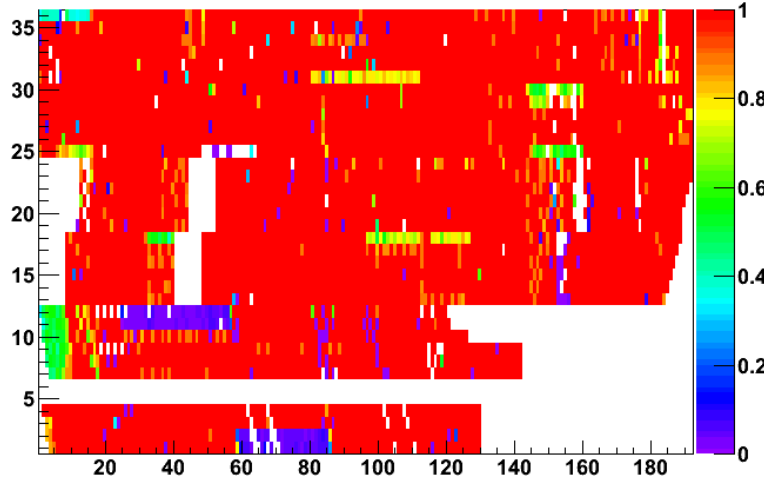


**Figure 18:** DC efficiency map for sector 1. All other sectors show very similar results.

## 2.6 Cerenkov Calibration and Performance

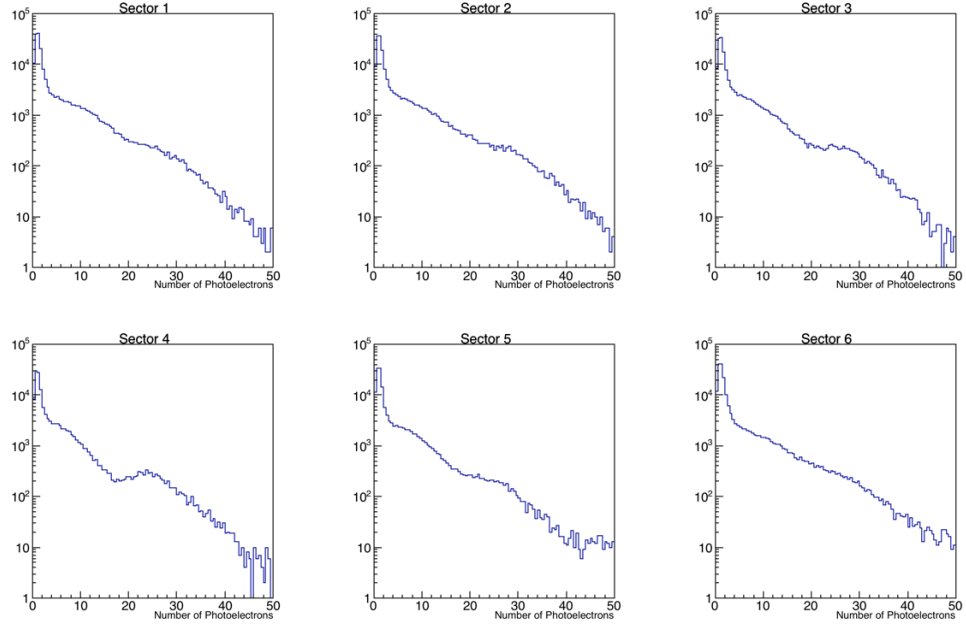
The Cerenkov detector's primary role in CLAS is to help differentiate leptons from pions at momenta below the pion Cerenkov radiation threshold. The Cerenkov for g12 was roughly calibrated by importing the (then) most recent CLAS CC calibration constants and then verifying that the photoelectron number was reasonable on a sector by sector basis. The following validation plots come from two g12 production runs skimmed only for pions via the standard PID, and inside the fiducial region as described in this document. In Fig. 19 the total photoelectron yield for each sector is shown. The histogram y-axis range is constant between all plots for ease of comparison. One can see that the photoelectron yield is consistent between sectors.

In Fig. 20 the photoelectron yields are further broken down by PMT. The z-axis (log-scale) is fixed for ease of comparison. The important feature here is that the delta-ray "pion" peak in the photoelectron spectra peaks roughly around 1.0 photoelectrons for all PMTs. The general lepton selection criteria includes a cut  $> 2.5$  photoelectrons, which is a relatively safe and conservative cut on any PMT (see Sec. 3.4 for more details on the lepton PID).

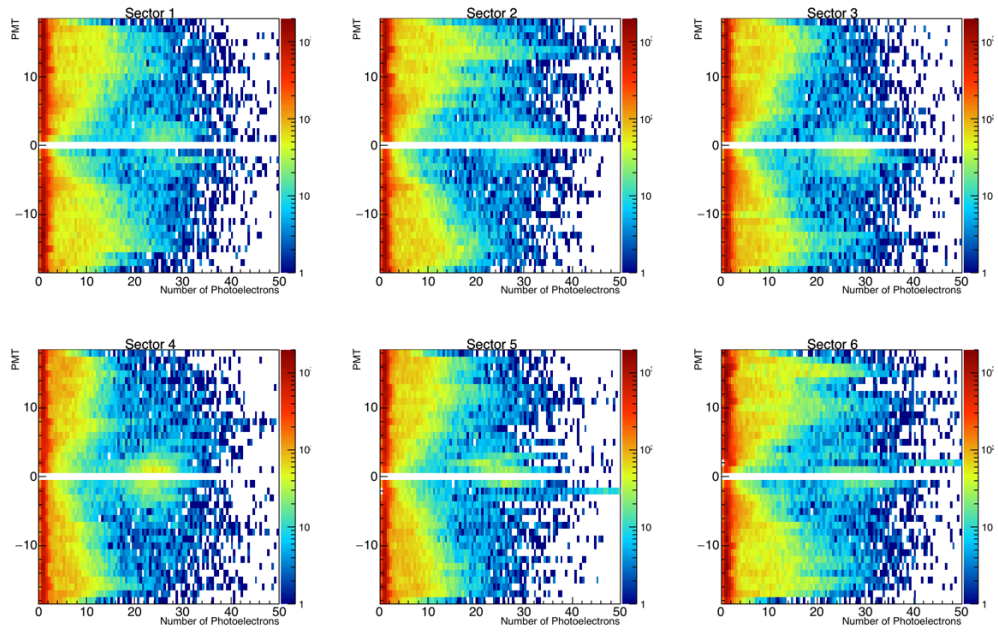
As an additional validity plot, the probability of a pion to cause a hit in the CC versus the momentum of the pion is shown in Fig. 21. This plot shows the expected behavior of the CC as the pions pass the Cerenkov radiation threshold.

### 2.6.1 Cerenkov Efficiency

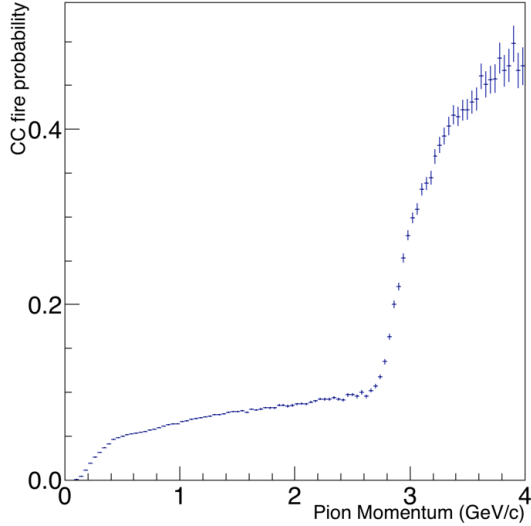
The exact efficiency of the CC over all momenta and angles for leptons was never explicitly calculated. Instead, it is recommended to look at the efficiency of the overall lepton identification procedure, if needed, for any lepton analyses.



**Figure 19:** An example CC photoelectron spectra from two production runs skimmed for pions. The y-axis range is fixed over all plots for ease of comparison.



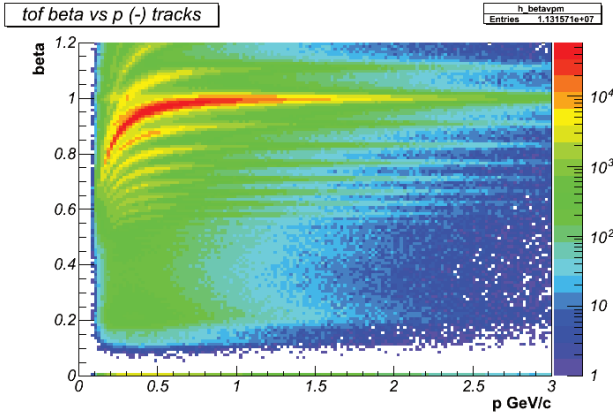
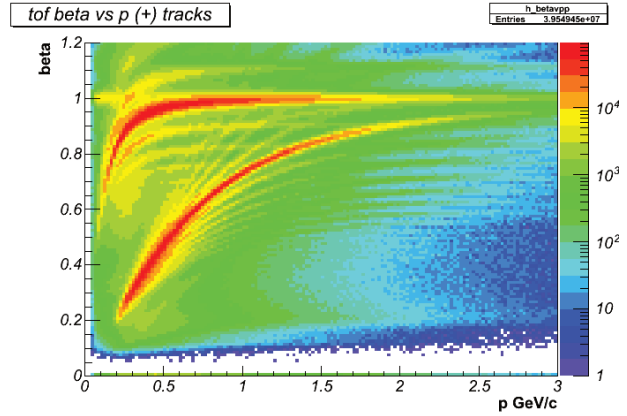
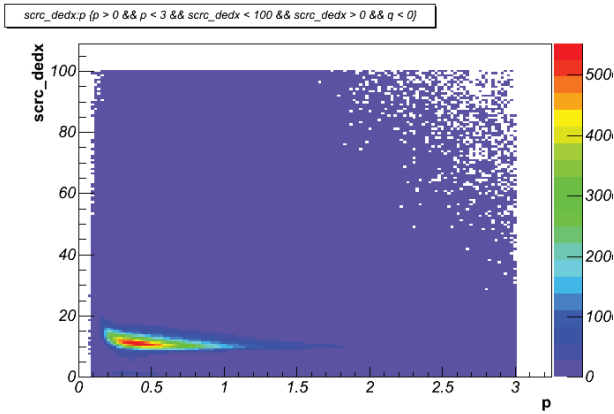
**Figure 20:** Same plot as Fig. 19 but 2D in PMT number. Negative and positive PMT numbers correspond to left and right CC PMTs. Z-axis range is fixed for ease of comparison.



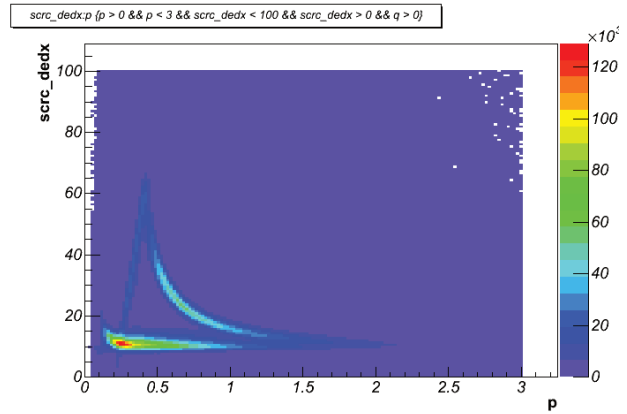
**Figure 21:** The overall CC hit probability for pions within the fiducial region versus the pion momentum.

## 2.7 Time-of-Flight Counter Calibration and Resolution

- The plots shown are for g12's run number 56855, pass0 v7. Did not change to pass1.
- Several steps were taken to calibrate the TOF for g12. Listed in C. Bookwalter's dissertation[1]:
  - Counter status
  - ADC pedestals
  - TDC linearization constants
  - Time-walk corrections
  - Left-right delay constants
  - Attenuation length
  - Minimum-ionizing particle pulse heights
  - Effective velocity
  - Paddle-to-paddle offsets
- The final time-walk corrections is a mix between constants from g6c and constants derived from g9a laser data using Gamecock.
- The plots (Figs. 22a–25b) included are:
  - The TOF velocity ( $\beta$ ) versus momentum by positive and negative tracks.
  - The RF TOF by paddle ID by sector.
  - The energy deposited versus momentum by positive and negative tracks.

(a) TOF  $\beta$  versus momentum for negative tracks(b) TOF  $\beta$  versus momentum for positive tracks

(a) TOF energy deposited versus momentum for negative tracks



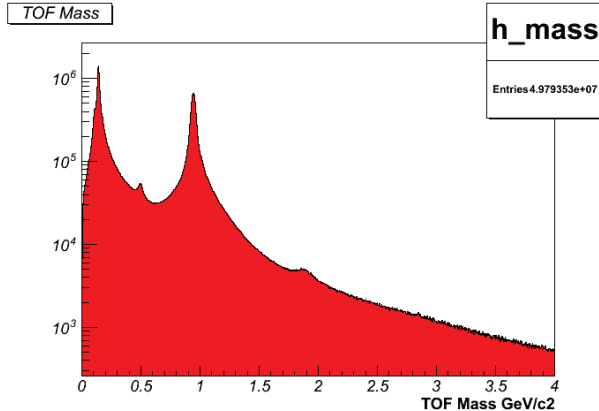
(b) TOF energy deposited versus momentum for positive tracks

- The TOF mass.
- The TOF resolution integrated over all paddles.
- The TOF run-by-run performance.

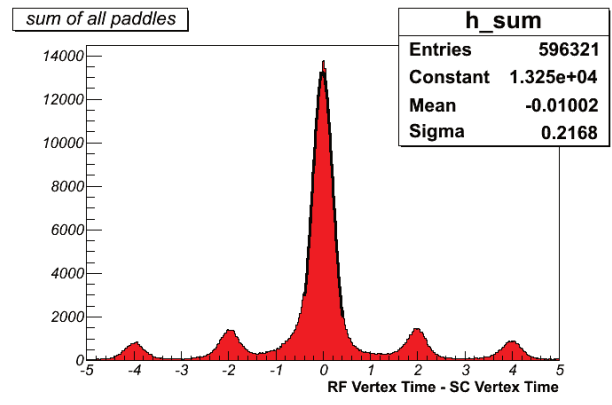
### 2.7.1 Time-of-Flight Counter Efficiency and Bad Paddles

As a standard procedure of the time-of-flight calibrations, the time-of-flight scintillators were initially studied during the calibration period, in which a list \* of scintillators had a faulty ADC or TDC as shown in Table 12. Another study, as shown below, was conducted to determine the efficiency of each paddle and to reevaluate the status of their ADC and TDC. Due to the more stringent requirements of paddle efficiency in the study below, more paddles were considered to be faulty than in the initial study. Table 16 shows the additional paddles which were considered to be inefficient.

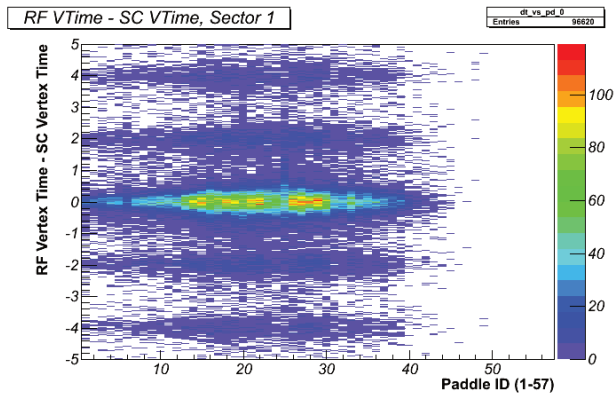
\* Can be obtained using the CLAS calibration database



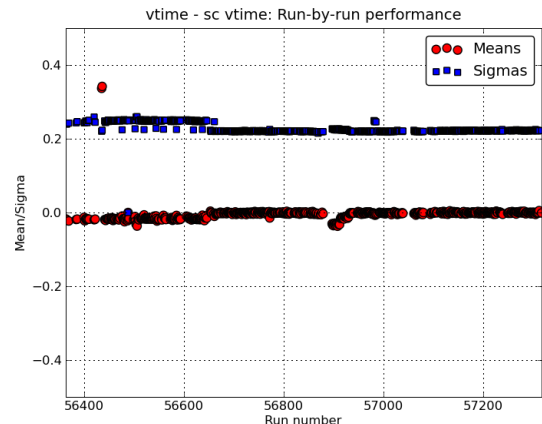
(a) TOF mass spectrum



(b) TOF resolution integrated over all paddles



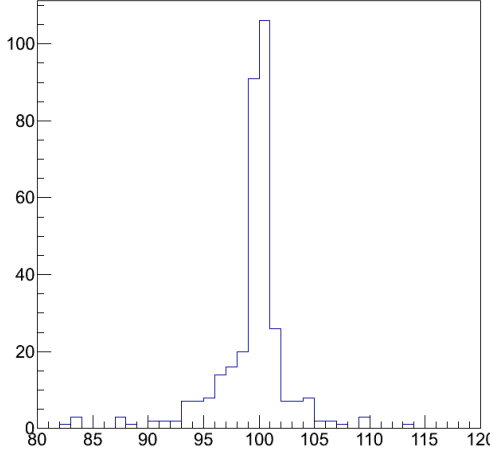
(a) Representative (sector 1) calibrated timing of the time-of-flight, paddle-by-paddle.



(b) TOF run-by-run performance

**Table 12:** List of faulty paddles as compiled during calibration

Sector	SCID	Notes
1	6	No ADCR and TDCR
2	8	No ADCL and TDCL
2	34	No ADCL and TDCL
3	11	No ADCR and TDCR
3	57	No ADCL, ADCR, TDCL, and TDCR
4	48	No ADCL and TDCL
5	57	No ADCL, ADCR, TDCL, and TDCR
6	5	No ADCR and TDCR

**Figure 26:** Relative occupancy of all scintillators**Table 13:** Paddles below two and three standard deviations from the mean relative occupancy

	$2\sigma = 92.49\%$	$3\sigma = 89.05\%$
Sector 1	35 (91.20%)	40 (87.87%), 41 (82.63%), 56 (83.37%)
Sector 2	2 (92.38%), 35 (90.11%), 50 (91.99%)	41 (87.31%), 56 (87.98%)
Sector 3	35 (90.59%)	40 (88.98%), 41 (83.29%)
Sector 4		41 (83.61%)

To determine efficiency of each scintillator paddle, the number of hits <sup>†</sup> registered by every paddle was recorded <sup>‡</sup>. The relative occupancy of paddle  $i$  in sector  $j$  is defined the following way: list the number of hits recorded by all paddle  $i$ 's in sectors  $\neq j$  and remove the ones with the most and least hits from the list. Take the average number of hits of the remaining three paddles. The relative occupancy is defined as

$$100 \times \frac{\text{Number of hits in paddle } i \text{ of sector } j}{\text{Average of remaining three paddles}} \%$$

Fig. 26 shows the relative occupancy of all scintillators plotted on a single histogram. A paddle is defined as inefficient if it is greater than two standard deviations below the mean relative occupancy of all scintillators. Table. 13 shows the paddles which are below two (left) or three (right) standard deviations below the mean relative occupancy.

### 2.7.2 ADC and TDC Values

The occupancy alone is not enough to determine which scintillators are bad. The ADC and TDC values for all scintillators were also recorded and studied. Fig. 27 shows the ADC and TDC values for all scintillators. Some of the events registered had an ADC or TDC value of zero or a maximum ADC value (shaded in red).

<sup>†</sup>The data used were obtained from the `clas_0[run#].A01` files located in `/mss/clas/g12/data/`

<sup>‡</sup>This was done by using `bosdump -GSC` and parsing its output

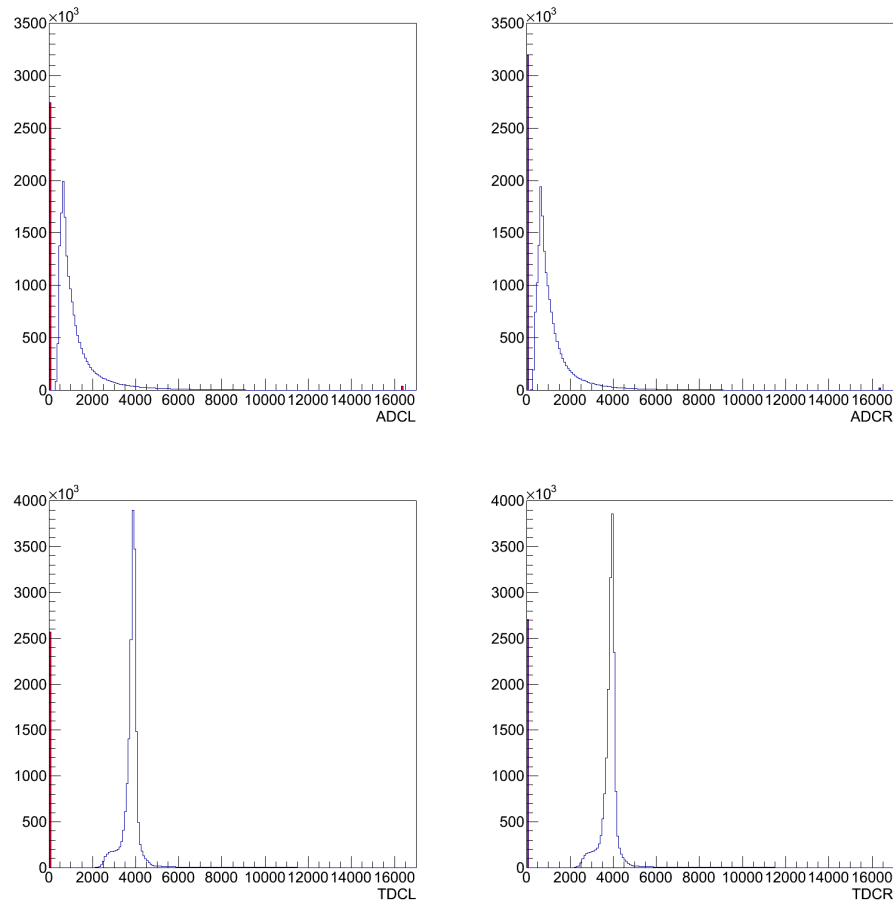


**Figure 27:** Top: ADC values of all scintillators. Left ADC (ADCL) values are on the left and right ADC values are on the right (ADCR). Shaded in red are events recorded with an ADC value of zero or maximum. Bottom: Same as Top but for TDC values

**Table 14:** Paddles which registered an ADC or TDC value of zero greater than 50% and 45%, respectively, of its entries

	% Events with ADCL or ADCR = 0 > 50%	% Event with TDCL or TDCR = 0 > 45%
Sector 1	6 (100% ADCR)	6 (100% TDCR), 46 (97.89% TDCL), 50 (98.11% TDCL)
Sector 2	8 (100% ADCL), 34 (100% ADCL), 44 (50.22% ADCL), 54 (52.00% ADCR)	8 (100% TDCL), 34 (100% TDCL), 44 (47.51% TDCL), 54 (47.10% TDCR)
Sector 3	11 (100% ADCR), 56 (74.75% ADCR)	11 (100% TDCR), 56 (62.79% TDCR)
Sector 4	48 (100% ADCL)	48 (100% TDCL)
Sector 5	48 (77.98% ADCL)	48 (76.10% TDCL)
Sector 6	5 (100% ADCR), 56 (59.30% ADCR)	1 (98.78% TDCL), 5 (100% TDCR), 33 (97.78% TDCL)

**Table 15:** Union of Tables 13 and 14 (Recommended list of paddles to knockout)

Sector 1:	6, 35, 40, 41, 50, 56
Sector 2:	2, 8, 34, 35, 41, 44, 50, 54, 56
Sector 3:	11, 35, 40, 41, 56
Sector 4:	41, 48
Sector 5:	48
Sector 6:	1, 5, 33, 56

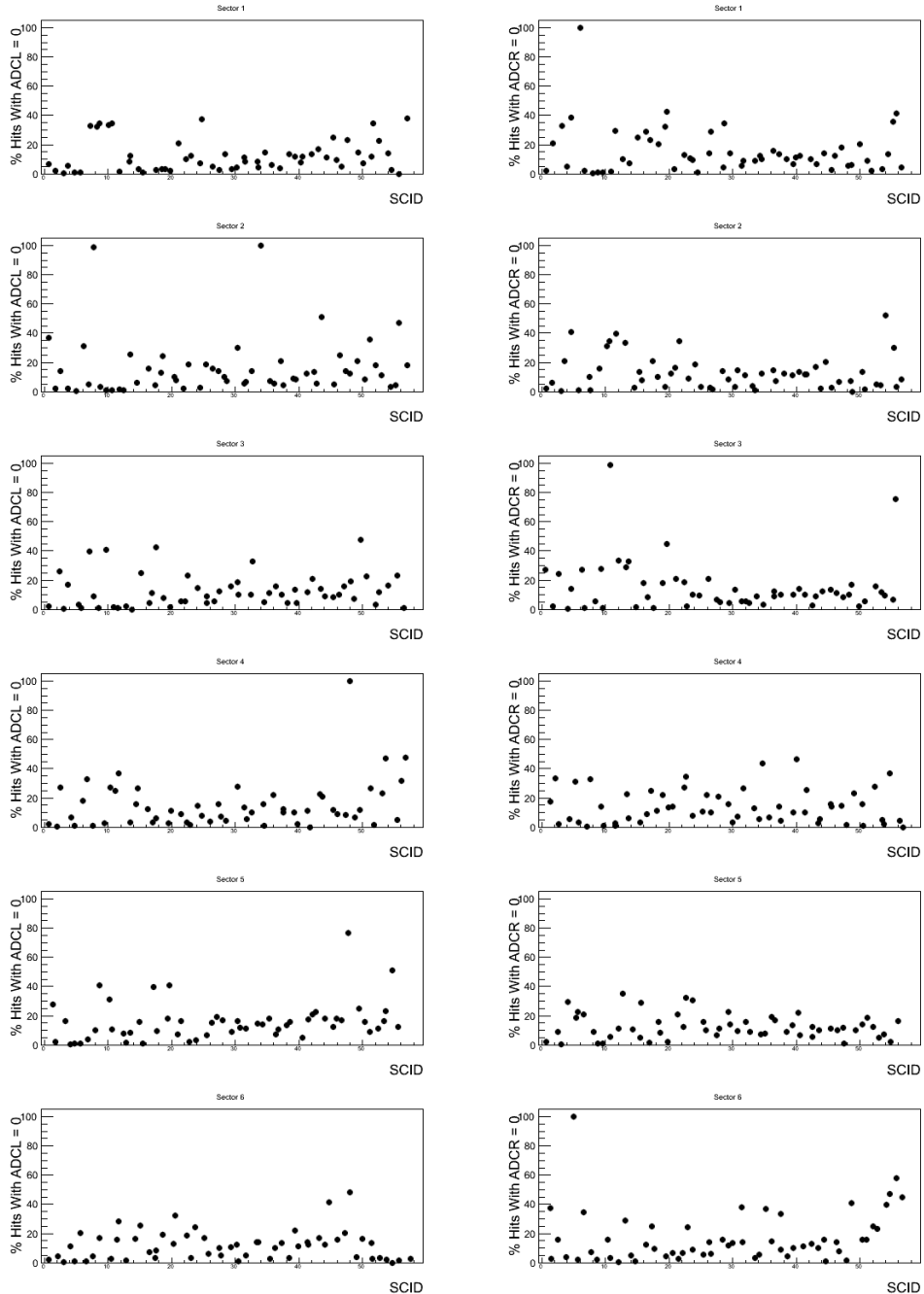
The percentage of events a scintillator recorded either a TDC or ADC value of zero or maximum ADC value was studied as shown in Figs. 28, 30 and 29. Figures 28, 29 and 31 assisted in determining bad paddles. It (is to be) was decided that a paddle cannot have more than 50% of its ADC (left or right) values be equal to zero or more than 45% of its TDC (left or right) values equal to zero. Table 14 shows which paddles fall in these categories. Table 15 shows which scintillators should be knocked out due to low occupancy or too many null ADC or TDC values. Due to the small number of events in which a maximum ADC value is obtained, it is not recommended in knocking paddles out based on this measure. However, Table 17 shows the paddles which attain a maximum ADC value on more than 2.5% of its registered events.

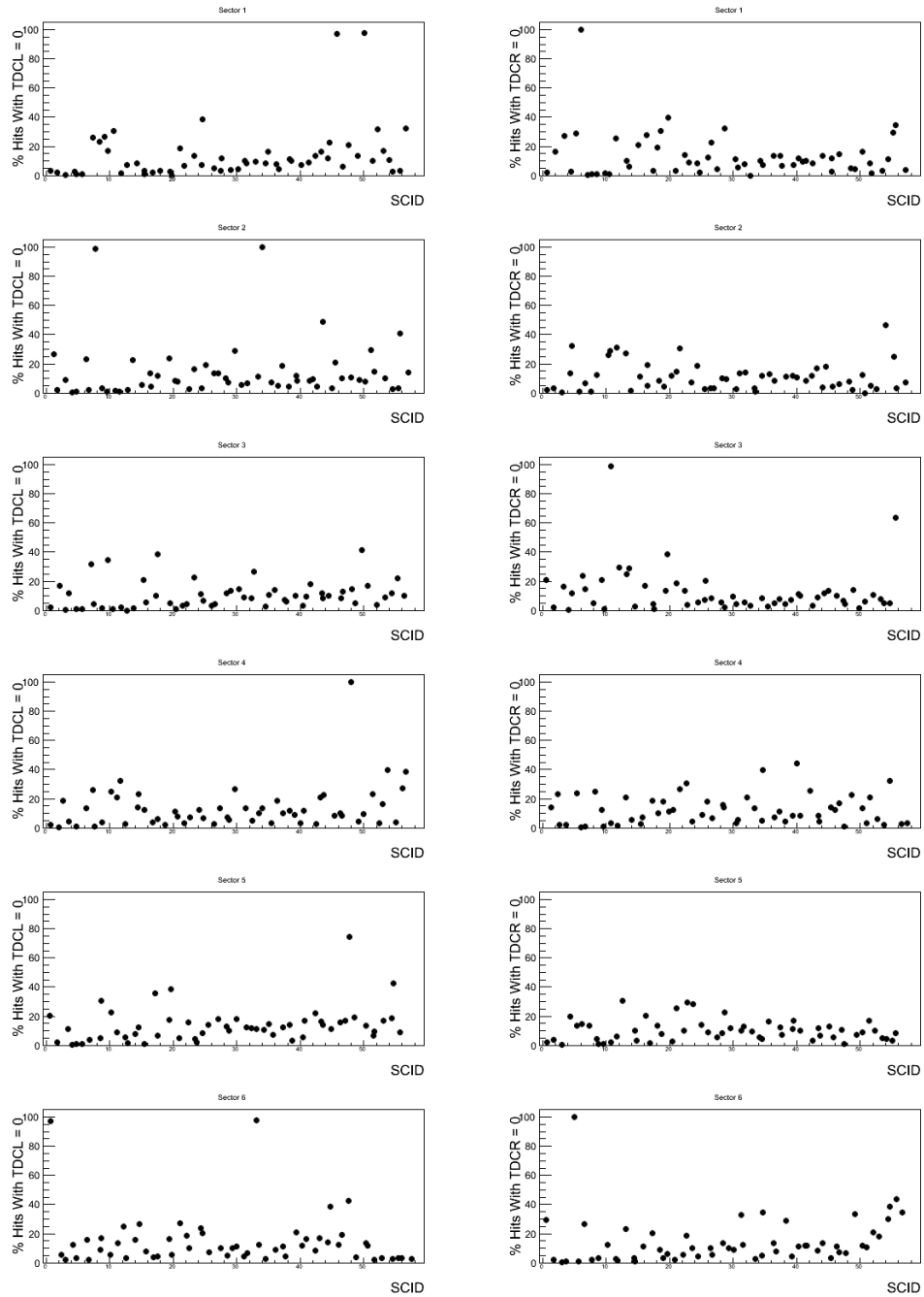
**Table 16:** Paddles in 15 not included in 12

Sector 1:	35, 40, 41, 50, 56
Sector 2:	2, 35, 41, 44, 50, 54, 56
Sector 3:	35, 40, 41, 56
Sector 4:	41
Sector 5:	48
Sector 6:	1, 33, 56

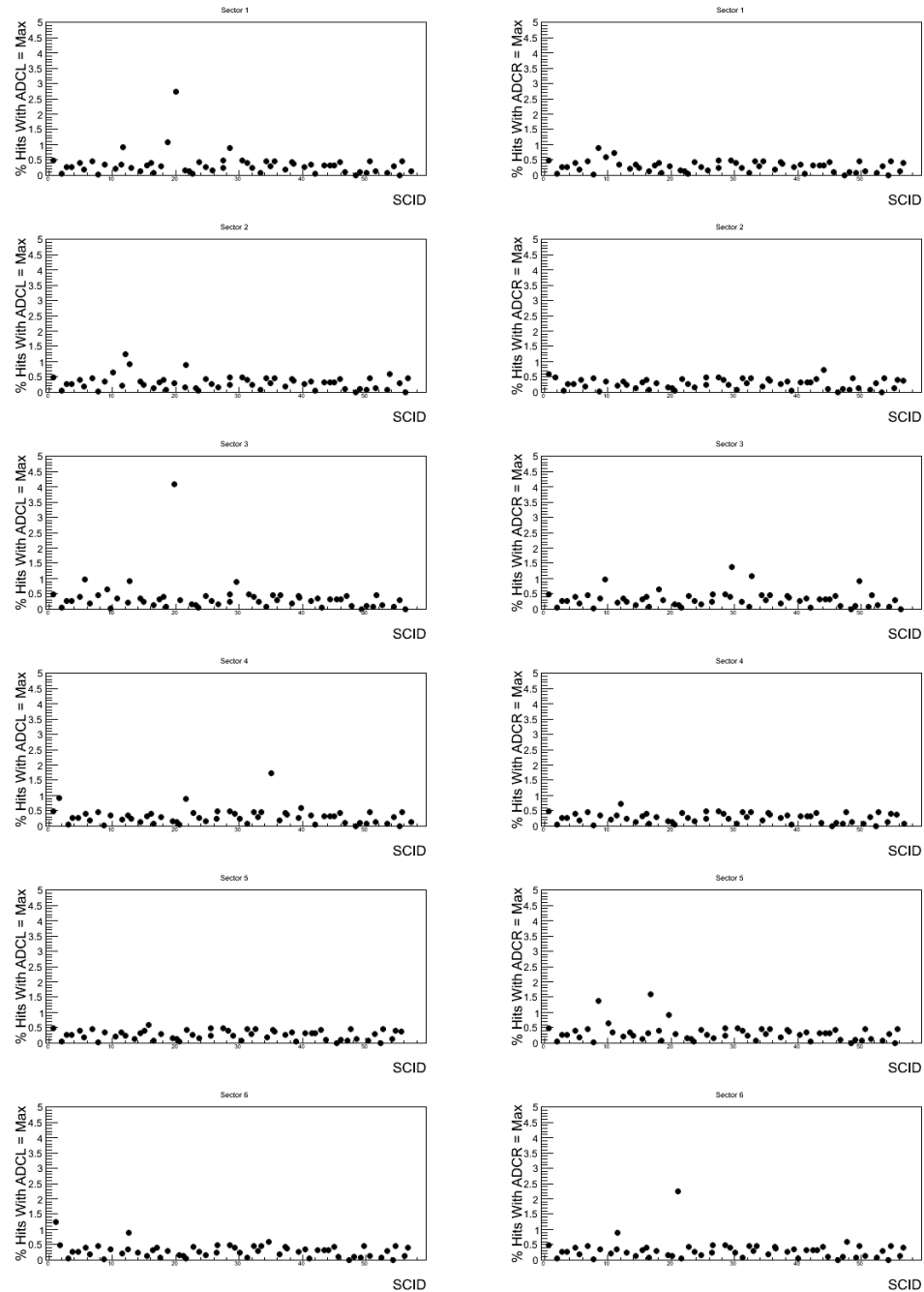
**Table 17:** Paddles with percentage of hits registering a maximum ADC value > 2.5% of its events

Sector 1: 20 (2.93% ADCL)
Sector 3: 20 (4.26% ADCL)

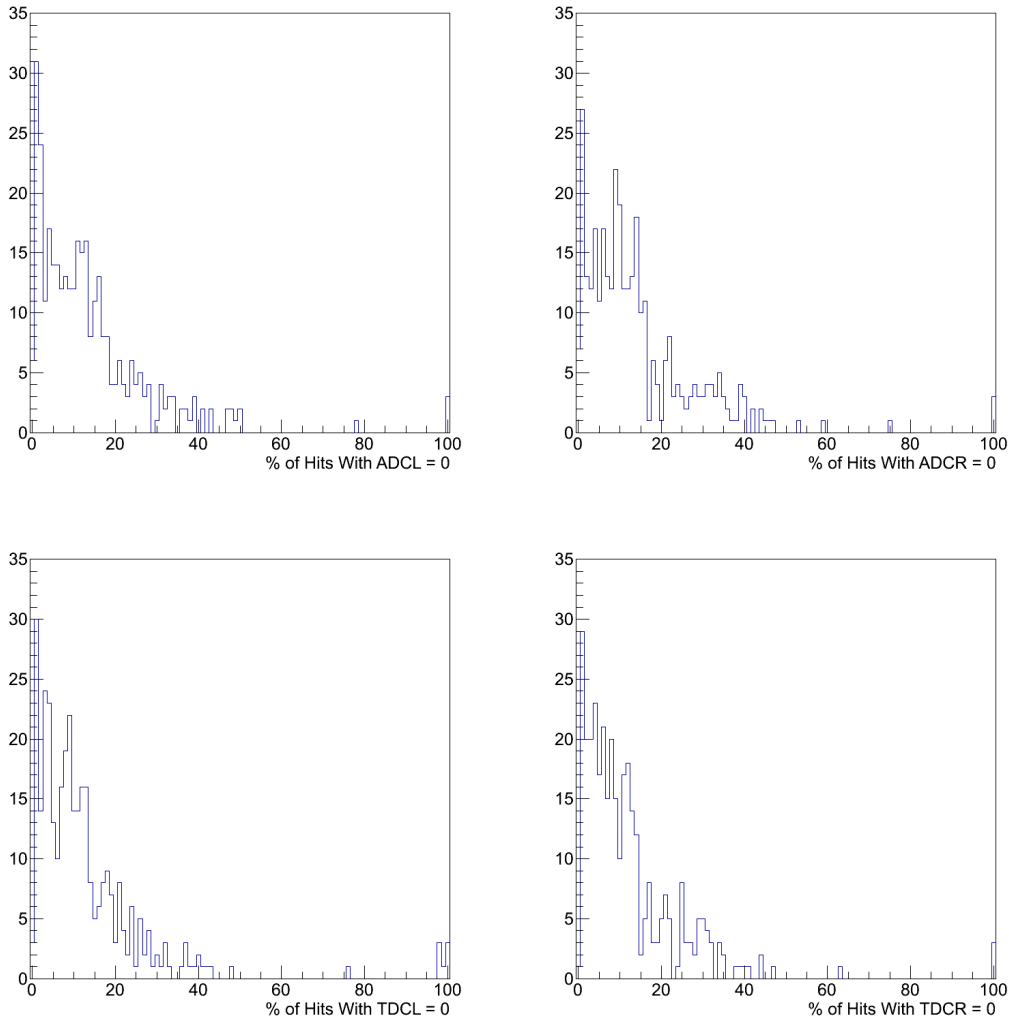
**Figure 28:** Percentage of hits registering an ADC value of 0 for all scintillators. Left ADC (ADCL) are on the left and right ADC (ADCR) values are on the right



**Figure 29:** Percentage of hits registering an TDC value of 0 for all scintillators. Left TDC (TDCL) are on the left and right TDC (TDCR) values are on the right



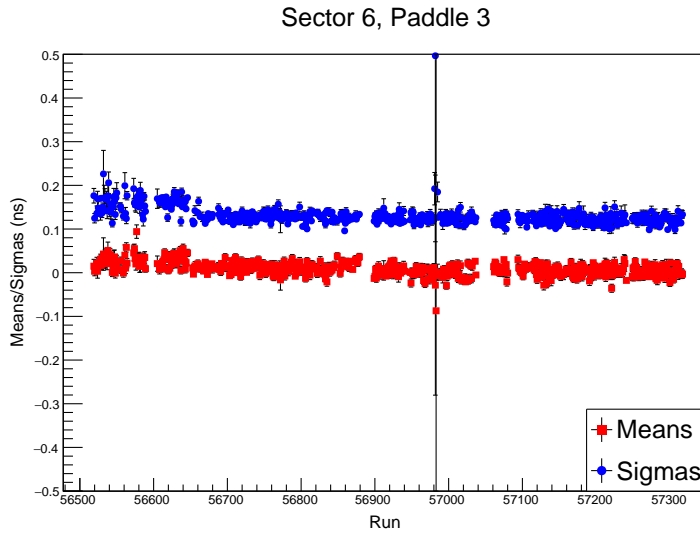
**Figure 30:** Percentage of hits registering a maximum ADC value for all scintillators. Left ADC (ADCL) are on the left and right ADC (ADCR) values are on the right



**Figure 31:** Top: Y axis projections of Fig. 28. Bottom: Y axis projections of Fig. 29

**Table 18:** Additional paddles to knock out due to drifts in the mean  $\Delta$  TOF or resolutions

Sector 1:	25, 26
Sector 2:	18, 25, 27
Sector 3:	1, 18, 32
Sector 4:	8, 19
Sector 6:	24

**Figure 32:** TOF resolution as a function of run number for a good paddle

### 2.7.3 Time-of-Flight Paddle Resolution

So far, the selection of bad paddles is based only on the raw data, which is only good for the initial selection. We further investigate the timing resolution of each paddle by run in order to determine stability of their resolutions throughout the experiment. The following data analyzed were from events containing  $p\pi^+\pi^-$  in the final state. For the  $\pi^+$  and  $\pi^-$ , the difference between the measured time-of-flight and the expected time-of-flight for a given run was plotted and fitted to a Gaussian. This was done for every paddle and every run. We define the resolution of that paddle to be the standard deviation of the fit. A few paddles that had not been previously knocked out had drifts on either the resolution or the mean  $\Delta$  TOF and were not properly calibrated. Table 18 shows which paddles should ideally be knocked out due to this. Consequently, the track dependent efficiency correction have been redirived with these paddles being knocked out as well. Figure 32 shows an example of a good paddle's resolution and mean  $\Delta$  TOF while figure 33 shows an example of a bad paddle. The TOF resolution for every paddle by run is stored in the g12 wiki.

To summarize, the final, combined TOF paddle knock out is listed in the table below:

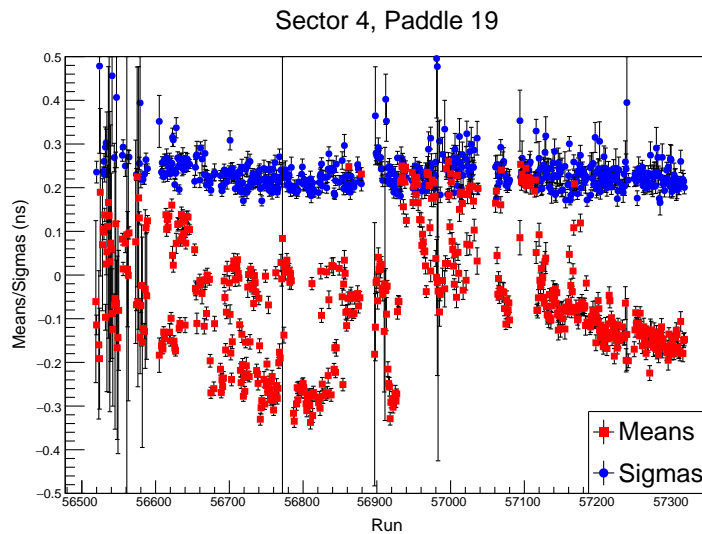


**Figure 33:** TOF resolution as a function of run number for a bad paddle

**Table 19:** Recommended list of paddles to knockout.

Sector 1:	6, 25, 26, 35, 40, 41, 50, 56
Sector 2:	2, 8, 18, 25, 27, 34, 35, 41, 44, 50, 54, 56
Sector 3:	1, 11, 18, 32, 35, 40, 41, 56
Sector 4:	8, 19, 41, 48
Sector 5:	48
Sector 6:	1, 5, 24, 33, 56

## 2.8 Electromagnetic Calorimeter Calibration and Resolution

The timing calibration of the EC system was performed using the ecGammaCal package, using photon hits. This package has been used by multiple running groups, although not all groups. An example of the method, shown in Fig. 34, compares the photon vertex time according to EC and the event vertex time. This calibration process uses real photon hits to perform the calibration on an iterative basis by improving the definition of good photon hits using prior calibration constants. Once the preliminary results are obtained, the stability of the calibration constants are monitored on a run-by-run basis. The integrated results are shown in Fig. 35 for sector 1 as an example. Clearly, the whole running period can be divided into several stable running periods to obtain the final calibration constants. The quality of the calibration for these individual ranges can be seen in Fig. 36. The timing resolution in Fig. 36 are shown to be about 700 ps, instead of 500 ps, due to the fact that in the inclusion of background hits in the EC that are not photons.

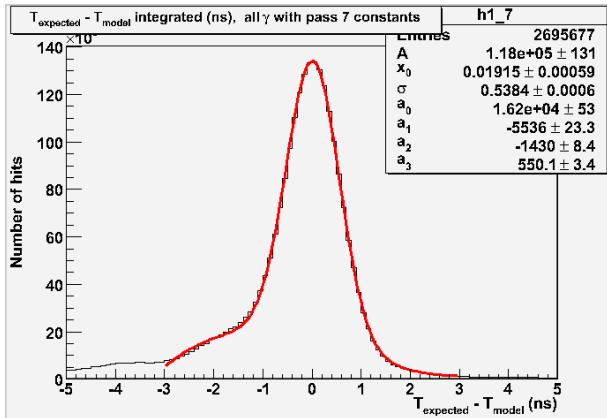


**Figure 34:** An example of the EC calibration plot, comparing the difference between photon vertex time according to EC ( $T_{\text{model}}$ ) and according to the event vertex time( $T_{\text{expected}}$ ), to obtain the EC timing calibration constants. The resolution, integrated for all tubes, is about 500 ps for good photon candidates.

Although not solely dependent on the EC timing calibration quality, the  $\pi^0$  mass and resolution are also monitored on a run-by-run basis (Fig. 37), which shows great stability.

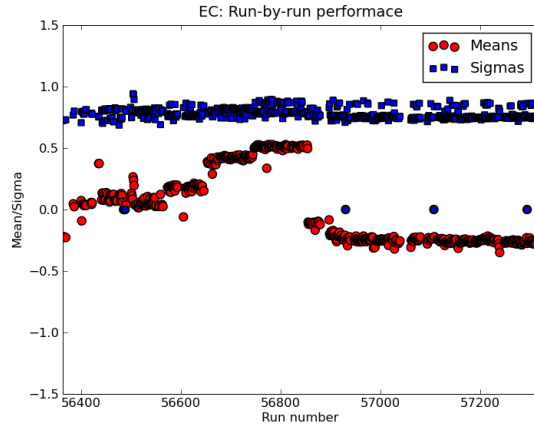


**Figure 35:** An example of the EC timing calibration before the final results, i.e., the mean and  $\sigma$  of the difference in photon vertex time according to EC and the event vertex time, as a function of the run numbers. Only sector 1 is shown here.

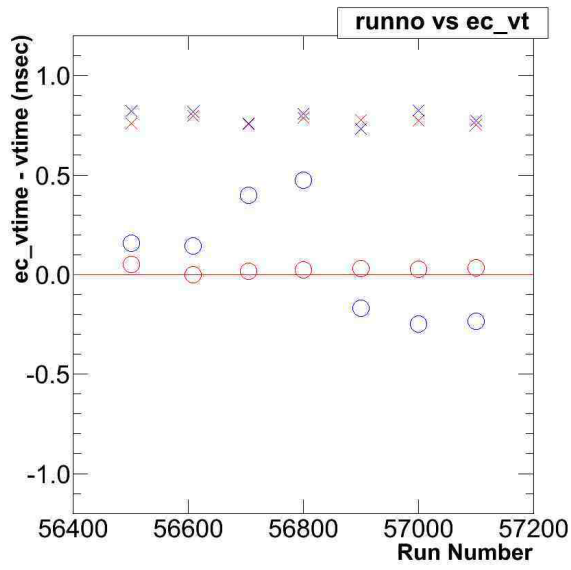


**Figure 36:** The quality of EC timing calibration, i.e., the mean and  $\sigma$  of the difference in photon vertex time according to EC and the event vertex time, monitored for several run ranges. The ranges are chosen according to Fig. 35.

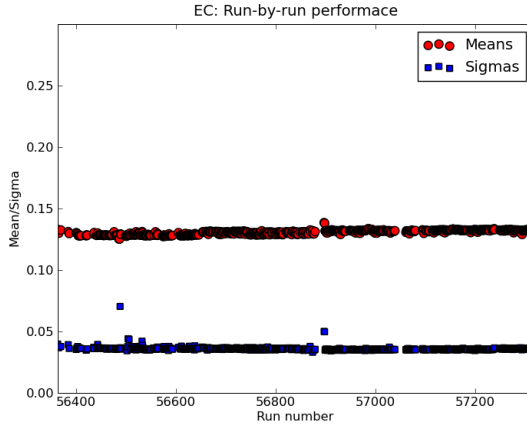


**Figure 37:** The mass and resolution of the  $\pi^0$  reconstructed from fitting two-photon invariant mass spectra as a function of the run number.

### 2.8.1 Electromagnetic Calorimeter Efficiency and Bad Paddles

The efficiency for the EC subsystem is different for each strip in the  $u$ ,  $v$ ,  $w$  arrangement. As a result, there are regions of detection which are inefficient. An extreme example of this is illustrated in Fig. 38, where the EC *inner* (top row) and *outer* (bottom row) strips are plotted as a function of the azimuthal angle ( $\phi$ ) for sector 5. A dead or inefficient strip is seen as a horizontal band in Fig. 38. The curvature of inefficient strips seen are reflections of inefficiency in an another orientation. For example, the curves seen in the top left plot,  $u$  orientation, of Fig. 38 is a reflection of dead or inefficient strips from  $v$  and  $w$  orientations respectively. All inefficiencies and cuts are shown for the  $e^-$  data. These inefficiencies and cuts are valid for the  $e^+$  data. The projection of Fig. 38 onto the y-axis can be seen in Fig. 39. This view depicts the actual paddles that are dead or inefficient. It can be seen in either Figs. 38 and 39 that there exists inefficient EC strips for sector 5. The inefficient strips were removed in data and MC. The effect of the inefficient strip cut, along with the standard CLAS EC geometric fiducial cuts can be seen in Fig. 40 and Fig. 41.

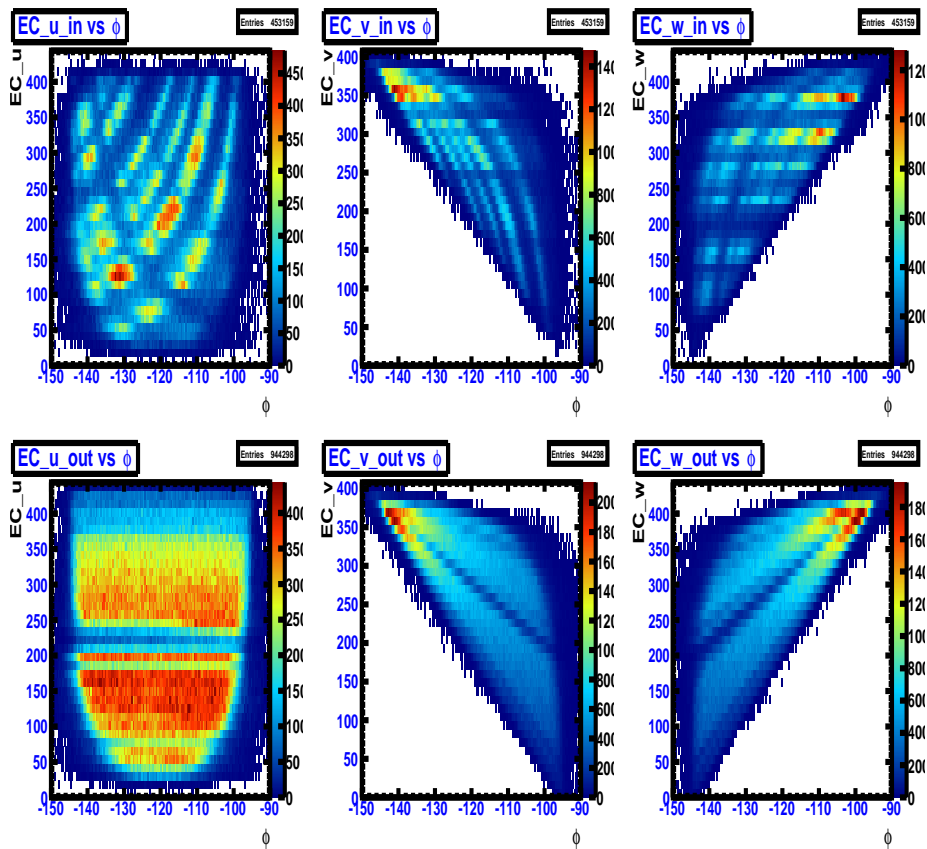


**Figure 38:** Inefficient EC  $u, v, w$  strips vs.  $\phi$  for sector 5 in CLAS  $e^-$  data. Top row depicts the  $u, v, w$  strips for the *inner* EC, while the bottom row depicts the  $u, v, w$  strips for the *outer* EC. The z-axis illustrates the number of hits in the plot. Image source: [10]

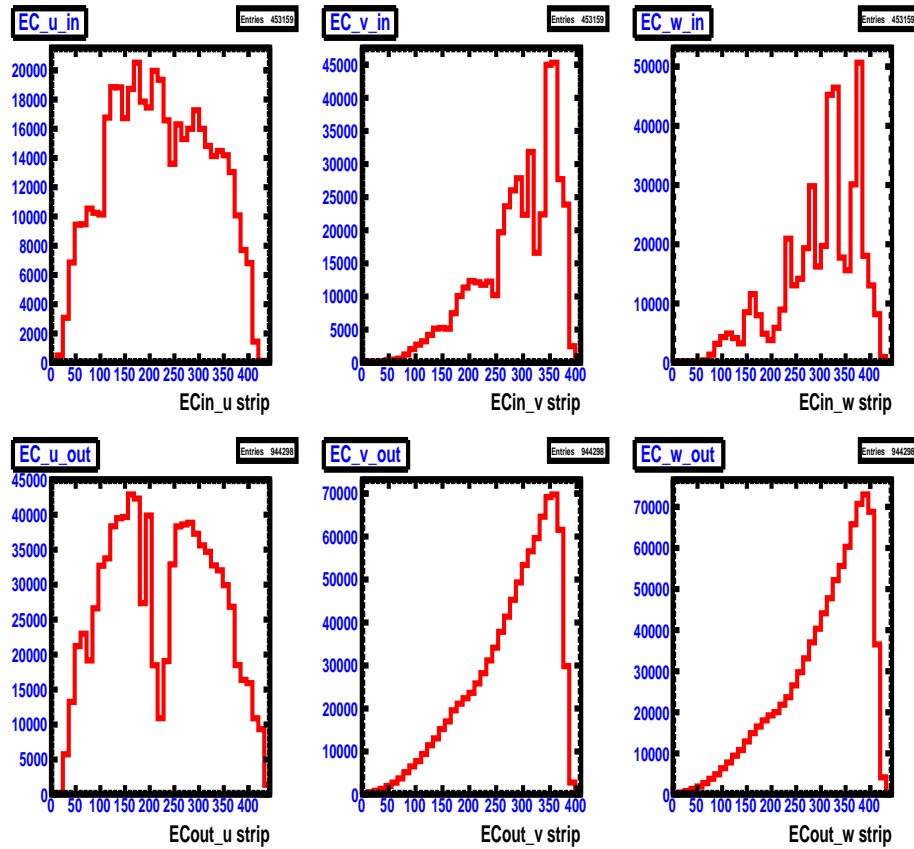


**Figure 39:** Number of hit vs. inefficient EC  $u$ ,  $v$ ,  $w$  strips for sector 5 for  $e^-$  data. Top row depicts the  $u$ ,  $v$ ,  $w$  strips for the *inner* EC, while the bottom row depicts the  $u$ ,  $v$ ,  $w$  strips for the *outer* EC. Image source: [10]

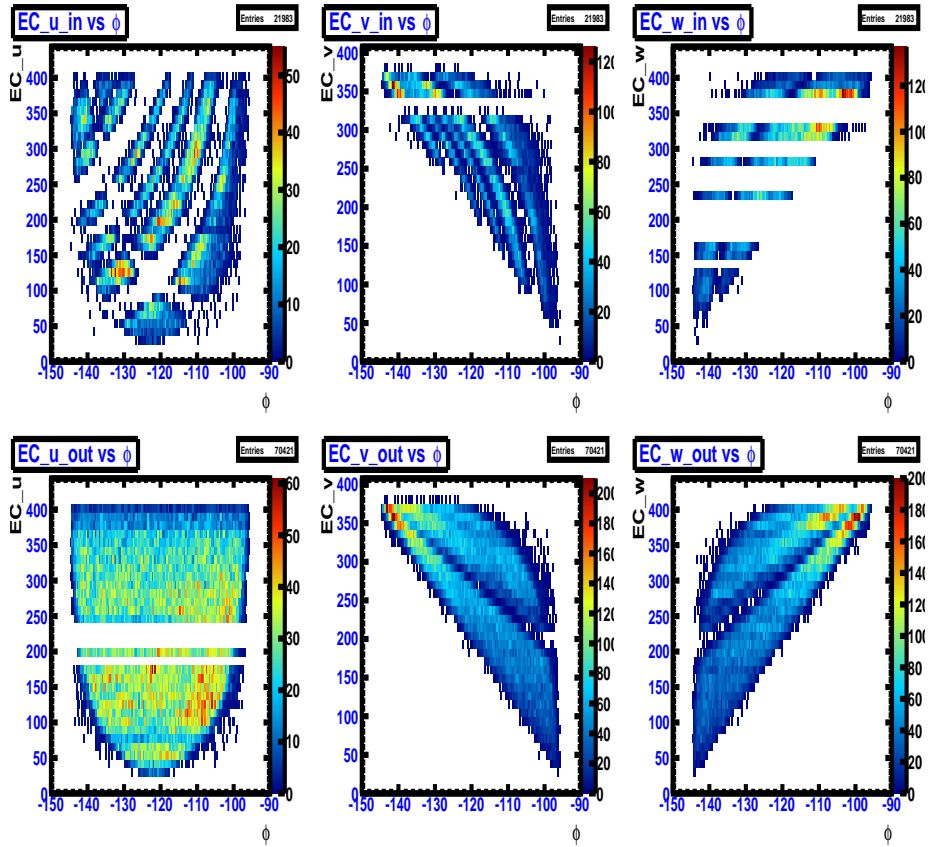


**Figure 40:** EC  $u, v, w$  strips vs.  $\phi$  for sector 5 with fiducial cuts and inefficient paddle knockouts applied to  $e^-$  data. Top row depicts the  $u, v, w$  strips for the *inner* EC, while the bottom row depicts the  $u, v, w$  strips for the *outer* EC. The z-axis illustrates the number of hits in the plot. Image source: [10]

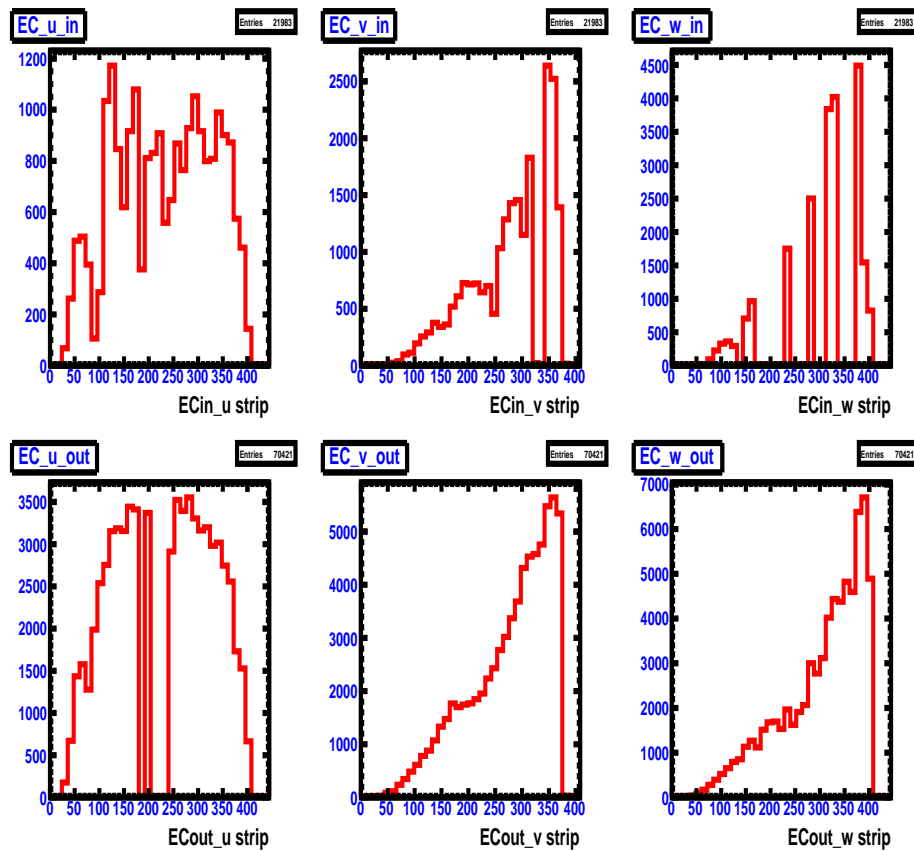


**Figure 41:** Number of hits vs. EC  $u$ ,  $v$ ,  $w$  strips for sector 5 with fiducial cuts and inefficient paddle knockouts applied to  $e^-$  data. Top row depicts the  $u$ ,  $v$ ,  $w$  strips for the *inner* EC, while the bottom row depicts the  $u$ ,  $v$ ,  $w$  strips for the *outer* EC. Image source: [10]

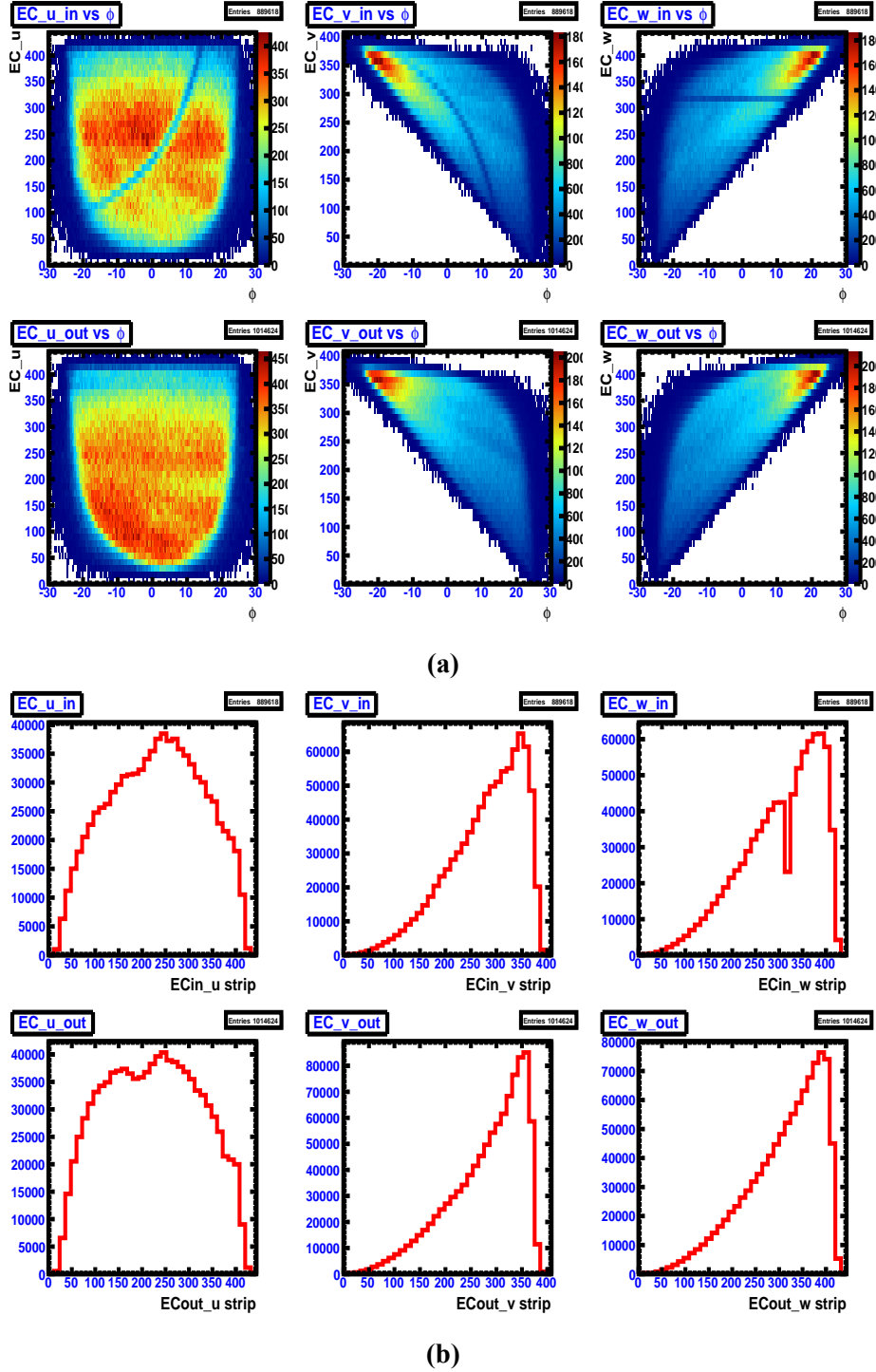


**Figure 42:** Inefficient EC  $u, v, w$  strips vs.  $\phi$  for sector 1 in CLAS  $e^-$  data (a), notation the same as Fig. 38. Number of hits vs. inefficient EC  $u, v, w$  strips for sector 1 for  $e^-$  data (b). Notation same as in Fig. 39. Image source: [10]

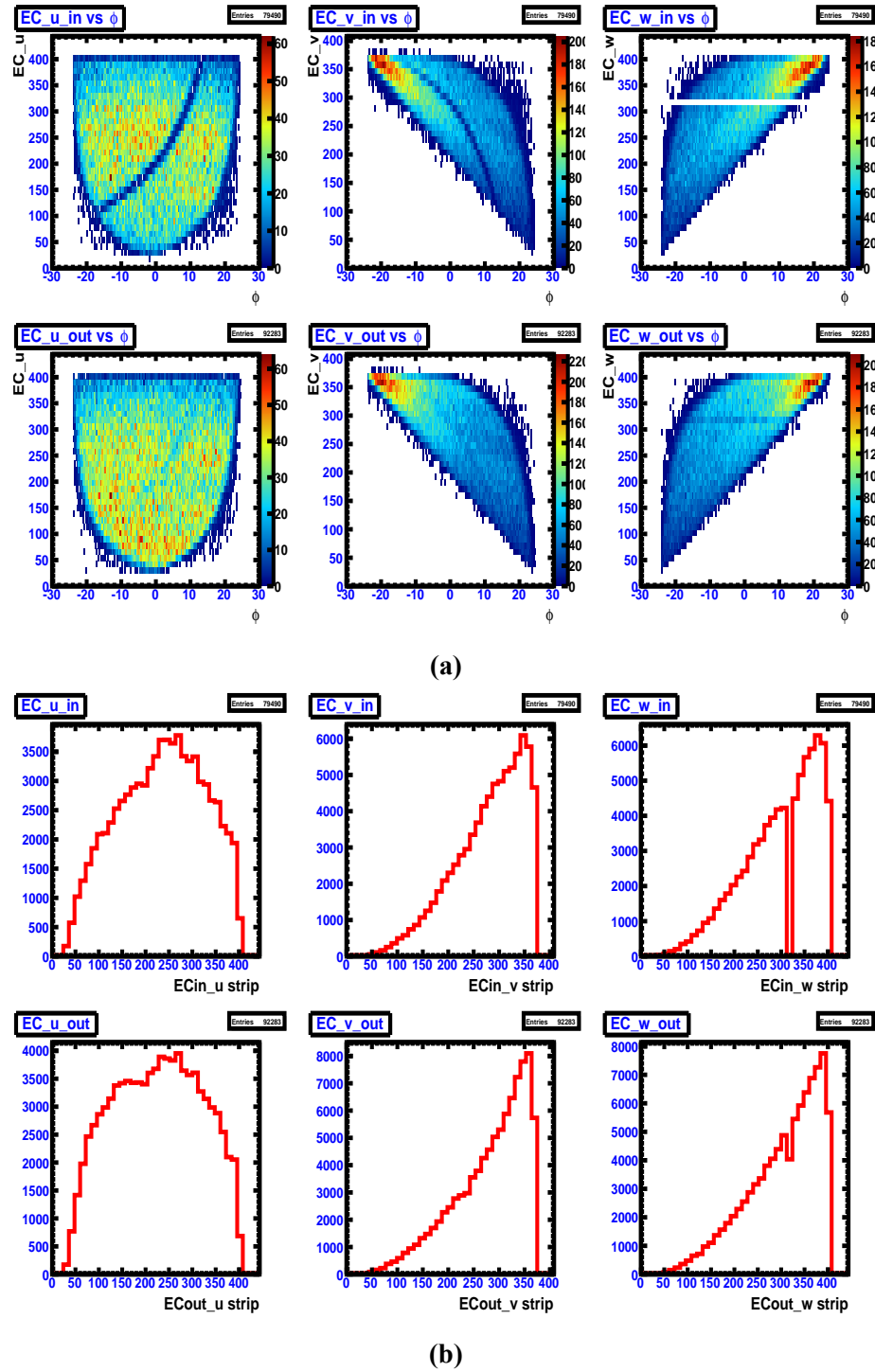


**Figure 43:** EC  $u, v, w$  strips vs.  $\phi$  for sector 1 with fiducial cuts and inefficient paddle knockouts applied to  $e^-$  data (43a), notation the same as Fig. 40. Number of hits vs. EC  $u, v, w$  strips for sector 1 with fiducial cuts and inefficient paddle knockouts applied to  $e^-$  data (43b). Notation same as in Fig. 41. Image source: [10]

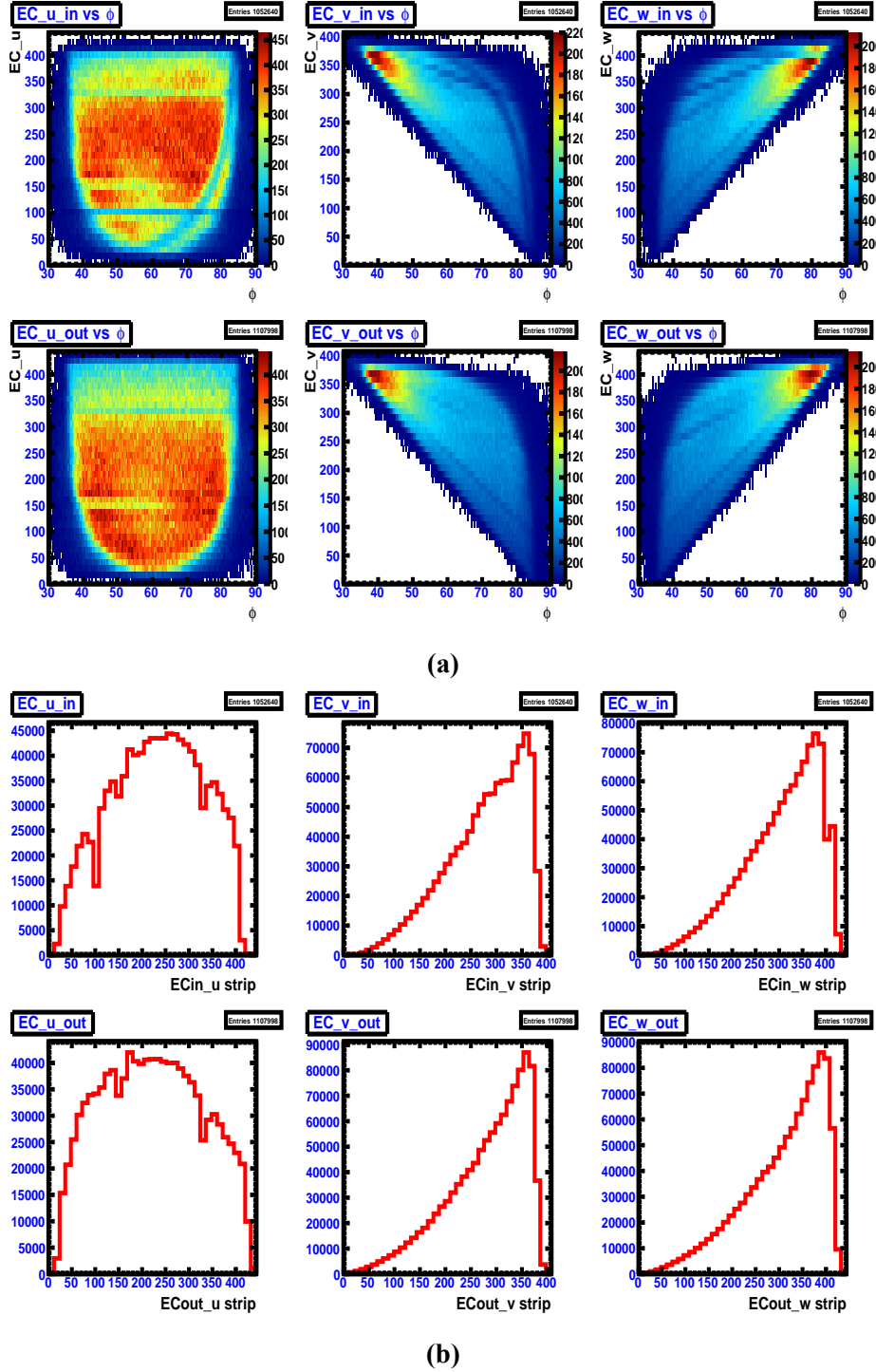


**Figure 44:** Inefficient EC  $u, v, w$  strips vs.  $\phi$  for sector 2 in CLAS  $e^-$  data (44a), notation the same as Fig. 38. Number of hits vs. inefficient EC  $u, v, w$  strips for sector 2 for  $e^-$  data (44b). Notation same as in Fig. 39. Image source: [10]

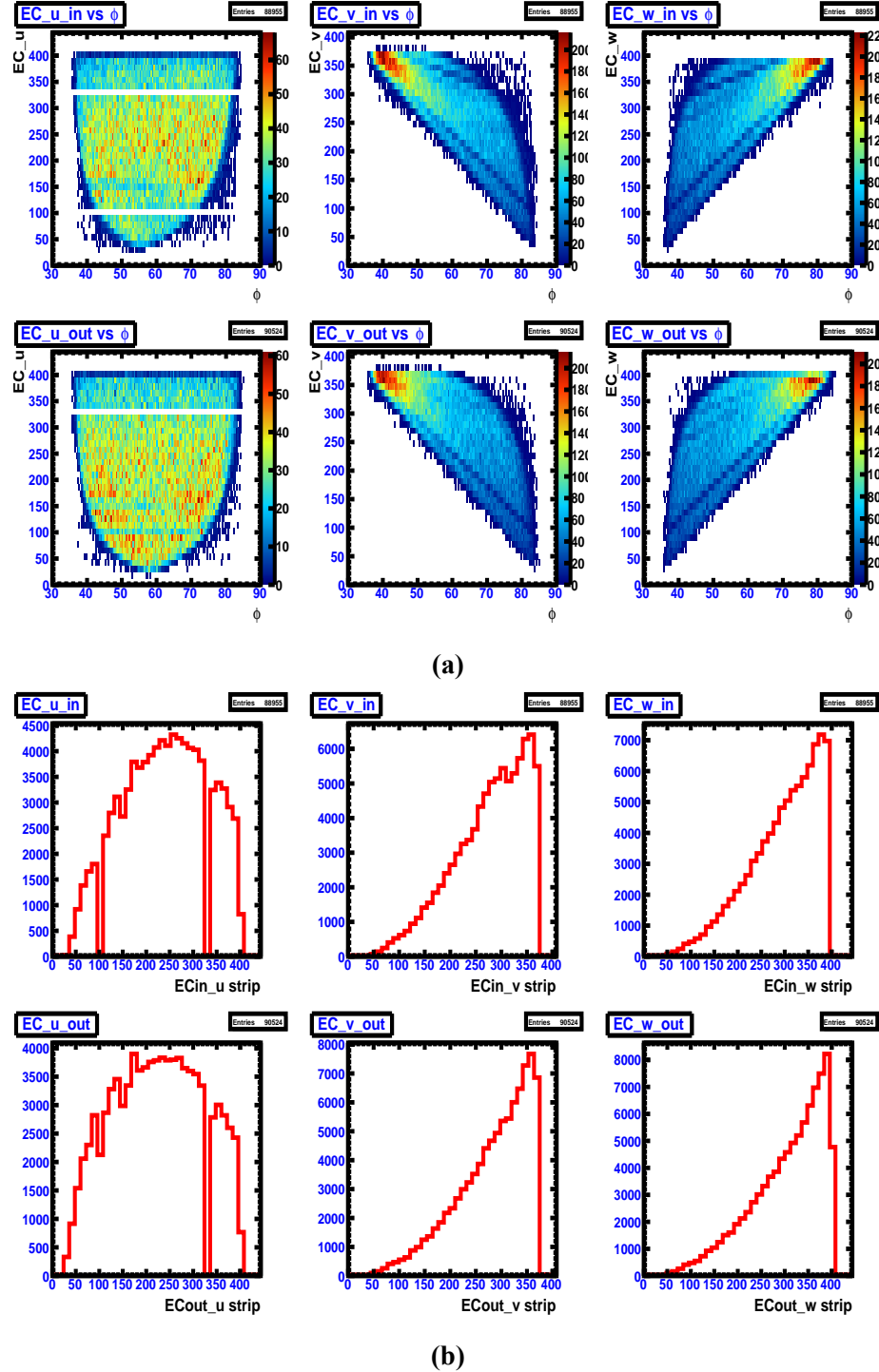


**Figure 45:** EC  $u, v, w$  strips vs.  $\phi$  for sector 2 with fiducial cuts and inefficient paddle knockouts applied to  $e^-$  data (45a), notation the same as Fig. 40. Number of hits vs. EC  $u, v, w$  strips for sector 2 with fiducial cuts and inefficient paddle knockouts applied to  $e^-$  data (45b). Notation same as in Fig. 41. Image source: [10]

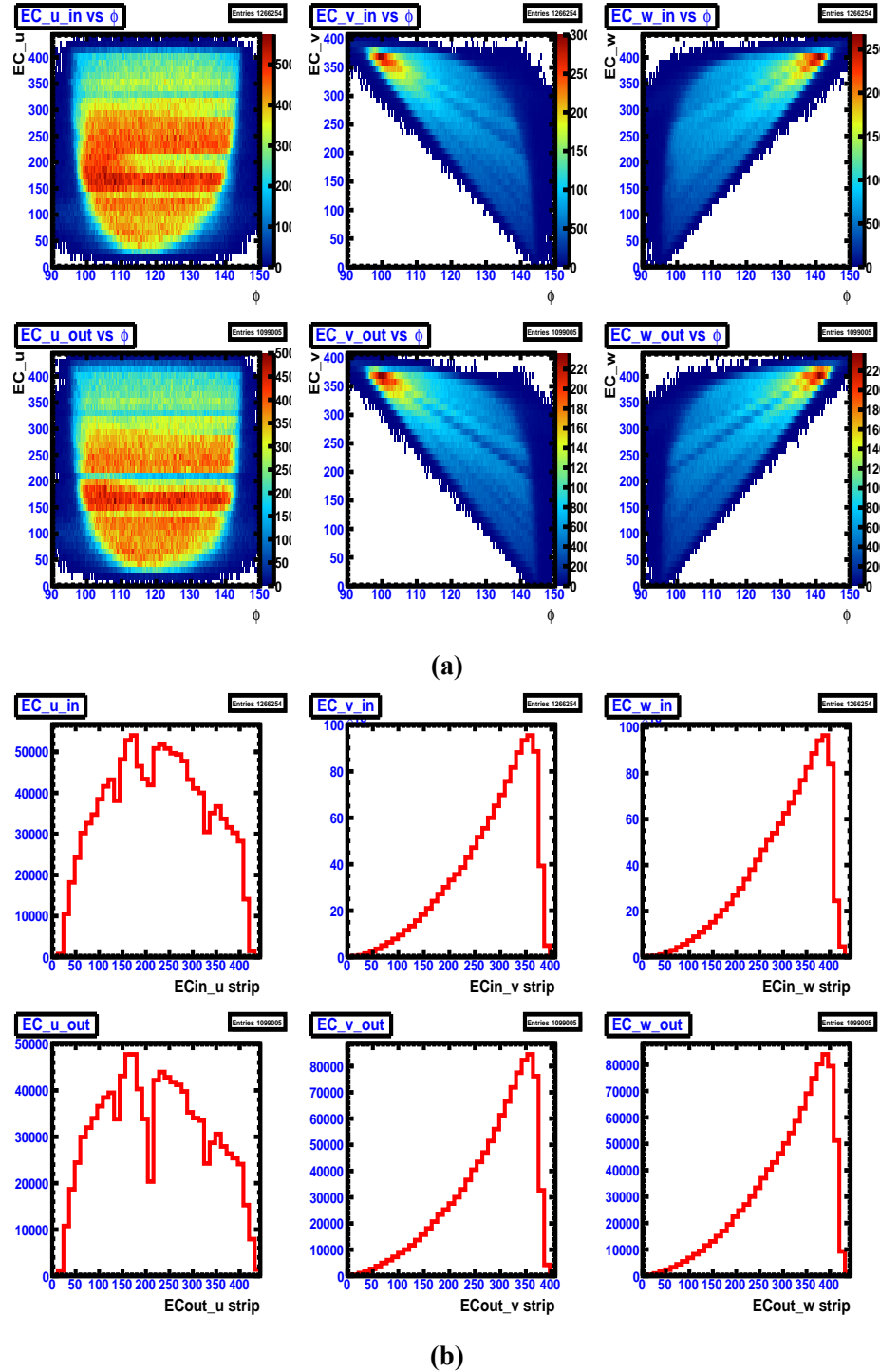


**Figure 46:** Inefficient EC  $u, v, w$  strips vs.  $\phi$  for sector 3 in CLAS  $e^-$  data (46a), notation the same as Fig. 38. Number of hits vs. inefficient EC  $u, v, w$  strips for sector 3 for  $e^-$  data (46b). Notation same as in Fig. 39. Image source: [10]

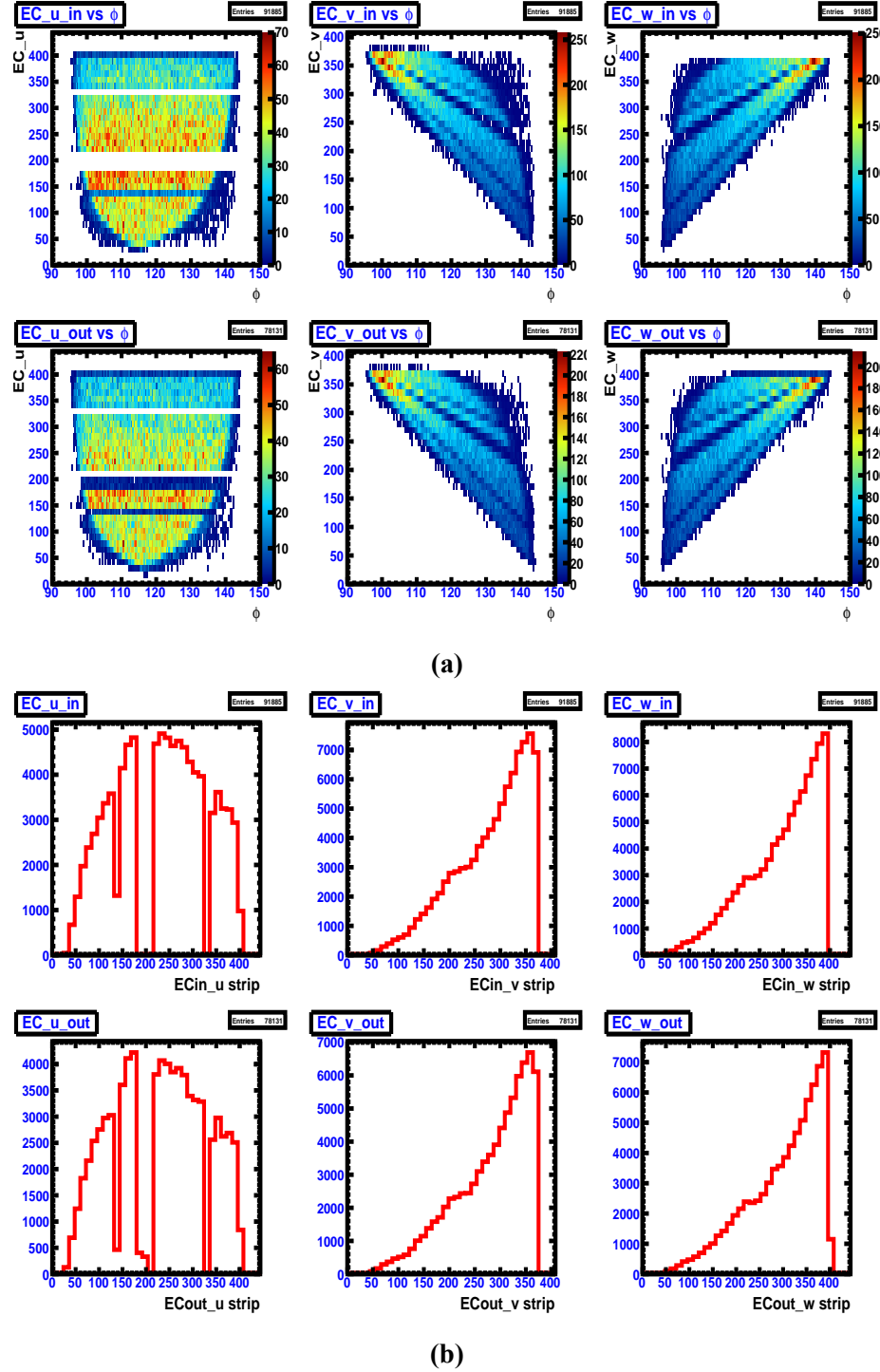


**Figure 47:** EC  $u, v, w$  strips vs.  $\phi$  for sector 3 with fiducial cuts and inefficient paddle knockouts applied to  $e^-$  data (47a), notation the same as Fig. 40. Number of hits vs. EC  $u, v, w$  strips for sector 3 with fiducial cuts and inefficient paddle knockouts applied to  $e^-$  data (47b). Notation same as in Fig. 41. Image source: [10]

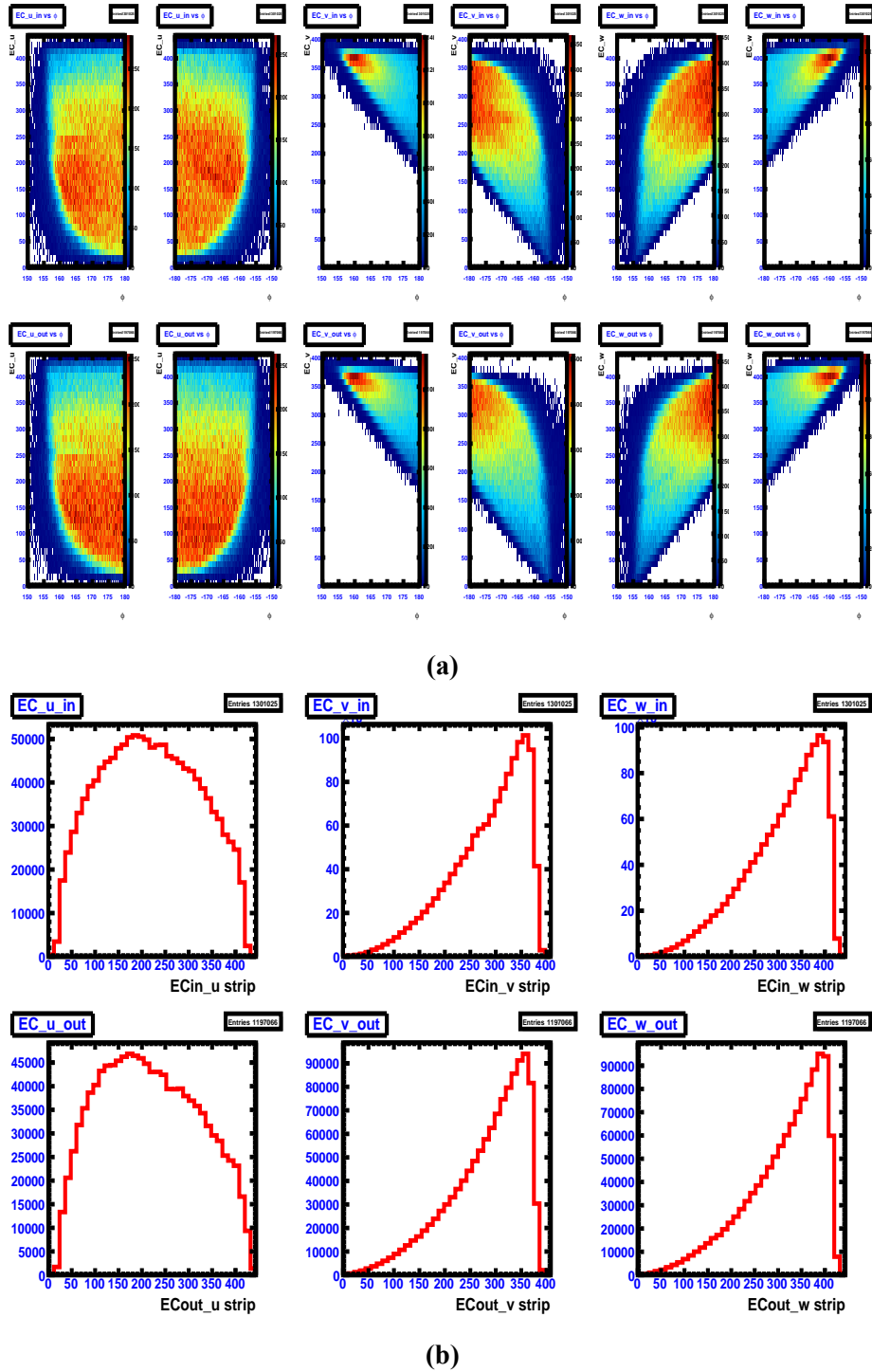


**Figure 48:** Inefficient EC  $u, v, w$  strips vs.  $\phi$  for sector 4 in CLAS  $e^-$  data (48a), notation the same as Fig. 38. Number of hits vs. inefficient EC  $u, v, w$  strips for sector 4 for  $e^-$  data (48b). Notation same as in Fig. 39. Fig. 48a is plotted with split  $\phi$  ranges due sector 4 having a defined  $\phi$  range from 150 to 180 and -180 to 150. Image source: [10]

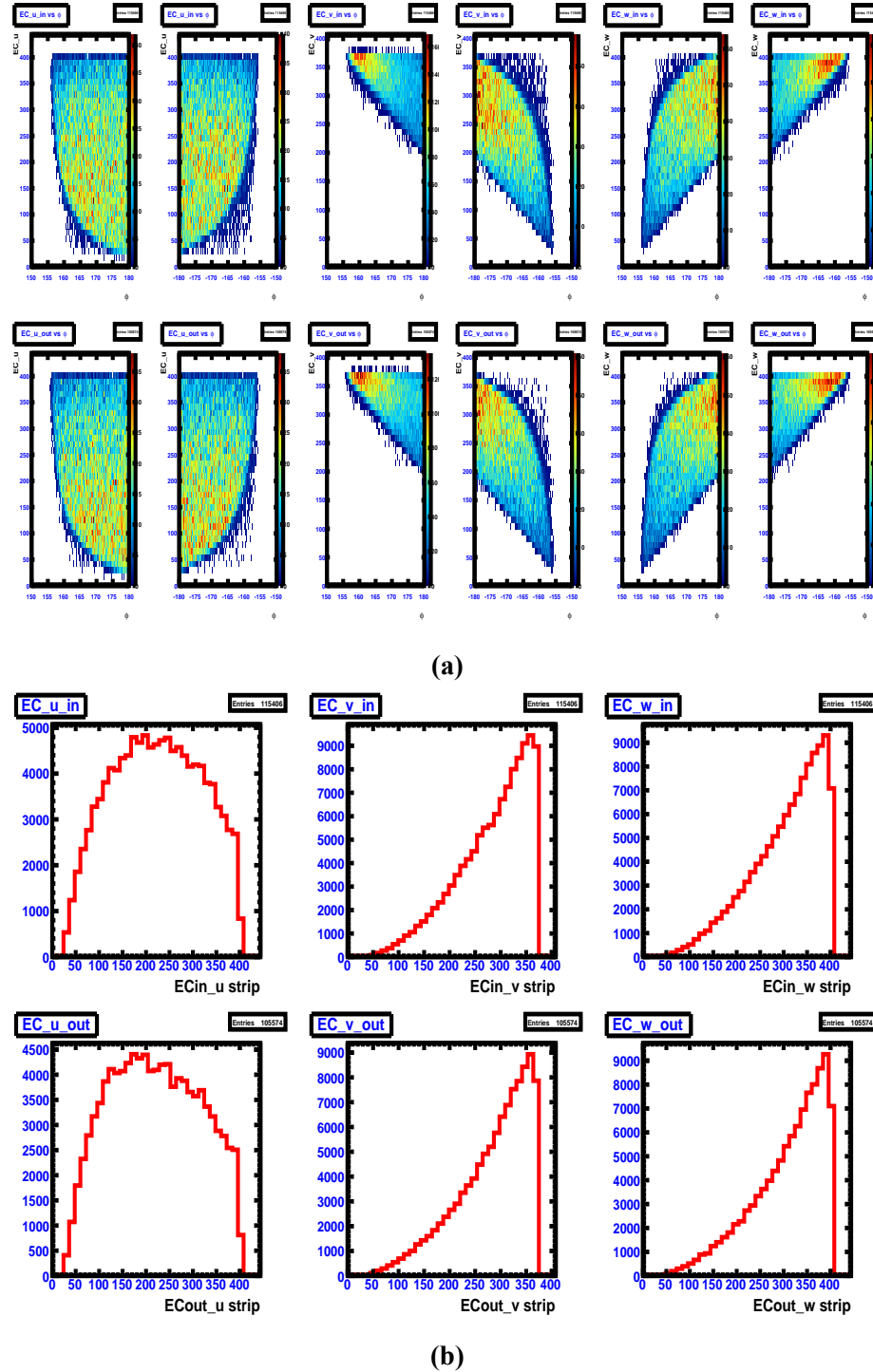


**Figure 49:** EC  $u$ ,  $v$ ,  $w$  strips vs.  $\phi$  for sector 4 with fiducial cuts and inefficient paddle knockouts applied to  $e^-$  data (49a), notation the same as Fig. 40. Fig. 49a is plotted with split  $\phi$  ranges due sector 4 having a defined  $\phi$  range from 150 to 180 and -180 to 150. Number of hits vs. EC  $u$ ,  $v$ ,  $w$  strips for sector 4 with fiducial cuts and inefficient paddle knockouts applied to  $e^-$  data (49b). Notation same as in Fig. 41. Image source: [10]

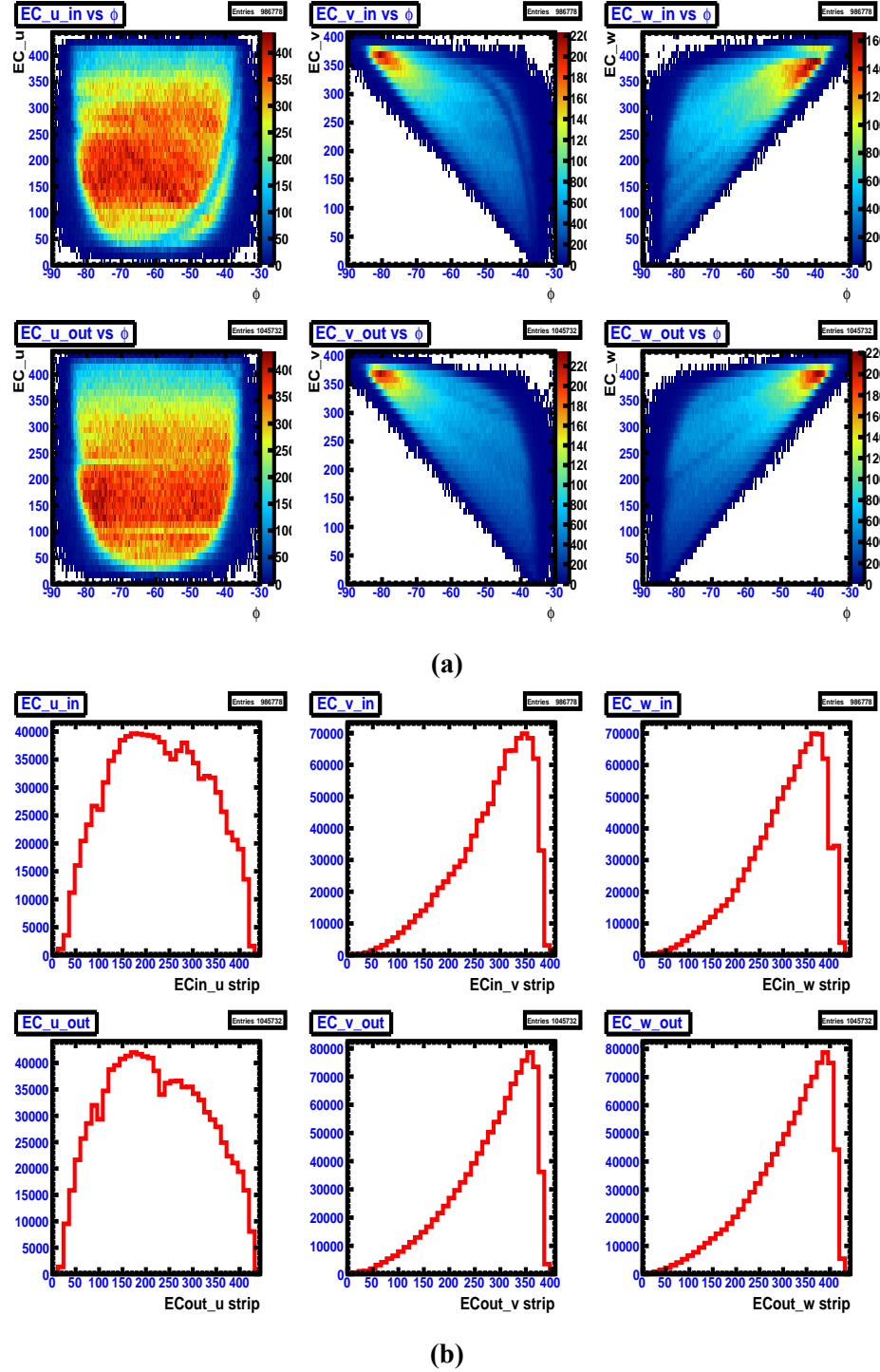


**Figure 50:** Inefficient EC  $u$ ,  $v$ ,  $w$  strips vs.  $\phi$  for sector 6 in CLAS  $e^-$  data (50a), notation the same as Fig. 38. Number of hits vs. inefficient EC  $u$ ,  $v$ ,  $w$  strips for sector 6 for  $e^-$  data (50b). Notation same as in Fig. 39. Image source: [10]

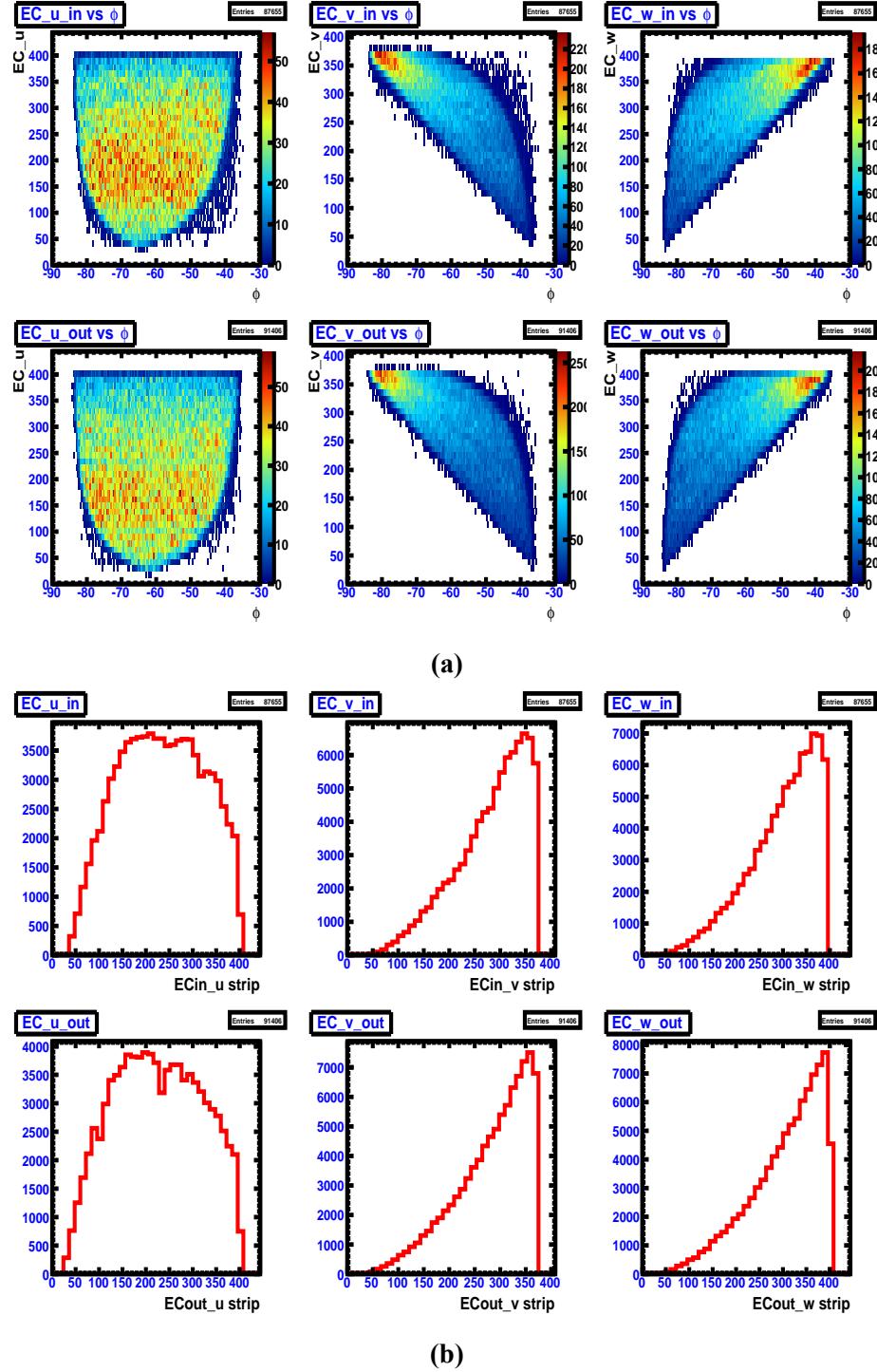


**Figure 51:** EC  $u, v, w$  strips vs.  $\phi$  for sector 6 with fiducial cuts and inefficient paddle knockouts applied to  $e^-$  data (51a), notation the same as Fig. 40. Number of hits vs. EC  $u, v, w$  strips for sector 6 with fiducial cuts and inefficient paddle knockouts applied to  $e^-$  data (51b). Notation same as in Fig. 41. Image source: [10]

The inefficiencies for the other 5 sectors are shown in Figs. 42 to 51. The final parameters for the EC strip cuts are listed in Tab. 20 and the parameters for the good EC fiducial range can be found in Tab. 21.

**Table 20:** EC UVW cut parameters. Table source: [10]

Sector	EC <sub>inner/outer</sub>	U
2	EC <sub>inner</sub>	$96 \leq U \leq 108 \parallel 324 \leq U \leq 336$
3	EC <sub>inner</sub>	$324 \leq U \leq 336 \parallel 180 \leq U \leq 216 \parallel 324 \leq U \leq 337$
2	EC <sub>outer</sub>	$324 \leq U \leq 336$
3	EC <sub>outer</sub>	$131 \leq U \leq 142 \parallel 204 \leq U \leq 216 \parallel 324 \leq U \leq 336$
5	EC <sub>outer</sub>	$180 \leq U \leq 192 \parallel 204 \leq U \leq 240$
		V
5	EC <sub>inner</sub>	$320 \leq V \leq 342 \parallel 254 \leq V \leq 242$
		W
1	EC <sub>inner</sub>	$312 \leq W \leq 324$
2	EC <sub>inner</sub>	$396 \leq W \leq 408$
3	EC <sub>inner</sub>	$396 \leq W \leq 408$
5	EC <sub>inner</sub>	$336 \leq W \leq 372 \parallel 288 \leq W \leq 312 \parallel 240 \leq W \leq 276$ $\parallel 168 \leq W \leq 228 \parallel 132 \leq W \leq 144$
6	EC <sub>inner</sub>	$W \geq 396$

**Table 21:** EC UVW good fiducial parameters. Table source: [10]

	U	V	W
EC Good Fiducial Range	$20 \leq U \leq 400$	$V \leq 375.0$	$W \leq 405.0$

To perform the procedure to knock-out bad EC paddles, use the header file:

```
clas/users/mkunkel/clas/g12_corrections/g12_ECxyz_2uvw.hpp
```

found in the SVN repository here:

<https://jabsvn.jlab.org/svnroot>

to convert the EC coordinates x, y, and z into u, v, and w EC coordinates. In the analysis program, the user needs to have the EC x, y and z coordinates, per particle, given by the TDPL bank for charged particles. For neutral particles the EC x, y and z coordinates are given by the ECHB bank. In the structure of *clasEvent.cc* there exists functions *ECpos()* and *ecPosition()* that return the EC x, y, and z coordinates for charged track and neutral tracks respectively. To use:

```
TVector3 partUVW = g12_ECxyz_2uvw(partECx, partECy, partECz);

double part_u = partUVW.X();
double part_v = partUVW.Y();
double part_w = partUVW.Z();
```

After the EC u, v, and w coordinates have been calculated, use the header file:

```
clas/users/mkunkel/clas/g12_corrections/g12_EC_knockout.hpp
```

found in the SVN repository here:

<https://jlabsvn.jlab.org/svnroot>

In the analysis program, the user needs to have the EC inner energy deposit, EC outer energy deposit, u, v, w, and particle sector to perform the EC bad paddle knock-out. To use:

```
g12_ec Knockout(partECin, partECout, part_u, part_v, part_w, part_sec);
```

which will return false if particle was knocked out, true if passed was not knocked out.

The paddle knock-out procedure described above must be applied to both data and simulation. The resolution of any topology will be affected asymmetrically and will have to be investigated for each individual analysis.

## 2.9 Beam Polarization

The electron beam produced with a polarized laser incident on gallium arsenide allows for longitudinal polarization of the electrons [14] and in turn, due to the bremsstrahlung process, circular polarization of the photon beam. The accurate measurement of the polarization transferred from the photon beam to the produced hyperons ( $C_x$  and  $C_z$ ) requires knowledge of the beam polarization. Such knowledge is ascertained by knowing the magnitude of incident electron-beam polarization, and the helicity orientation of the electron beam bunch responsible for the event (in the lab-frame). The Maximon-Olsen formula relating incident electron beam polarization, with the photon polarization is given by [15],

$$P_{\odot}(E_{\gamma}) = \frac{x(4-x)}{4-4x+3x^2} P_{elec} \quad (10)$$

where  $x = E_{\gamma}/E_{elec}$  is the ratio of photon energy,  $E_{\gamma}$ , to beam energy,  $E_{elec}$ . The g12 experiment ran with a constant electron energy of  $E_{elec} = 5.715$  GeV. (The actual electron beam energy was corrected on a run-by-run basis, see later section) The polarization of the electron beam was measured regularly using the a Møller polarimeter. The polarimeter measures electron polarization by making use of the helicity dependent nature of Møller scattering [16, 17]. The Møller measurements, summarized in Table ??, were performed regularly (every few days) during g12 and whenever we were notified of any beam changes. During the g12 running period, Hall B did not have the priority. As a result, the polarization of the beam was delivered as a byproduct as other Halls requirement, and fluctuates. However, the majority of the g12 runs has beam polarization close to 70% with a total uncertainty estimated to be 5%. The run-integrated and flux -weighted value of the polarization of a particular range of photon energies can be easily obtained by using the maximum-Olsen formula.

**Table 22:** The degree of longitudinal electron polarization ( $P_e$ ) between each Møller measurements. The uncertainties shown are statistical uncertainties.

Run Range	Møller Readout ( $P_e$ )
56355 – 56475	(81.221 $\pm$ 1.48)%
56476 – 56643	(67.166 $\pm$ 1.21)%
56644 – 56732	(59.294 $\pm$ 1.47)%
56733 – 56743	(62.071 $\pm$ 1.46)%
56744 – 56849	(62.780 $\pm$ 1.25)%
56850 – 56929	(46.490 $\pm$ 1.47)%
56930 – 57028	(45.450 $\pm$ 1.45)%
57029 – 57177	(68.741 $\pm$ 1.38)%
57178 – 57249	(70.504 $\pm$ 1.46)%
57250 – 57282	(75.691 $\pm$ 1.46)%
57283 – 57316	(68.535 $\pm$ 1.44)%

An important experimental aspect of g12 is that the electron-beam helicity was flipped at a rate around 30 Hz. While the helicity information was recorded and stored in the HEVT bank for each event, the convention for bit encoding has been known to change from real-time to delayed-time recording. Further considerations, such as the half-wave plate orientation also had to be accounted for.

The only sure way to pin down the absolute beam helicity orientation for our data was to analyze a well known helicity-dependent reaction. Well-established results in Ref. [18] in the beam-helicity asymmetry,  $I^\odot(\phi_{\pi^+}^{hel})$ , for the reaction,  $\gamma p \rightarrow p\pi^+\pi^-$ , were reproduced. The mentioned reaction was shown to have a specific helicity-frame defined  $\phi_{\pi^+}^{hel}$ -dependent structure. If the helicity convention was reversed then we would observe  $I^\odot(\phi_{\pi^+}^{hel}) \rightarrow -I^\odot(\phi_{\pi^+}^{hel})$ .

The sub-analysis we performed required exclusive  $p\pi^+\pi^-$  events in the final state. To ensure exclusivity we required zero missing energy and momentum within detector resolution. The helicity frame (shown in Fig. 52) was defined to be the rest frame of the hypothetical parent meson of the two pion system, with  $\hat{z}$  aligned along its center-of-mass defined momentum.  $\phi_{\pi^+}^{hel}$  is the angle between the proton-production plane, and the plane containing both pions. The beam helicity asymmetry is given by,

$$I_\odot = \frac{1}{P_\gamma} \frac{N^+ - N^-}{N^+ + N^-}, \quad (11)$$

where  $N^\pm$  indicates the number of events with positive (negative) photon helicity. Figs. 53-54 show the  $I_\odot(\phi_{\pi^+}^{hel})$  for g12 and in the analysis of [18]. The lab-frame electron helicity readout was taken from the HEVT bank (HEVT→hevt[0].TGRPRS). The results of our  $I_\odot(\phi_{\pi^+}^{hel})$  analysis and the previously published results showed a positive (negative) HEVT readout indicates positive (negative) photon helicity. **The following method, stored in**

```
/work/clas/clasg12/clasg12/clas6-trunk/include/gethelicity.h
```

```
int GetHelicity(clasHEVT_t *HEVT)
{
    int helicity = 0;
```

```

int readout = HEVT->hevt[0].trgps;
if(readout > 0) helicity = 1;
if(readout < 0) helicity = -1;
return helicity;
}

```

The reproduction of beam-helicity asymmetry for double charged pion production also served as a way to test the accuracy of the calculated photon polarization magnitude: both results' wave amplitudes were in good agreement. FIU and FSU independently measured the beam-helicity asymmetry and were in good agreement with each other. The pull distribution between FIU and FSU is shown in figure 55 and the pull distribution between FIU and g1c's results are shown in figure 56. Both FIU and FSU use approximately 15% of the entire dataset (due to the independence of the two measurements, their selection of the data is most likely not the same). Figure 56 shows good agreement between g12 and g1c's beam-helicity measurement.

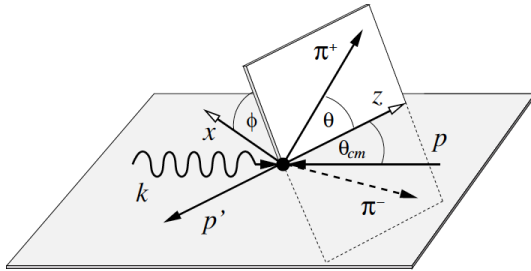


**Figure 52:** An illustration of the angle definitions used in the  $\gamma p \rightarrow \pi^+ \pi^- p$  sub-analysis.  $\theta_{cm}$  is defined in the center-of-mass frame.  $\theta$  and  $\phi$  are defined in the rest frame of the  $\pi^+ \pi^-$  system as the polar and azimuthal angles. The  $z$  direction is along the total momentum of the  $\pi^+ \pi^-$  system.

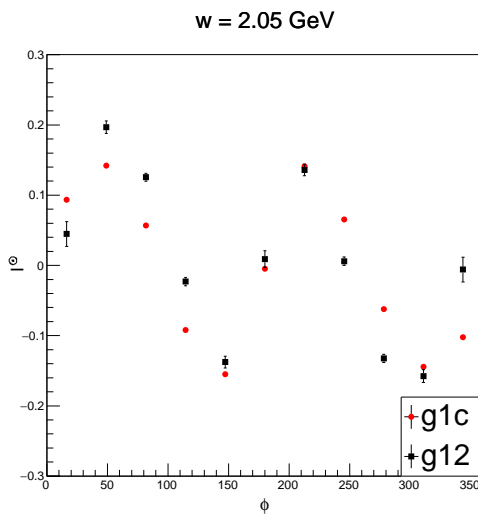


**Figure 53:**  $I_0(\phi_{\pi^+}^{hel})$  comparison between g12 (FIU) and g1c within the energy range  $W = 2.05 \pm .025$  GeV.

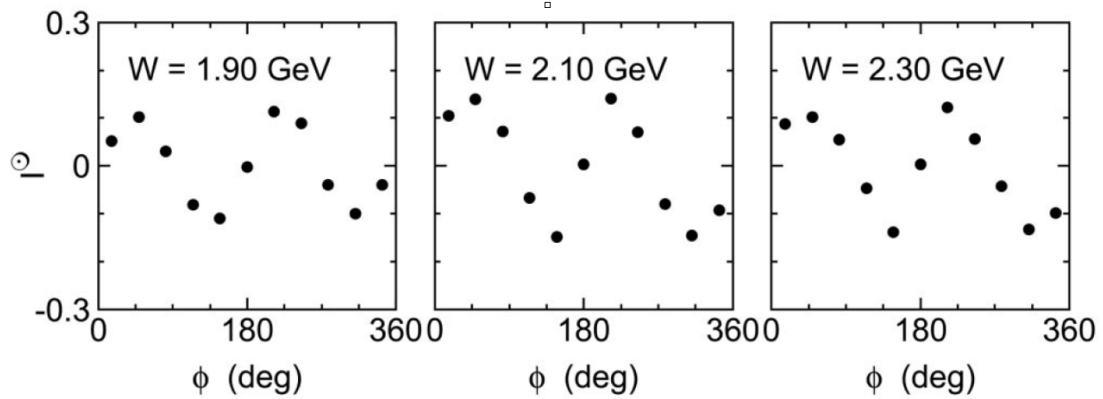


**Figure 54:**  $I_\infty(\phi_{\pi^+}^{hel})$  as measured in the previous analysis.  
 $I_\infty(\phi_{\pi^+}^{hel})$  as measured in the analysis [18]. The results of are shown in bins of  $W$  from 1.9 to 2.3 GeV.

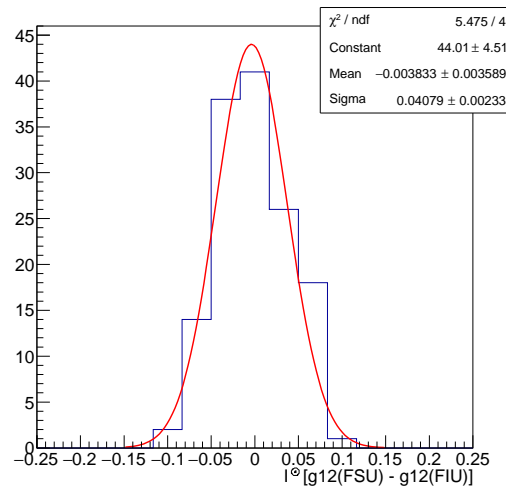


**Figure 55:** Pull distribution between FIU and FSU  $I_\infty$

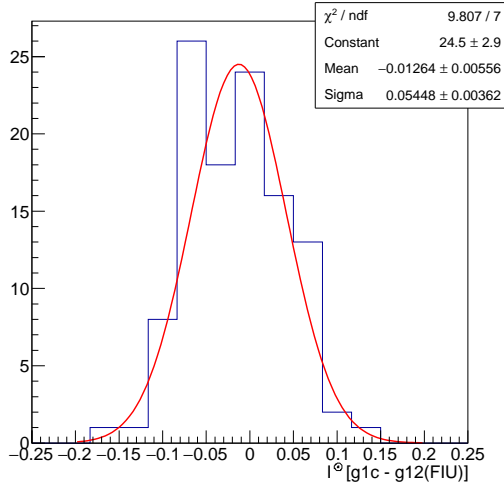


**Figure 56:** Pull distribution between g12 (FIU) and g1c  $I^0$

To conclude, the g12 beam polarization was measured with standard methods, and the validity of the photon helicity definition in the HEVT bank was double checked against existing experimental results and confirmed to be correct. All g12 measurements that utilizes the beam polarization refer to what has been summarized here.

### 3 Procedure for Data Analysis

The broad steps for analysis of a specific reaction in the *g12* data are:

1. determine event selection cuts to be used on a small subset of the data,
2. skim the “cooked” data and produce an ntuple which will include the four-momenta and a few other parameters needed for the final analysis,
3. tune the analysis on the data to get the final yields,
4. run simulations through the tracker/digitizer (`gsim`), smearing (`gpp`), track reconstruction (`a1c`), and the final analysis programs to obtain efficiencies and acceptances,
5. calculate the beam flux corresponding to the data analyzed,
6. tie the yields, acceptances and flux together to come up with a final answer and an absolute scaling.

One or more of these steps, or parts of these steps, may not be necessary for a given analysis and they do not have to be done this order. This section discusses where to find the various programs and files needed for each of these steps.

### 3.1 “Pass1” Cooking and Data Reconstruction

This section describes the process of reconstructing the raw data into almost-physics-ready form. Broadly speaking, the output of this procedure is the three-momenta of the detected final-state particles and various supporting measurements such as timing or energy deposit which is used for particle identification.

The reconstruction program `a1c` requires an environment variable to point to the correct run index for this run period. This can be set in a bash shell using the command:

```
export CLAS_CALDB_RUNINDEX=calib_user.RunIndexg12
```

The command to cook the gsim bos file using the `a1c` program is:

```
a1c -T4 -sa -ct1930 -cm0 -cp0 -X0 -d1 -F -P0x1bff -z0,0,-90 \
-Aprlink_tg-90pm30.bos -o3pi.a1c 3pi.gpp
```

which will produce BOS files similar to the “cooked” data. This is the same command to be used to *recook* raw data files. The options shown here will be slightly different for simulated data since *CLAS* does not treat simulation in exactly the same way as real data. This is a legacy issue that has been well documented in previous experiments and we will merely say that one will have to add the option “`-X0`” when running the `a1c` reconstruction program. This is mentioned again in Sec. 5.4 where we discuss the reconstruction of simulated data.

There was only one “physics” pass of the *g12* data, labeled `pass1`, which represents 99% of the reconstructable data taken. It was determined that tracking down that last 1% was not worth the effort. On JLab’s common user environment (CUE), the cooked data can be found here:

```
/mss/clas/g12/production/pass1/bos
```

and the raw data can be found here:

```
/mss/clas/g12/data/
```

Please see JLab’s SciComp help pages on how to get these files off the mass storage system. The source code for `pass1` was consistent with revision 4715 in the Subversion repository found here:

```
https://jlabsvn.jlab.org/svnroot/clas/trunk
```

which was linked against the 2005 version of the CERNLIB.

### 3.2 Obtaining Reconstructed Data

All reconstructed data resides in BOS files on the tape-silo at JLab under the directory:

```
/mss/clas/g12/production/pass1/bos
```

which contains the following subdirectories or “categories” used for event-sorting:

**1-1ckaon1ctrk** Events which have at least 2 charged tracks, one of which is a “possible kaon.” A possible kaon is either a track that the PART bank says is a kaon, or a high-momentum charged pion ( $> 2.0 \text{ GeV}$ ), or a really high momentum proton ( $> 3.0 \text{ GeV}$ ). The idea of this selection is to leave no kaon behind.

**2-2pos1neg\_not\_1ckaon1ctrk** Two-positive and one-negative (+ + −) inclusive events which are *not* included in *1-1ckaon1ctrk*. So, for example, if you wanted all (+ + −) events you would have to use both this category and *1-1ckaon1ctrk*.

**3-2ctrk\_not\_2pos1neg\_1ckaon1ctrk** Events with 2 or more charged tracks which do not qualify for either *1-1ckaon1ctrk* or *2-2pos1neg\_not\_1ckaon1ctrk*.

**4-not\_2ctrk\_2pos1neg\_1ckaon1ctrk** Physics events that do not fit into categories 1, 2, or 3.

**5-other** Non-physics events which may include scalers and such.

**6-1lepton** Redundant set of all events with a single “possible lepton” according to the

```
ClasParticle::isMaybeLepton()
```

method in the ClasEvent analysis suite.

**7-4ctrk** Redundant set of all four-charged track events.

**8-ppbar** Redundant set of all proton, anti-proton events according to the PART bank.

Note that the first five of these categories are *mutually exclusive and complete* while the last three are completely redundant and are provided for convenience. Non-physics events are included in the fifth (“other”) skim. If one wishes to synchronize these events with their data, they have some options. Perhaps the easiest is to process the raw data which is completely ordered. Timestamps could be used instead, provided they exist in the non-physics skim.

**This bears repeating since it is a non-standard sorting of the cooked data:** The five categories numbered 1 through 5 listed above consist of one and only one of *every* event recorded by the data acquisition during the g12 run period for the set of run which were deemed “good.” A specific single event will only be found in one of the first five categories. If you want to run on events that are described by category number 4 for example, you will have to include the data in categories 1 through 3 since these will also satisfy category 4 by design and by definition.

The total size of the reconstructed data is 211 TiB consisting of 26.2 billion triggers. The secondary skims (6–8) total 31 TiB. The breakdown of the size of the skims is shown in Table 23.

Typical analyses with g12 will start with the particles as identified in the PART bank as default in the ClasEvent analysis suite. This provides the basic four-momenta of the tracks and their identification which is based on mass calculated from the time-of-flight. The photon associated with the event is then taken from the TAGR bank and the one closest in-time with the tracks is usually taken.

For a deeper analysis, one can get information for specific hits in a given subsystem by following the pointers in the PART and TBID bank to the TBTR, SCRC, ECHB or other similar banks. Most of the relevant banks needed for this type of investigation are included in the cooked data though several raw banks were dropped to save space. To recover the missing banks one would have to go back to the raw data and recook using the a1c program though we anticipate this will be a rare event.

The following banks were written out to tape in the pass1 reconstructed data: CC CC01 CCPB CCRC CL01 DCPB DSTC EC EC1 EC1R ECHB ECPB ECPC ECPI ECS EPIC EVNT FBPM HBER HBID HBTR HEAD HEVT HLS LCPB MVRT PART RGLK S1ST SC SC1 SCPB SCR SCRC SCS ST1 STNO STN1 STPB

**Table 23:** Size of skims both in data-size and number of events.

size (TiB)	events (G)	skim
50	6.2	1-1ckaon1ctrk
31	3.8	2-2pos1neg_not_1ckaon1ctrk
68	8.4	3-2ctrk_not_2pos1neg_1ckaon1ctrk
62	7.7	4-not_2ctrk_2pos1neg_1ckaon1ctrk
0.26	0.033	5-other
17	2.1	6-1lepton
13	1.6	7-4ctrk
1	0.124	8-ppbar

STR STSN SYNC TAGE TAGI TAGR TBER TBID TBTR TDPL TGBI TGPB TGS TRGS TRKS TRL1. Note that the SEB-related banks (EVNT etc.) were written out. These may be used for any analysis though care should be taken not to mix these with the PART-related series of banks except where there is an apparent redundancy.

### 3.3 g12-Specific Corrections

The event reconstruction of a particle track in CLAS starts in region 1 of the DC after the track has gone through the target and start counter. To reconstruct the track back to the event vertex, additional energy loss from the target and start counter are included. The standard CLAS ELOSS package provides the required functionality as detailed in Ref. [19]. ELOSS corrects for the energy lost as charged tracks go from the event vertex through the beam pipe, target, and start counter using the Bethe-Bloch equation [20] to relate the material characteristics and path length to energy loss. These corrections are standard. In addition, g12 specific corrections have also been derived, including momentum correction and run-dependent beam energy correction. We performed several iteration to obtain the final corrections to remove the correlations between them. Overall, the impact of momentum corrections have been found to be small, consistent with all previous CLAS results. The beam energy corrections are necessary, after applying the energy loss and momentum correction, to align the masses of all known narrow states with the PDG values. With the final g12 correction procedures, these goals have been achieved. The details of these procedures are explained below:

#### 3.3.1 Final-State Particle Momentum Corrections

The momenta of the tracks as measured by the Drift-Chamber (DC) have a systematic shift within each sector as a function of azimuthal-angle  $\phi$  of one of the tracks. This can be seen in the “transverse momentum balance” plots shown in Fig. 57. The transverse momentum balance for a given particle is defined as the sum of the momentum of the other particles projected onto the line that is perpendicular to the beam having the same  $\phi$  angle as the given particle minus its momentum transverse to the beam.

The procedure used is described in the *CLAS* note for the momentum correction of the g9b dataset[21], though we choose to show the transverse (to the beam) momentum balance which is slightly more sensitive to this feature. The resulting transverse momentum and missing mass balance are shown in Figs. 58 and 59.

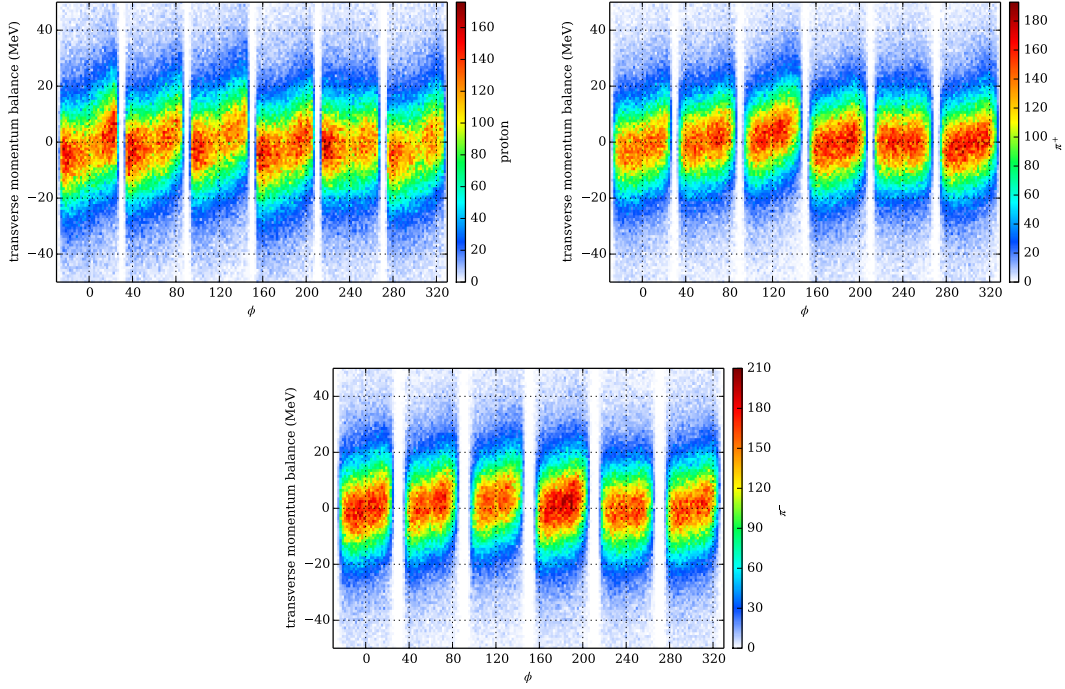


**Figure 57:** Transverse momentum balance of exclusive  $p\pi^+\pi^-$  events as a function of azimuthal angle  $\phi$  of each track before momentum corrections for the proton,  $\pi^+$  and  $\pi^-$ .

The final *g12* momentum corrections are in the *clas6* trunk:

```
svn co https://jlabsvn.jlab.org/svnroot/clas/trunk/pcor/g12pcor
```

The code to use the momentum corrections should look something like this:

```
#include "g12_pcor.hpp"

string parms_dir = "/group/clas/parms";

/// load up momentum correction parameters
clas6::g12::MomentumCorrection Pcor(parms_dir);

///begin loop over charged particles
{
    float newp = Pcor.pcor(oldp, phi, geant3_pid);
}
```

Where *geant3 pid* is the particle ID (according to *geant3*) for  $\pi^+$ ,  $\pi^-$ ,  $p$ ,  $K^+$  or  $K^-$ .

A simultaneous fit was done by adding a correction to the momenta of each particle for each sector which was linear in  $\phi$ . The result of the correction is shown in Fig. 58.

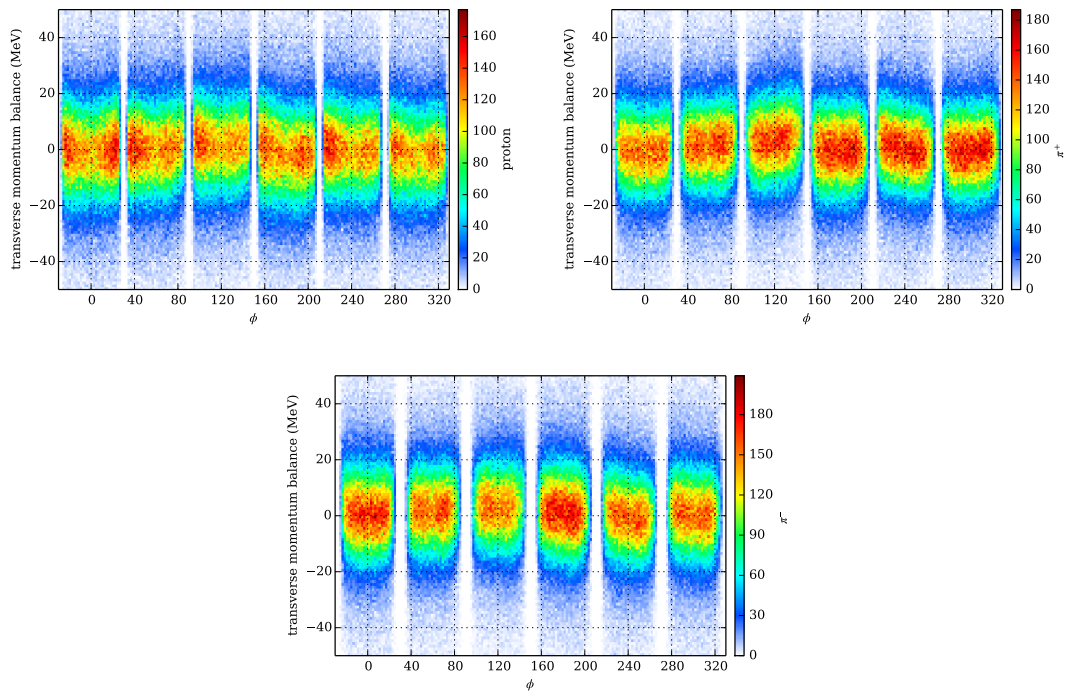


**Figure 58:** Transverse momentum balance of exclusive  $p\pi^+\pi^-$  events as a function of azimuthal angle  $\phi$  of each track after momentum corrections for the proton,  $\pi^+$  and  $\pi^-$ .

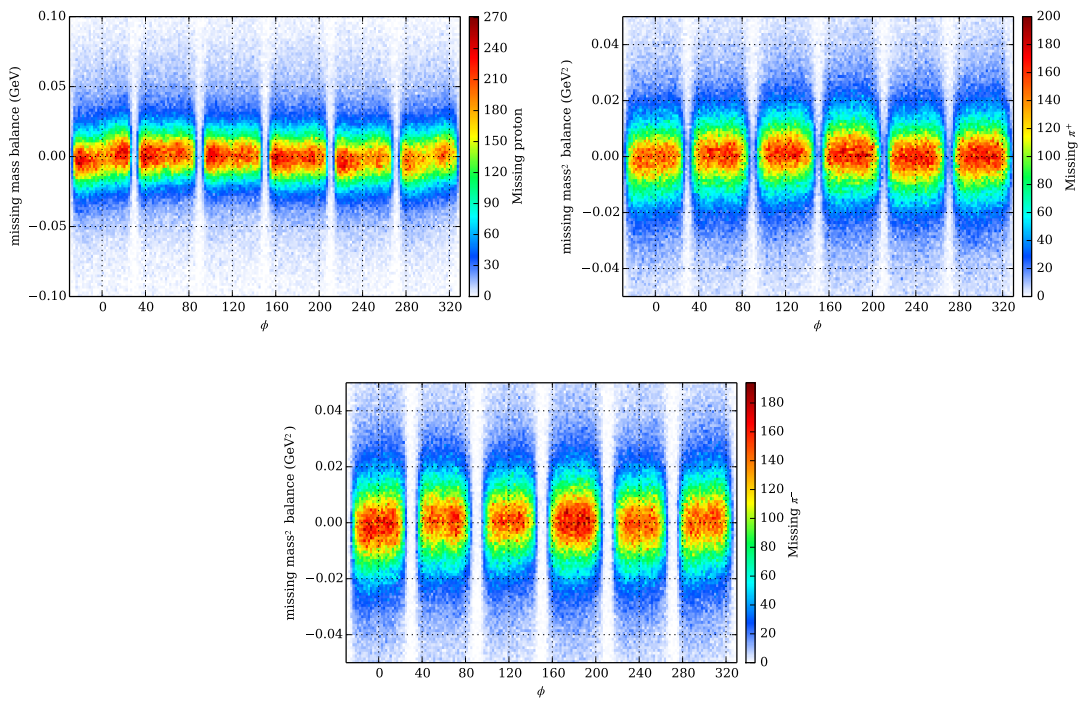


**Figure 59:** Missing mass (and mass-squared) balance of exclusive  $p\pi^+\pi^-$  events as a function of azimuthal angle  $\phi$  of each track after momentum corrections for the proton,  $\pi^+$  and  $\pi^-$ .

### 3.3.2 Photon Tagger Calibration and Beam Energy Corrections

The *g12* experiment had a complicated trigger which presented difficulties that were ironed out as described in this section. The problem was first noticed by *g12* participants at the analysis level in which missing particle masses were systematically low. It was realized while investigating the issue that the low missing particle mass was dependent on the run number and varied in mass as much as 10 MeV. There were also features in the run dependent missing mass that showed a constant low mass (run<56550) followed by a jump in mass which remained constant (56550<run<56920) until another jump in mass which seemed to produce a mass closer the PDG mass (run>56920). To analyze and correct for the cause of the problem, two topologies were chosen to isolate the missing particles, proton and neutron. The first topology;

$$\gamma p \rightarrow \pi^+ \pi^- p \quad (12)$$

was chosen to be the correction topology, while the second topology;

$$\gamma p \rightarrow \pi^+ \pi^+ \pi^- [n] \quad (13)$$

was chosen to verify the corrections obtained from eq. 12. The skim consisted of the data for the correction was of one CLAS PID  $\pi^+$ , one CLAS PID  $\pi^-$ , one CLAS PID proton and nothing else. Exclusive cuts were then placed by requiring the missing energy,  $M_E(p\pi^+\pi^-) < 0.025$  GeV and the missing mass squared of  $M_x^2(p\pi^+\pi^-) < 0.015$  GeV<sup>2</sup>. These cuts assure all events chosen exclude the topology;

$$\gamma p \rightarrow p \pi^+ \pi^- [\pi^0]$$

since the mass squared of  $\pi^0 = 0.0182$  GeV<sup>2</sup>.

The first step chosen was to verify whether the “energy-loss” correction was causing the discrepancy, this can be seen in Figs. 60, 61. It was concluded that the “energy-loss” correction was not the culprit of the problem. From Fig. 60, two runs were chosen, 56515 and 57130, in which the difference in the missing mass was  $\approx 10$  MeV. Inspecting the invariant mass,  $M(\pi^+\pi^-)$ , Fig 62, for runs 56515 and 57130 revealed only a mass deviation of approximately 1.4 MeV, which suggested that the problem with the *g12* data stream is most likely in the photon beam energy.

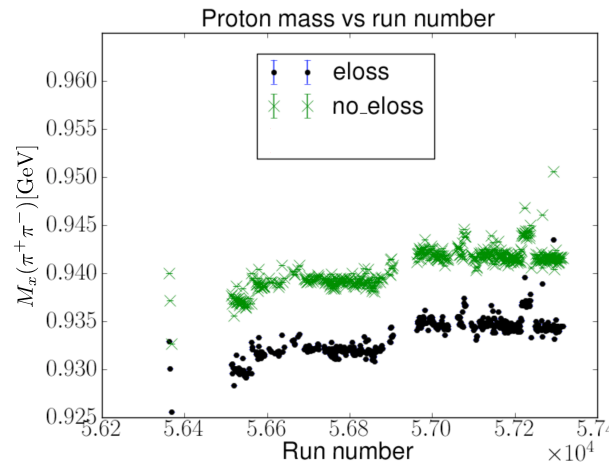


**Figure 60:** Plot of  $g12$  run number vs. proton mass with and without the “energy-loss” applied. See text for details.

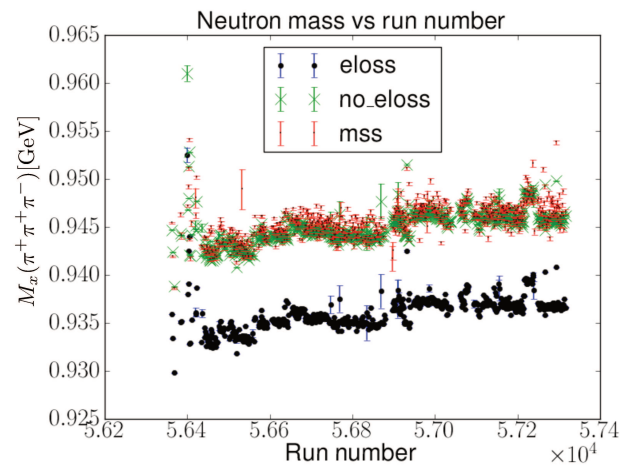


**Figure 61:** Plot of  $g12$  run number vs. neutron mass with and without the “energy-loss” applied. See text for details.  
Image Source: [1]

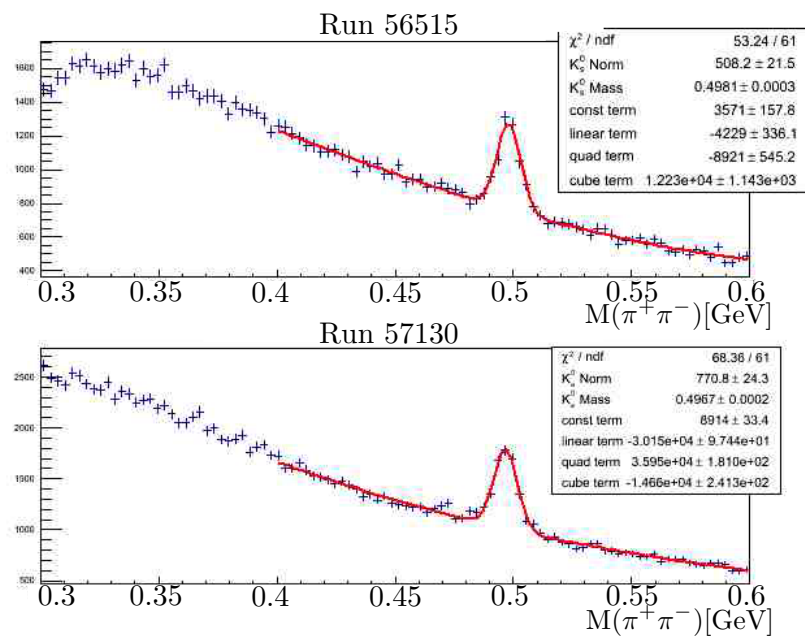


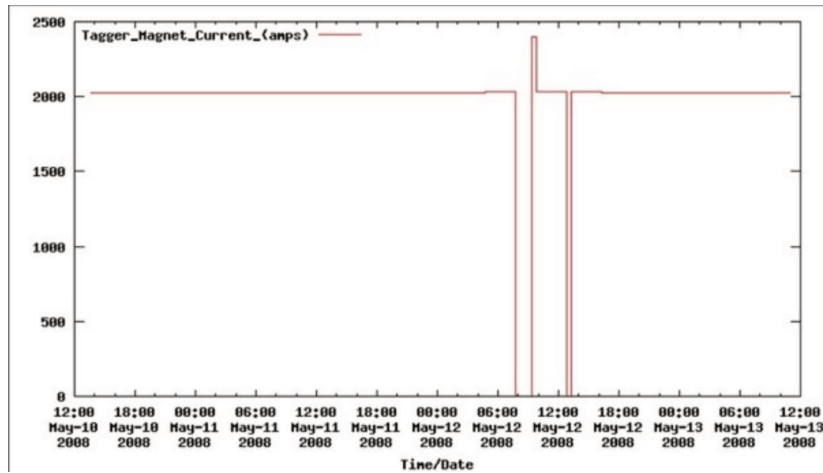
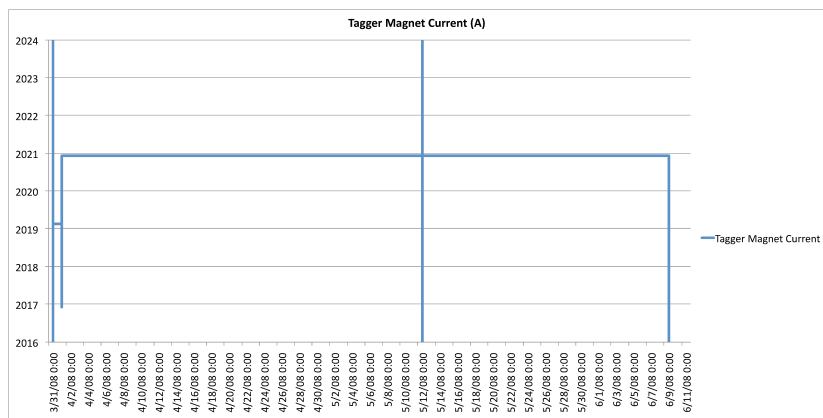
**Figure 62:** Plot of Kaon mass for runs 56515 and 57130.

Now that it is known that the photon beam energy is the cause of the issue, it must be known the cause of the photon beam error. Several quantities that the tagger subsystem are subjected to were analyzed, first being the tagger magnet current which, according to the EPICS Fig 63, remain constant but showed that around run = 56920 (May 12, 2008) the tagger magnet was shut-off. The tagger magnet shut-off was done because work had to be done in the hall, however after the tagger magnet was turned on, the current was set to its previous setting. A further investigation into the tagger magnet was performed by private communication with the accelerator group chief Arne Freyberger, Fig 64 shows the data the accelerator group had for the tagger magnet which confirms that the tagger magnet current was stable throughout the running of g12. The next beam quantity analyzed was the beam **energy** delivered by CEBAF, again through private communication with the accelerator group chief Arne Freyberger it is shown in Fig. 65 that the electron beam **energy** remained constant throughout the g12 experiment.

The next quantity investigated was the positioning of the tagger dump. Since the radius of curvature a charged particle travels is proportional to the magnetic field, Eq. 14, this quantity is suitable.

$$p = q(v \times B)r \quad (14)$$

The y-positioning of the tagger dump jumps on or about May 12, 2008, Fig. 66. This would effect how the tagger recorded the scattered electron. A cause for the change in y-positioning can only be due to the magnetic field changing. The phenomena in magnetism that allows for a steady current but a change in magnetic field is known as hysteresis, Fig. 67 illustrates that on the x-axis there is a constant current that is associated with 2 distinct magnetic fields shown on the y-axis of Fig. 67.

**Figure 63:** Tagger magnet current according to EPICS**Figure 64:** Tagger magnet current according to accelerator group**Figure 65:** Electron beam **energy** delivered to hall *b*(red) and hall *c* (green) according to accelerator group during the time of *g12* running

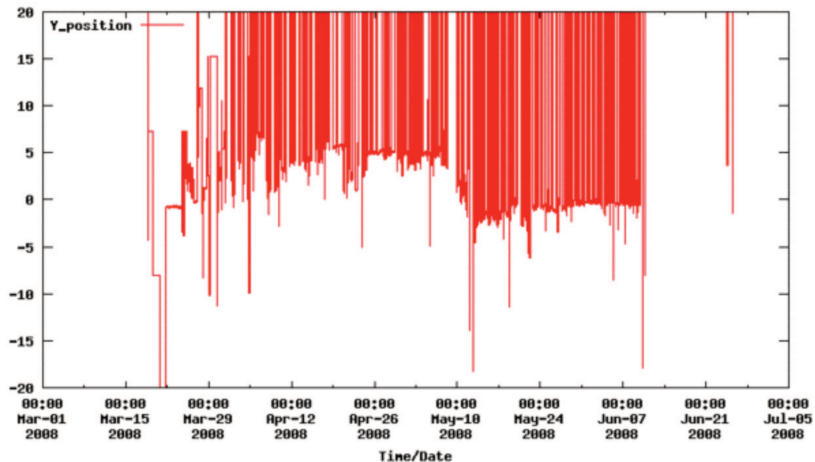


**Figure 66:** Tagger dump y-positioning according to EPICS

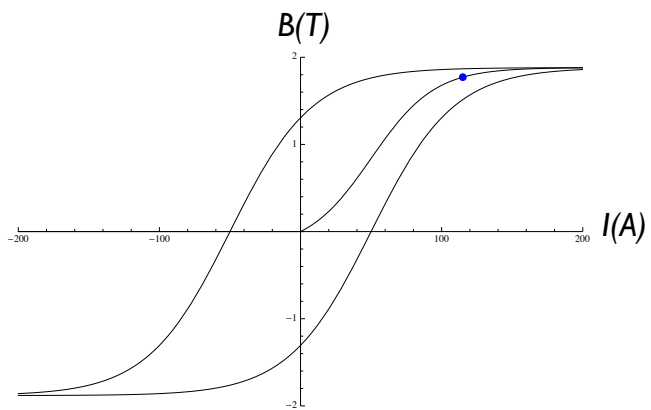


**Figure 67:** Plot depicting the process of hysteresis. For the a current of strength  $I$ , there could exist two magnetic fields of strength  $B$ . Image source: [10]

Hysteresis would affect the scattered electron and was corrected for in the following manner. Lets let

$$P_{\pi^+} + P_{\pi^-} = P_{\pi^+ \pi^-}$$

therefore

$$(P_\gamma + P_{\text{target}} - (P_{\pi^+ \pi^-}))^2 = m_p^2 \quad (15)$$

$$P_\gamma^2 + P_{\text{target}}^2 + P_{\pi^+ \pi^-}^2 + 2P_\gamma P_{\text{target}} - 2P_\gamma P_{\pi^+ \pi^-} - 2P_{\text{target}} P_{\pi^+ \pi^-} = m_p^2 \quad (16)$$

collecting terms of  $P_\gamma$  to one side and using  $P_{\text{target}}^2 = m_p^2$  and  $P_\gamma^2 = 0$

$$P_{\pi^+ \pi^-}^2 - 2P_{\text{target}} P_{\pi^+ \pi^-} = 2P_\gamma(P_{\pi^+ \pi^-} - P_{\text{target}}) \quad (17)$$

From this using eq. 16 in 4-vector notation

$$P_\gamma = P_{E_0} - P_e$$

where  $P_{E_0}$  is the beam energy delivered from CEBAF as recorded in the RUNC bank and  $P_e$  is the scattered electron in the *bremssstrahlung* process that is recorded by the tagger. From eq. 16 the only known quantities are  $P_{E_0}$  and  $P_\gamma$ . Applying a scalar correction to  $P_e$  as  $xP_e$  and solving for  $x$  for all known quantities, eq. 17 simplifies to;

$$x = \frac{P_{E_0}(P_{\text{target}} - P_{\pi^+ \pi^-}) + P_{\pi^+ \pi^-}^2/2 - P_{\text{target}} P_{\pi^+ \pi^-}}{(P_{E_0} - P_\gamma)(P_{\text{target}} - P_{\pi^+ \pi^-})} \quad (18)$$

To reduce statistical fluctuations  $\frac{1}{10}$  of run 56515 was analyzed to obtain the correction factor  $x$ . The correction factor was fitted to a 3<sup>rd</sup> order polynomial  $\pm 0.008$  from the mean of the peak to establish an accurate measurement of the peak, this is shown in Fig. 68. After the correction factor was extracted for run 56515, it was applied to both the topologies listed in Eq. 12 and Eq. 13 by recalculating the photon beam energy as

$$\begin{aligned} E_e &= E_{\text{CEBAF}} - E_\gamma \\ E_\gamma^{new} &= E_{E_0} - E_e * x. \end{aligned}$$

Figures 69 and 70 illustrate the missing mass topologies after beam correction and shows that the new calculated missing mass is less than 1 MeV from PDG values. Since both the missing proton mass and missing neutron mass were adjusted properly to the correct mass by using the same beam correction factor, it shows that the correction factor is independent of topology and therefore must be applied to all g12 analyses. The procedure to calculate  $x$  was repeated for every run in g12, Fig. 71, with  $\frac{1}{10}$  of the data used. To validate the corrections of the entire g12 data set, the missing neutron mass was recalculated for each run, shown in Fig. 72, using several correction schemes, i.e. a scheme of just “energy-loss” corrections, a scheme of “energy-loss” and momentum corrections (JTG PCor), a scheme of “energy-loss”, momentum corrections (JTG PCor) and beam corrections (MK BeamCor) and a scheme of “energy-loss” and beam corrections (MK BeamCor). It can be seen in Fig. 72 that the only scheme that sufficed was the combination of “energy-loss” and beam corrections.

To correct for run by run shifts in the beam energy, use the header file in:

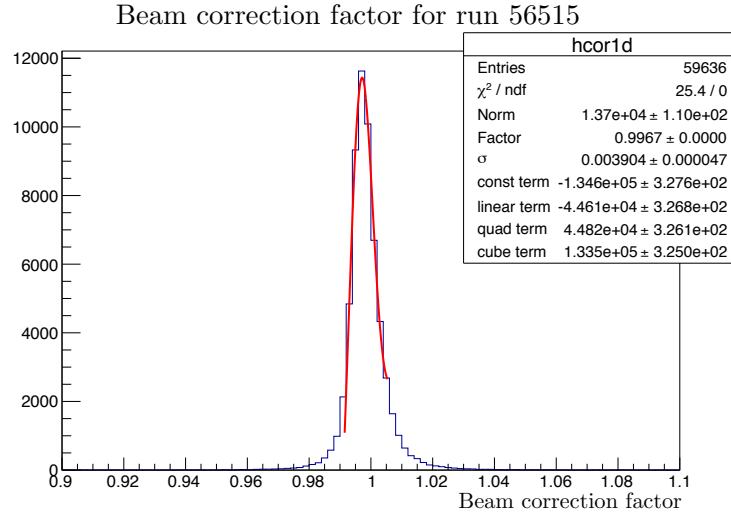


**Figure 68:** Beam correction factor for run 56515. The fit is a 3<sup>rd</sup> order polynomial  $\pm 0.008$  from the mean of the peak.  
Image source: [10]

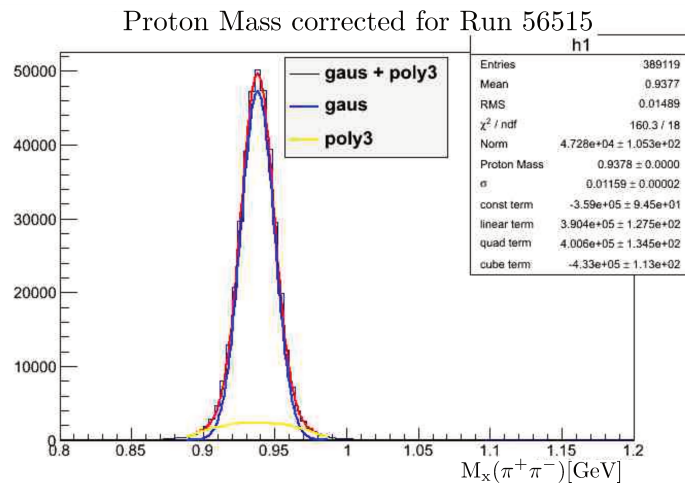


**Figure 69:** Plot of proton mass for runs 56515 after beam correction was applied. PDG mass for the proton is 0.938272 GeV/c. Image source: [10]

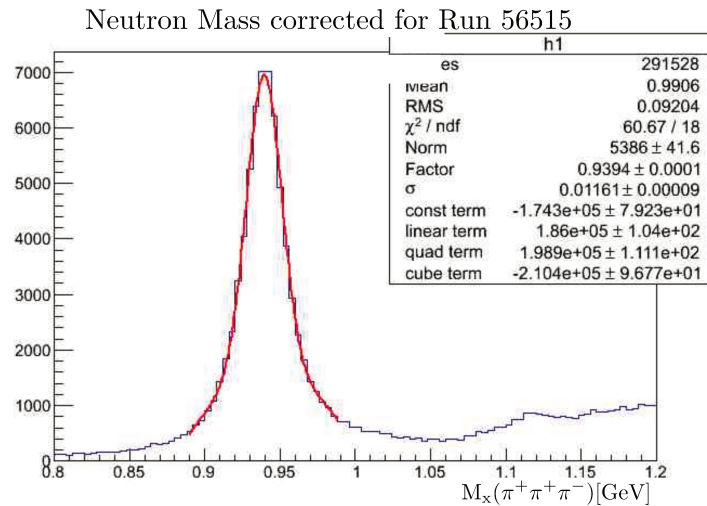


**Figure 70:** Plot of neutron mass for runs 56515 after beam correction was applied PDG mass for the neutron is 0.939565 GeV/c. In the plot, the "Factor" is the fitting parameter for the neutron mass. Image source: [10]

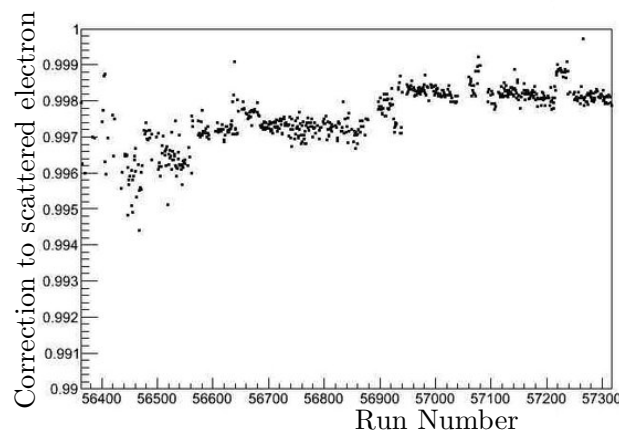


**Figure 71:** Plot of correction factor calculated for the entire g12 run set. Image source: [10]

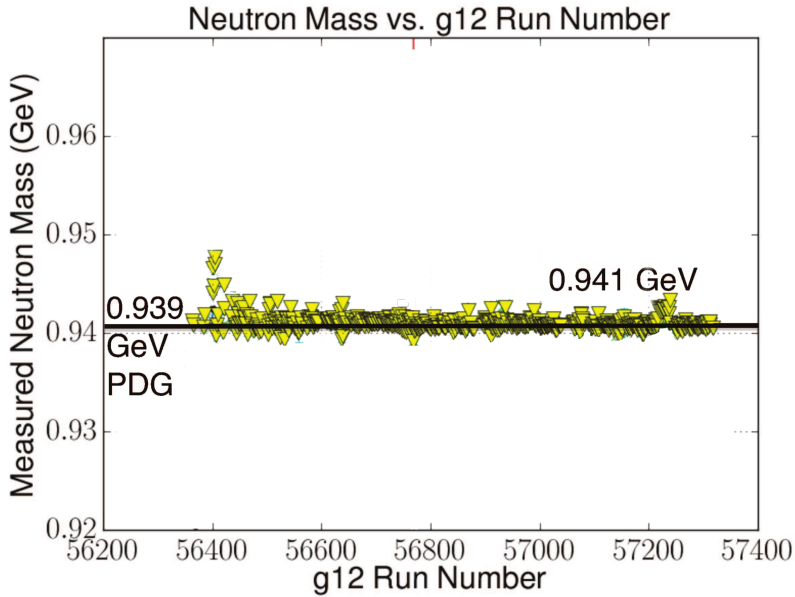


**Figure 72:** Plot of missing neutron mass using various corrections. The yellow triangles show a missing neutron mass with only “energy-loss,” beam corrections and momentum corrections applied. PDG mass for the neutron is 0.939565 GeV/c.

[https://jlabsvn.jlab.org/svnroot/clas/trunk/analysis/g12/g12\\_ecor.hpp](https://jlabsvn.jlab.org/svnroot/clas/trunk/analysis/g12/g12_ecor.hpp)

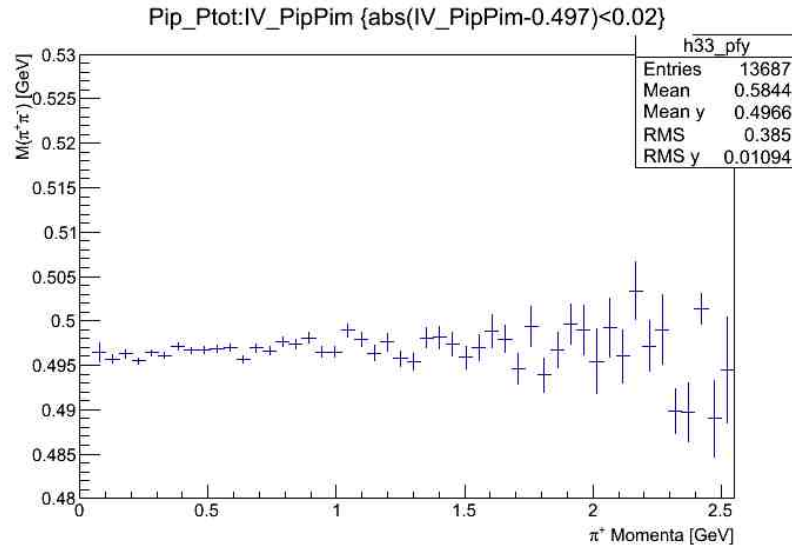
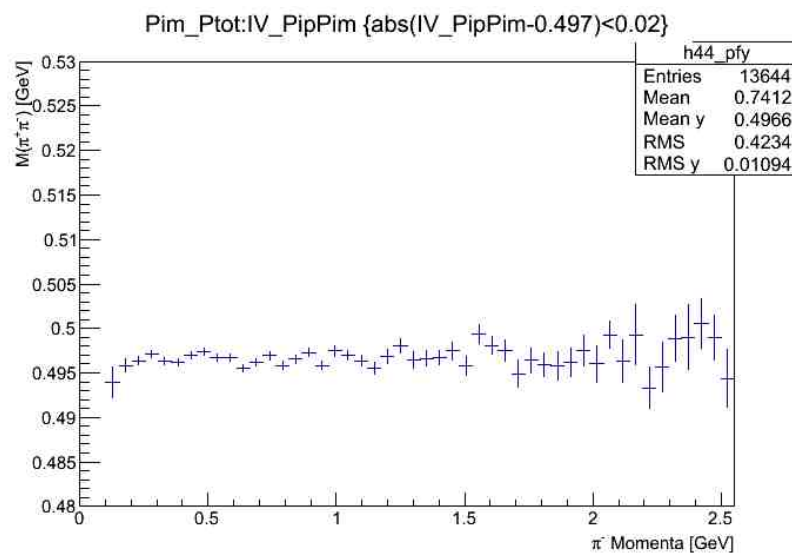
In the analysis program, the user needs to have the run number of the event and the uncorrected beam energy, then use:

```
corrected_beam_energy(int run, double uncorrected_beam_energy)
```

The final and standard g12 photon-energy corrections were re-derived after the momentum correction and e-loss corrections were applied. Here are some plots (Figs. ??) depicting the stability of the  $K_s$  mass throughout the  $\pi^+$  and  $\pi^-$  momenta.

Here are some plots (Figs. ??) depicting the stability of the  $K_s$  mass throughout the  $\pi^+$  and  $\pi^-$  the  $\pi^+$  and  $\pi^-$  polar angle  $\theta$  and azimuthal angle  $\phi$ .

For some bins of  $\theta$  and  $\phi$  the  $K_s$  mass difference (from PDG value) are more than 1 MeV, this is due to the number of entries and the fit performed for that bin. It should be noted that for all plots involving the  $K_0$  mass distribution, a distance of closest approach cut was placed on the  $\pi^+\pi^-$ .

**Figure 73:**  $K_s$  mass vs.  $\pi^+$  momentum.**Figure 74:**  $K_s$  mass vs.  $\pi^-$  momentum.

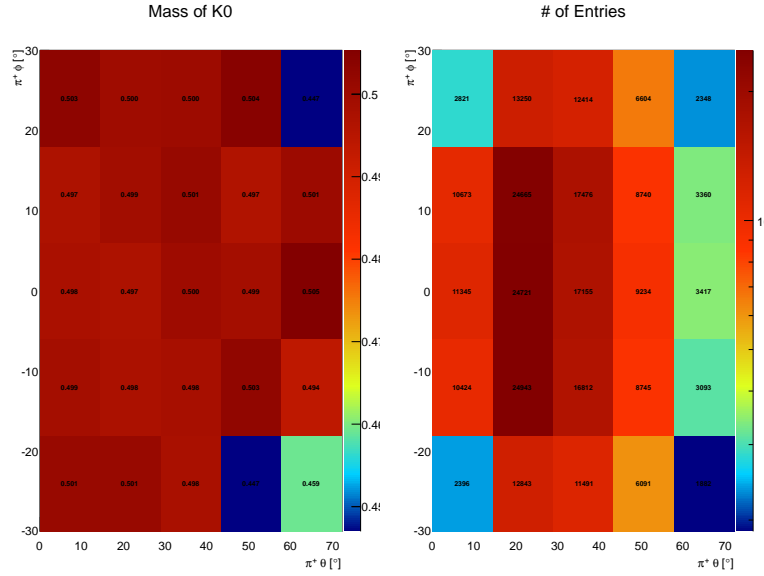


**Figure 75:** (Left)  $\pi^+$  mod( $\phi$ ) vs.  $\theta$  with the centroid of the  $K_s$  mass labeled. (Right)  $\pi^+$  mod( $\phi$ ) vs.  $\theta$  with the number of entries for the centroid of the  $K_s$  mass labeled.

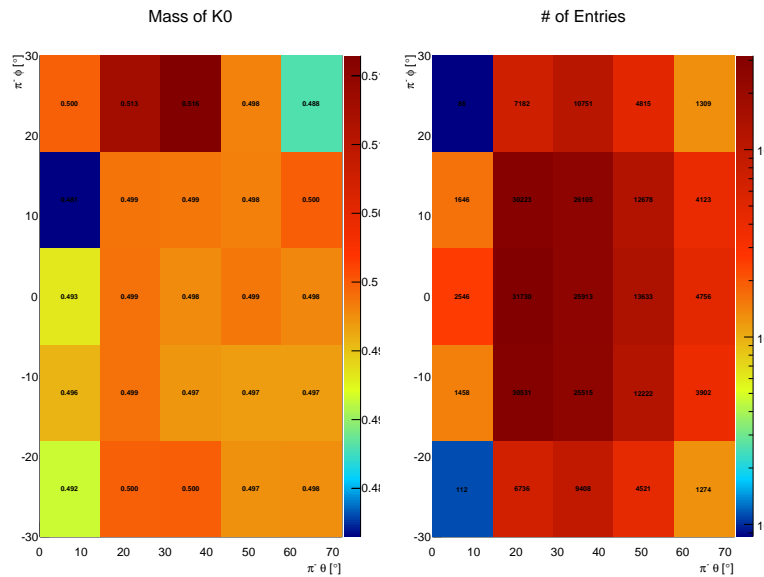


**Figure 76:** (Left)  $\pi^-$  mod( $\phi$ ) vs.  $\theta$  with the centroid of the  $K_s$  mass labeled. (Right)  $\pi^-$  mod( $\phi$ ) vs.  $\theta$  with the number of entries for the centroid of the  $K_s$  mass labeled.

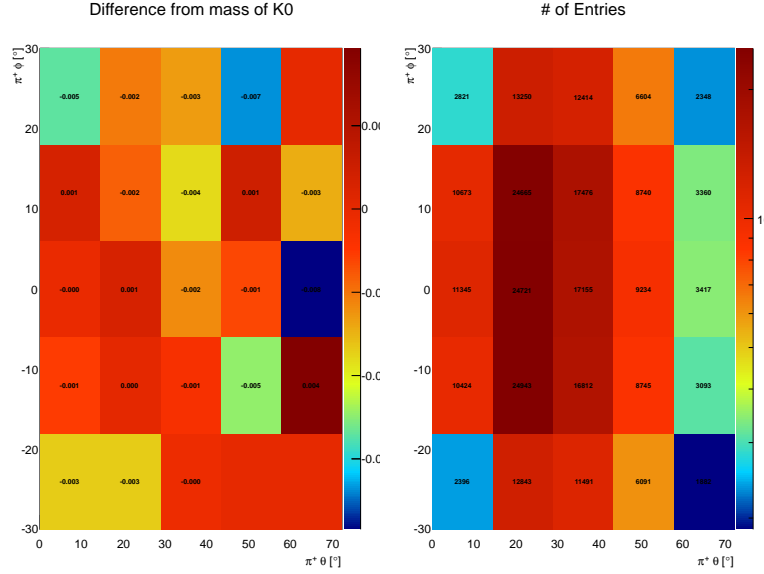


**Figure 77:** (Left) $\pi^+ \text{ mod}(\phi)$  vs.  $\theta$  with the mass difference from PDG value of the  $K_s$  mass labeled. (Right) $\pi^+ \text{ mod}(\phi)$  vs.  $\theta$  with the number of entries for the mass difference of the  $K_s$  mass labeled.

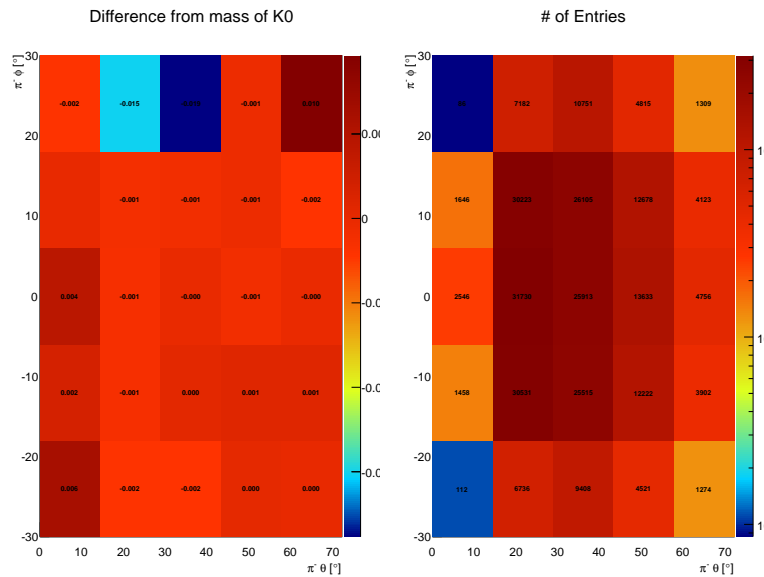


**Figure 78:** (Left) $\pi^- \text{ mod}(\phi)$  vs.  $\theta$  with the mass difference from PDG value of the  $K_s$  mass labeled. (Right) $\pi^- \text{ mod}(\phi)$  vs.  $\theta$  with the number of entries for the mass difference of the  $K_s$  mass labeled.

### 3.4 General Features of Lepton Data in g12

To identify electrons and positrons properly in CLAS, quantities obtained from the CC and EC are used to reject charged pions. The CC collects the number of photo-electrons caused by Cerenkov radiation and the EC records the energy deposition of electrons/positrons as well as photons. A previous CLAS experiment *g7* analyzed the properties of medium modifications from the decay of vector mesons through the lepton decay channel. This experiment derived a set of cuts for identifying electron/positrons pairs in CLAS by employing specific cuts to the number of photo-electrons (NPE) detected in the CC, a match in azimuthal angle  $\phi$  from a charged track in the DC to the  $\phi$  of the CC, as well as comparing the momentum of the charged track to the energy deposited in the EC. These cuts can be found in Table 24. To validate the *g7* electron/positron

**Table 24:** Cuts applied to the CC and EC to perform electron/positron PID. Table source: [10]

Subsystem	Quantity	Cut
CC	# of photo-electrons (NPE)	$NPE > 2.5$
	$DC \phi & CC \phi$	$DC \phi = CC \phi$
EC	$q^\pm$ momentum threshold ( $p_{\text{thres}}$ ) & EC deposited energy ( $E_{\text{calo}}$ )	$p_{\text{thres}}^{\text{high}} < E_{\text{calo}} < p_{\text{thres}}^{\text{low}}$

PID scheme for *g12*, a comparison of the CC and EC quantities was performed for all charged tracks CC/EC hit signatures and while selecting events from  $\pi^0$  decay. To separate the  $\pi^0$  events from the  $\pi^+\pi^-$  events, all charged pions were assigned the mass of electrons and cuts were placed on the missing energy of  $\gamma p \rightarrow p e^+ e^-$  as well as a cut on the missing mass squared of  $\gamma p \rightarrow p$ , values found in Table 25. A graphical depiction of the cuts applied to separate  $\pi^0$  events from the  $\pi^+\pi^-$  events is seen in Fig. 79. The values of the threshold

**Table 25:** Cuts applied to separate  $\pi^0$  events from  $\pi^+\pi^-$  events. Table source: [10]

Cut Topology	Topology Quantity	Value
$\gamma p \rightarrow p e^+ e^-$	Missing Energy ( $M_E$ )	$> 0.075 \text{ GeV}$
$\gamma p \rightarrow p$	Missing mass squared ( $M_x^2$ )	$< 0.0779 \text{ GeV}^2$ for $\pi^0$ events $> 0.0779 \text{ GeV}^2$ for $\pi^+\pi^-$ events

momentum are calculated from empirical studies and are based upon calculations using the momentum obtained from the DCp under the following criteria;

$$\begin{aligned} p_{\text{thres}}^{\text{low}} &= \alpha p * (p + EC_{P\_LO})/p \\ p_{\text{thres}}^{\text{high}} &= \alpha p * (p + EC_{P\_HIGH})/p \end{aligned}$$

where  $EC_{P\_LO} = -0.3$ ,  $EC_{P\_HIGH} = 0.5$  and

$$\alpha p = \begin{cases} .23 * p + .071p^2 - .032p^3, & p < 1.0 \text{ GeV} \\ 0.272p, & p > 1.0 \text{ GeV} \end{cases}$$

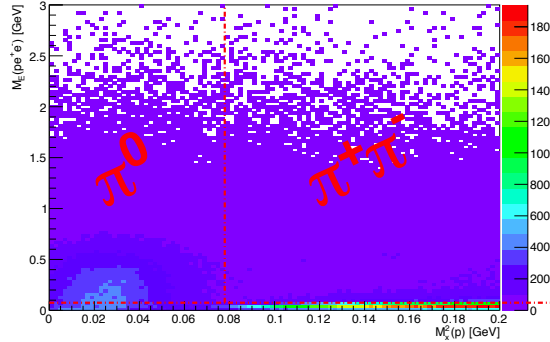


**Figure 79:** Plot of missing mass squared of off proton (horizontal) vs. missing energy of proton  $e^+e^-$  (vertical). The red dashed vertical line depicts the  $\pi^+\pi^-$  threshold mass cut while the horizontal red dashed line represents the missing energy cut-off used to separate  $\pi^+\pi^-$  from  $\pi^0$ . Image source: [10]

There are more and more restrictive cuts one can always do to try to clean up a lepton signal, but the general CC, TOF, and  $EC_{total}$  are the most robust. After that you can make further cuts on  $EC_{inner}$  and/or  $EC_{outer}$  at the users discretion. The g7 lepton cuts were the standard `isLepton()`, plus a  $> 45$  MeC  $EC_{inner}$  cut, see Ref. [22].

### 3.4.1 CC Comparison

The NPE measured by the CC for all positron/electron ( $e^+/e^-$ ) candidates can be seen in Fig 80. The sharp decline prior to 2.5 NPE is due to photo-electrons created by electron/positrons, pions traveling through the CC or pions producing delta-electrons which pass through the CC. Delta-electrons are created as an effect of the ionization of gases that could be present when the pion travels through the DC. These types of electrons are typically lower in momentum than the electrons obtained from particle decays in CLAS and thus should emit less NPE per unit length.

Through mass conservation the particles for the  $\pi^0$  events must be  $e^+/e^-$  pairs. In comparison to fig. 80, fig. 81 plots the NPE measured by the CC for all  $e^+/e^-$  pairs for  $\pi^0$  events selected as shown in fig. 79. It can be seen that the sharp decline prior to  $NPE = 2.5$  is reduced leaving mostly electrons or positrons signatures in the CC concluding that the g7 CC NPE cut is valid for identifying  $e^+/e^-$  pairs while rejecting  $\pi^+\pi^-$  pairs.

Using the current cuts of NPE and hit angle, the suppression of di-leptons was sufficient without including additional cuts on the CC such as a timing comparison to the TOF. This method of lepton PID, involving di-leptons, was established during the g7 run period. Further g12 analyses that involve single lepton PID could include this as a cut.

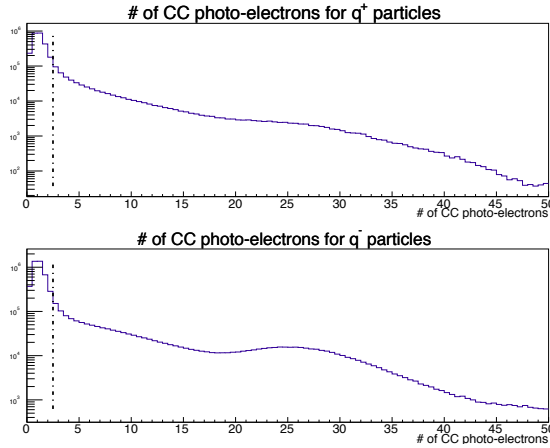


**Figure 80:** Plot of NPE measured by CLAS CC subsystem for positron/electron candidates top/bottom respectively. The dashed dotted vertical line depicts the cut applied if using the  $g7$  lepton PID scheme. Image source: [10]

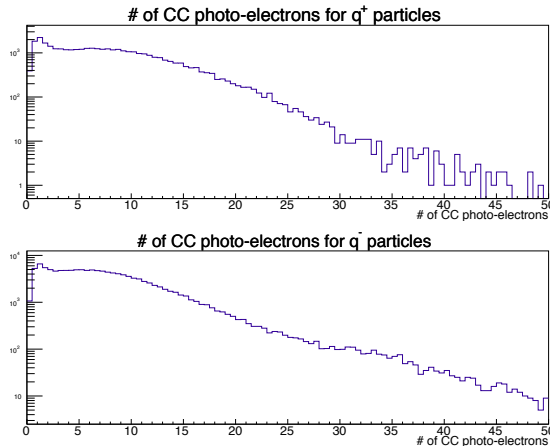


**Figure 81:** Plot of NPE measured by CLAS CC subsystem when selecting  $\pi^0$  events seen in Fig 79, positron/electron candidates top/bottom respectively. Image source: [10]

### 3.4.2 EC Comparison

Similarly to the CC comparison, figures 82, 83, 86, 87 depict the  $p_{\text{thres}}^{\text{low}}$  and  $p_{\text{thres}}^{\text{low}}$  cuts listed in Table 24 for the  $q^-$  and  $q^+$  tracks respectively. After  $\pi^0$  event selection, seen in figures 84, 85, 88, 89, the bulk of  $e^+e^-$  events reside within the region of the cut acceptance therefore it is evident that the  $g7$  EC cuts are valid for identifying  $e^+e^-$  pairs. The following four plots are for electron( $e^-$ ) PID validation of the  $g7$  EC cuts described in Table 24.

Figures 86–89 are for positron ( $e^+$ ) PID validation of the  $g7$  EC cuts described in Table 24.

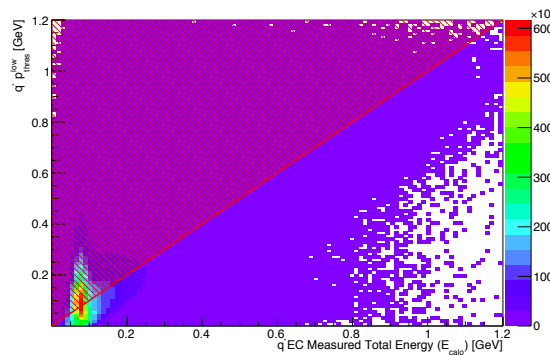


**Figure 82:** Plot of energy deposited measured by EC vs. track momentum  $p_{\text{thres}}^{\text{low}}$  for negative charged tracks. The red region depicts the cut that would reject events in the  $g7$  lepton EC PID scheme. Image source: [10]

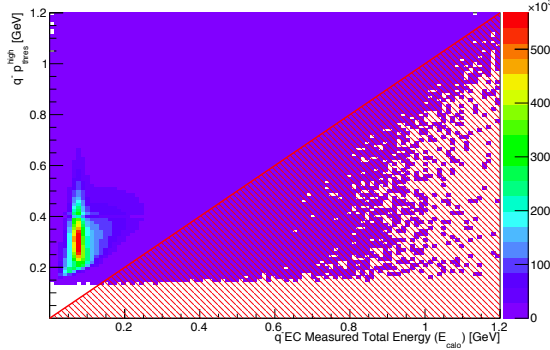


**Figure 83:** Plot of energy deposited measured by EC vs. track momentum  $p_{\text{thres}}^{\text{high}}$  for negative charged tracks. The red region depicts the cut that would reject events in the  $g7$  lepton EC PID scheme. Image source: [10]

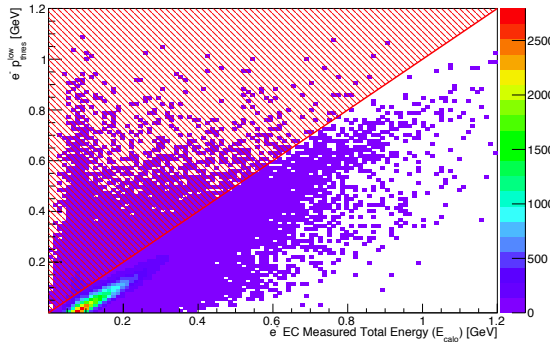


**Figure 84:** Plot of energy deposited measured by EC vs. track momentum  $p_{\text{thres}}^{\text{low}}$  for electrons from  $\pi^0$  events without the  $g7$  lepton EC PID scheme applied. The red region depicts the cut that would reject events in the  $g7$  lepton EC PID scheme. Image source: [10]

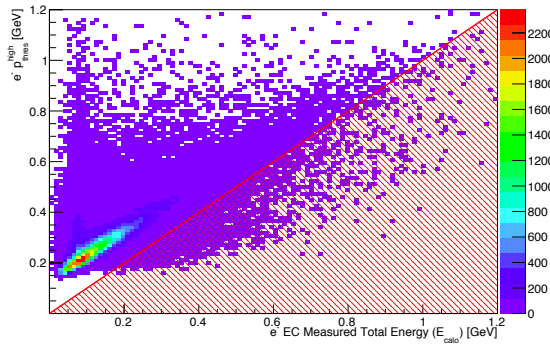


**Figure 85:** Plot of energy deposited measured by EC vs. track momentum  $p_{\text{thres}}^{\text{high}}$  for electrons from  $\pi^0$  events without the  $g7$  lepton EC PID scheme applied. The red region depicts the cut that would reject events in the  $g7$  lepton EC PID scheme. Image source: [10]

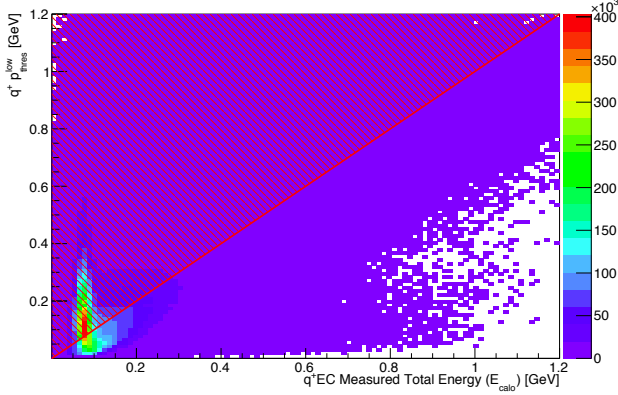


**Figure 86:** Plot of energy deposited measured by EC vs. track momentum  $p_{\text{thres}}^{\text{low}}$  for positive charged tracks. The red region depicts the cut that would reject events in the  $g7$  lepton EC PID scheme. Image source: [10]

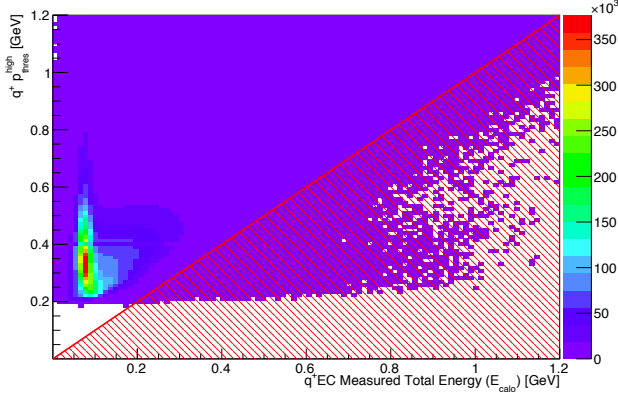


**Figure 87:** Plot of energy deposited measured by EC vs. track momentum  $p_{\text{thres}}^{\text{high}}$  for positive charged tracks. The red region depicts the cut that would reject events in the  $g7$  lepton EC PID scheme. Image source: [10]

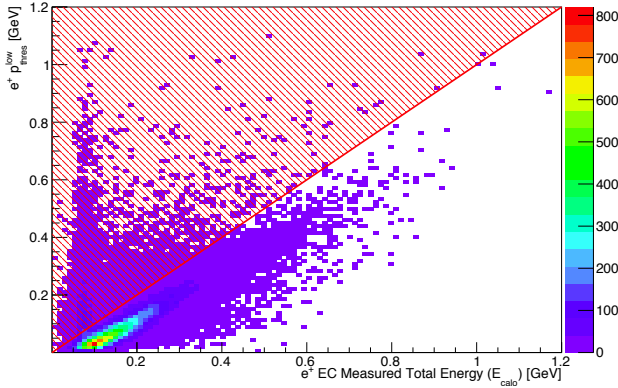


**Figure 88:** Plot of energy deposited measured by EC vs. track momentum  $p_{\text{thres}}^{\text{low}}$  for positrons from  $\pi^0$  events without the  $g7$  lepton EC PID scheme applied. The red region depicts the cut that would reject events in the  $g7$  lepton EC PID scheme. Image source: [10]

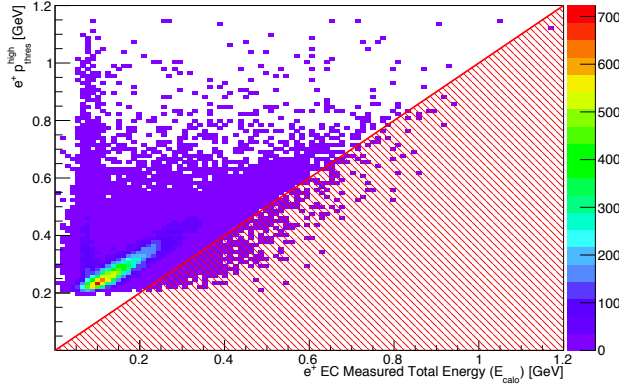


**Figure 89:** Plot of energy deposited measured by EC vs. track momentum  $p_{\text{thres}}^{\text{high}}$  for positrons from  $\pi^0$  events without the  $g7$  lepton EC PID scheme applied. The red region depicts the cut that would reject events in the  $g7$  lepton EC PID scheme. Image source: [10]

## 4 Flux Determination

The photon flux is based on the flux procedure outline in Ref. [23]. The script to generate the photon flux for g12 is here:

```
/home/clasg12/local/scripts/g12-gflux
```

and there is also a script (/home/clasg12/local/scripts/g12-gflux-all) that does not rebin the energies and outputs two columns: energy and flux for each logical paddle in the tagger.

The help output from the script:

```
> /home/clasg12/local/scripts/g12-gflux -h
usage: g12-gflux emin emax ebinwidth runlist.txt (good|all)
      (good|all) specifies either all scalar intervals
      or only "good" scalar intervals.
example:
      g12-gflux 1.5 5.5 0.2 runlist.txt good
where runlist.txt is an ascii file of one column: run
56363
56365
...

```

To use the script, you will need to create a file that consists of the run numbers you used in your analysis. Using this file name when you call g12-gflux, will give you the total flux as a function of beam energy in the range and binning requested. The command:

```
/home/clasg12/local/scripts/g12-gflux 1.5 5.5 0.2 filelist.txt good
```

will return to stdout the flux in the energy bins using three columns: emin, emax, flux. Something like this:

```

1.5 1.7 7.75466725993e+12
1.7 1.9 7.23861294572e+12
1.9 2.1 6.85242336788e+12
... [snip] ...
4.9 5.1 2.69244768955e+12
5.1 5.3 2.49808049501e+12
5.3 5.5 1.99322166816e+12

```

The option good or all can be used to specify if you only want to consider good regions, throwing out beam trips, or if you want all events from good scalar intervals as well as the beam trip regions.

An alternative script which does not rebin the data but returns the flux for each logical energy paddle can be run like this:

```
/home/clasg12/local/scripts/g12-gflux-all filelist.txt good
```

The script has been extensively tested on the 64-bit machines. The precision of all variables are adequate to provide at least 4 significant figures for the final flux numbers. The two scripts both poll the flux information from the output files of the program gflux which was run with the options:

```
gflux -c -b -B -ooutput.hbook -ttripfile.txt -F100000 -f0 -l1000 <infiles>
```

where <infiles> included all files, in order, for a specific run. The output files are kept on the /work directory on the CUE machines at JLab here:

```
/work/clas/clasg12/flux
```

and the associated trip files (see discussion below in Sec. 4.1) can be found here:

```
/work/clas/clasg12/clasg12/tripfiles
```

For reference, the output of gflux -h is here:

```
Usage: gflux [-Options] file1 [file2] etc...
```

#### Options:

- B Bloated mode(All histograms) equivalent to -P -T -e
- F[#] Run gated clock frequency in KHz, default 10 KHz
- M[#] Process only # number of events
- N[#] Normalize to this run, instead of using map
- P Rebuild PID with particle histograms
- R Do NOT rebuild TAGR bank, by default it does
- T Raw tagger histograms from TAGE, TAGT, and TAGI
- E apply tagger energy correction (default: no correction)
- b Batch mode(no printout on screen)
- c Clock based DAQ livetime, default event based
- e Make exclusive reaction histograms

```

-f          File number, necessary if you want to keep txt files
-l[#]       Scaler intervals in timeline histograms, default 50
-n          Process a normalization run
-o<outfile> Output hbook file name
-p          Particle histograms without rebuilding PID
-p          Particle histograms without rebuilding PID
-s          Start counter histograms from ST1 and STR
-t<file>   Trip file
-y<file>   Synch event mode (skip events)

```

The major caveat to using this script, which relies on gflux, is that you must included *whole runs* in your analysis for this to be accurate. This is because the gflux program was not designed to work with partial runs. So, you must verify that you have processed every file in the runs which were analyzed – one can use the g12runs program to aid in this.

## 4.1 Beam Trips

Beam trips were classified as scalar intervals with a lifetime above a threshold of 0.90. Depending on the trigger and run conditions, the peak of the lifetime ranged from 0.85 to 0.80. Additionally, due to the setup of the program in the flux procedure outline, Ref. [23], the beginning and the end of every file was labeled a bad scalar interval. With such a high number of files per run (100 to 200 files), roughly 12% of good data would be lost. To remedy this, we were able to load and run the flux calculator on a whole run basis and recover most of the events except for the first and last scalar of the run. As a result the flux is valid for whole runs only and a proper run list can be obtained from the g12-flux script.

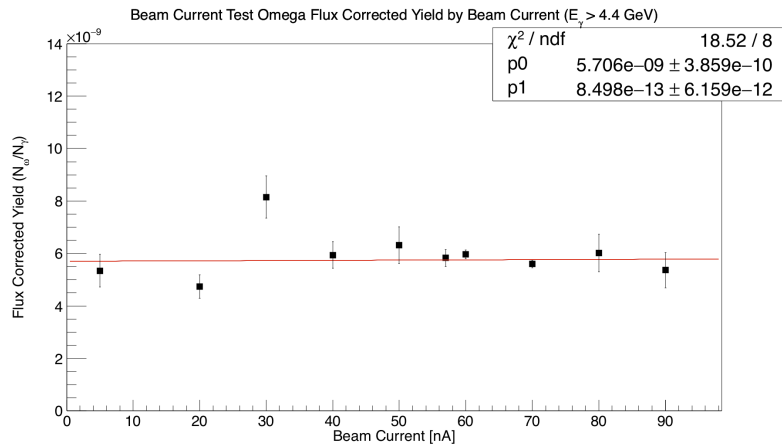
## 4.2 Normalized Yields for Different Beam Conditions

The  $\omega$  yield normalized to the flux as a function of beam current has also been studied in order to verify that there is no beam-current-dependent trigger or reconstruction inefficiency. This study is possible since g12 took data at various beam currents at the beginning of the running period. The variance photon multiplicity, i.e., having more than one photons in the chosen time bucket for the event, has also been taken into account. It can be seen, that the g12 normalized yields for the  $\omega$  do not have any statistically significant beam current dependency. The fitted slope shown in Fig.90 is consistent with zero.

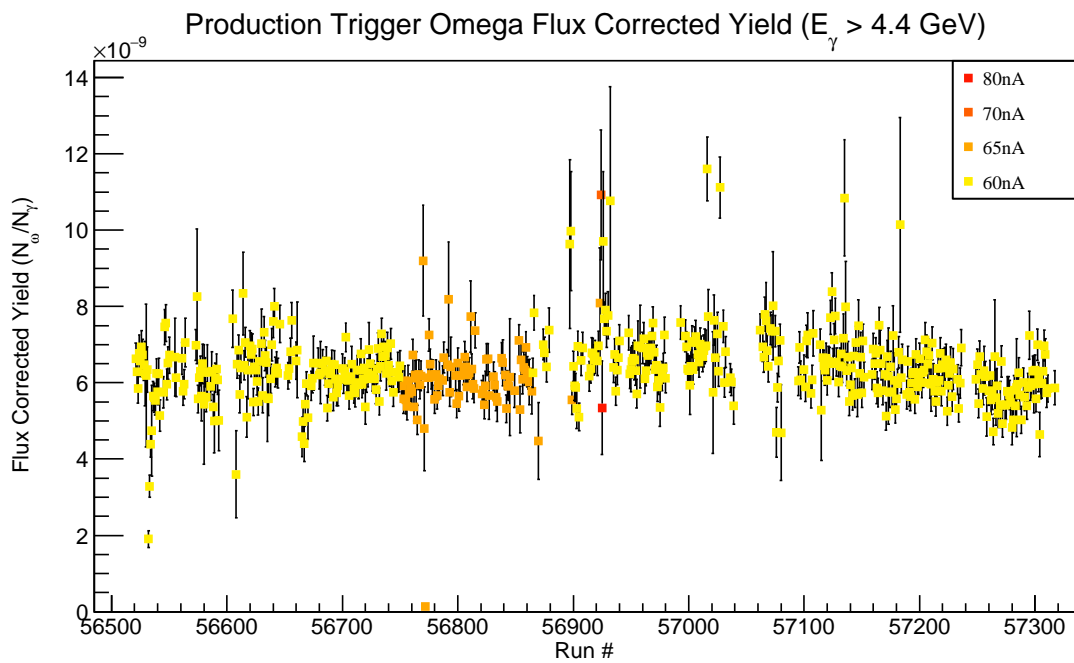
## 4.3 Run-by-run Stability and Systematic Uncertainty of Flux

Fig. 91 shows the stability of the flux corrections for runs after run 56519. These runs all use the same trigger and have a cut on  $E_\gamma > 4.4$  GeV. These data were projected onto the  $y$ -axis and fit to a Gaussian and the resulting error on the mean indicates a systematic uncertainty of 0.5%, though the width of the fit indicates a statistical uncertainty of approximately 10%.

The algorithm for summing the flux in each energy bin in g12-gflux is rather crude. It locks each energy bin to the center-point energy of the 767 tagger (logical) paddles. If finer control over the binning is required, one may use the g12-gflux-all program to return the flux in each individual logical energy bin of the tagger.



**Figure 90:** The flux-corrected yield of the  $\omega$  by beam current for high-energy part of the tagger ( $E_\gamma > 4.4 \text{ GeV}$ ).



**Figure 91:** Photon flux normalized yields by run for the production runs (Runs  $> 56519$ ).

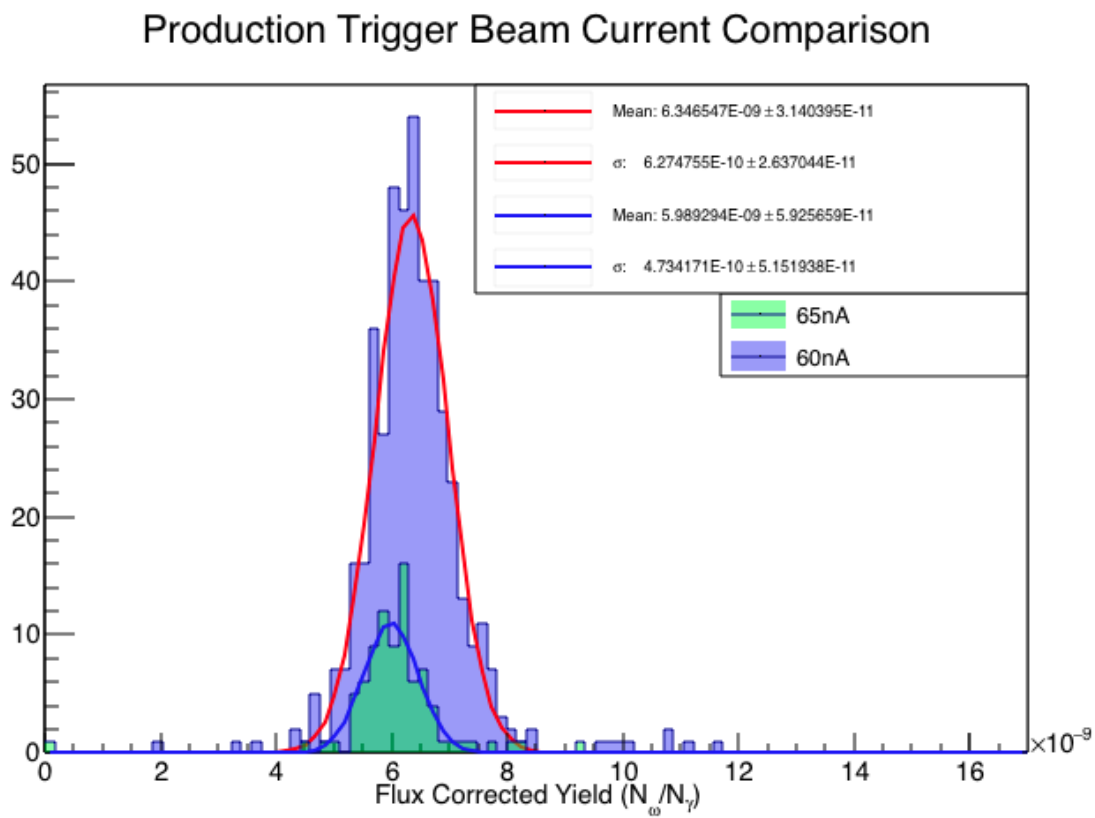


**Figure 92:** Gaussian fit to 60 and 65 nA data shown in Fig. 91. The error on the mean indicates a systematic uncertainty of 0.5%. The sigma of the Gaussian fit indicates a statistical uncertainty of approximately 10%.

There are two regions in the tagger that should be cut out of any analysis - in data, simulation and flux. The photon energy ranges affected are:

$$\begin{aligned} E_\gamma &\in [2.975, 3.175], \\ E_\gamma &\in [3.475, 3.575]. \end{aligned} \quad (19)$$

The first is due to a bad paddle readout (possibly a dead PMT), and the second is due to missing flux information. The width of the normalized yields distributions for given intensity in fact is consistent with the expected statistical widths. In Fig. 92, one can see that the widths are 6.2E-10 (60nA) and 4.7E-10(65nA). The expected statistical width (shown in Fig. 93) are actually 4.9E-10 (60nA, RMS: 2.6E-10) and 4.8E-10(65nA, RMS: 2.9E-10). These are consistent with each other and we should stick to the currently quoted lower bound of the systematic uncertainty for the g12 normalization of 5.7%.

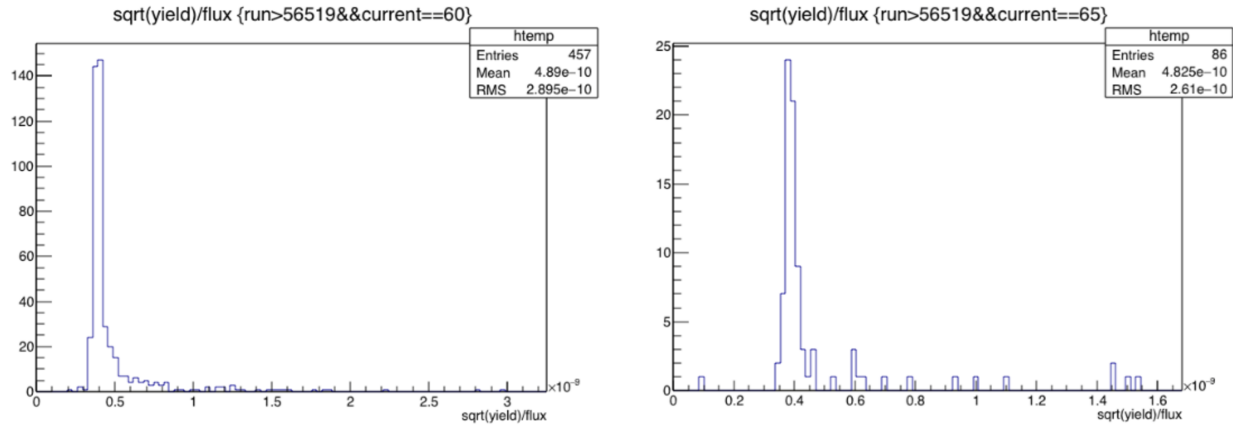


**Figure 93:** Expected statistical uncertainty for the flux normalized omega yields, for 60nA runs (left) and 65nA runs (right).

## 5 Simulations

All the programs in this section can be obtained from the standard *SVN* repository for *CLAS* here:

<https://jlabsvn.jlab.org/svnroot/clas/trunk>

Under this directory, you may find the following directories which hold the programs in the order which they appear below:

- simulation/generators/genr8
- io/part2gamp
- io/bosdump
- simulation/generators/ppgen
- simulation/gsim
- simulation/gpp

## 5.1 Generating Events for Digitization

One may use the program genr8 for generating t-channel phase space events. It is driven by an input key file which describes the exclusive reaction. Typical usage to generate 10k events from 4.4 to 5.45 GeV in beam energy using the input file “n\_pi-pipi+.input+” looks like this:

```
genr8 -M10000 -B4.4,5.45 -oevents.gamp < n_pi-pipi+.input
```

See the genr8 documentation for how to write the input file, or you can see this example here:

[http://clasweb.jlab.org/rungroups/g12/wiki/index.php/N\\_pimpippip](http://clasweb.jlab.org/rungroups/g12/wiki/index.php/N_pimpippip)

Gsim requires a bos file with a PART bank containing the MC event. Note PART bank 0 is reserved for MC events whereas PART banks 1 and 2 are used for containing the reconstructed event. The best way to convert GAMP to PART banks is by using gamp2part – the command, for protons pions and kaons, following the example above is:

```
gamp2part -r56855 -oevents.part -T -S-0.173,-0.0658,0.377,0.390 \
-z-110,-70 events.gamp
```

and for electrons and positrons

```
gamp2part -r10 -oevents.part -T -S-0.173,-0.0658,0.377,0.390 \
-z-110,-70 events.gamp
```

where the option -r10 is specific to RUN 10 in:

```
export CLAS_CALDB_RUNINDEX=calib_user.RunIndexg12_mk
```

This writes a BOS file full of PART, sector 0 banks with the 4-vector information from the gamp file. Also, the -z option smears the target distribution in Z, while the -S smears it in X and Y. The parameters are means and sigmas of a 2D Gaussian which were derived from a fit to the data. An alternative way to convert a gamp file to a BOS PART bank file is using gamp2txt and txt2part. These programs are piped together during run time.

```
gamp2txt -E5.714 -z-110,-70 < events.gamp | txt2part -T -oevents.part
```

The above command takes in gamp events, smears the z vertex in the target range, creates a tagger hit and writes out a bos file with HEAD, PART, and TAGR banks. Here is a bosdump of an event:

```
ifarml1> bosdump events.part -M1
Group: HEAD      Sector: 0          Nhits: 1    Next ind: 0
Version:        0
Run:           1
Event:         1
Type:          -2 (GSIM monte carlo)
ROC:           0
CLASS:         15
Trgbit:        0x1
```

TIME: Wed Feb 27 22:16:00 2008

```

Group: PART      Sector: 0      Nhits: 3  Next ind:      0
pid: 8
    vert-> x: 0.000  y: 0.000  z: -95.178
    p-> E: 3.194  px: -0.591  py: -0.688  pz: 2.942
    q: 1.000  trkid: 0  qpid: 0.000  qtrk: 0  flags: 0
pid: 9
    vert-> x: 0.000  y: 0.000  z: -95.178
    p-> E: 3.194  px: -0.591  py: -0.688  pz: 2.942
    q: -1.000  trkid: 0  qpid: 0.000  qtrk: 0  flags: 0
pid: 8
    vert-> x: 0.000  y: 0.000  z: -95.178
    p-> E: 4.780  px: -0.246  py: -0.140  pz: 4.383
    q: 1.000  trkid: 0  qpid: 0.000  qtrk: 0  flags: 0

Group: TAGR      Sector: 0      Nhits: 1  Next ind:      0
ERG:5.001 TTAG:0.000  TPHO:0.000 STAT:15 T_id:17  E_id:82

```

One can use any alternative to genr8 as long as the output is either gamp or an appropriate BOS file. For example, there is the phase-space generator ppgen:

```
ppgen -M<reaction code> -P<photon energy> -E5.714 -j1 -G -A \
-t<t-slope> -m50000 > events.gamp
```

The output can be txt or gamp file depending on user's needs. Follow the previous instructions to convert to part banks as needed.

## 5.2 Digitization and Smearing

The program to track the particles through the simulation and ultimately digitize the information to simulated “raw” banks is the geant3-based program: gsim. Running this on the BOS file created above looks like this:

```
gsim_bat -ffread ffread.g12 -kine 1 -mcin events.part \
-bosout events.gsim -trig 2000000
```

Using the above command, should create a gsim BOS output file. Here is the FFREAD file should be used to run gsim\_bat for *g12* analyses not using electrons/positrons:

```
====BEGIN=====FFREAD.G12=====
CUTS 5.e-3 5.e-3 5.e-3 5.e-3 5.e-3
DCCUTS 1.e-4 1.e-4 1.e-4 1.e-4 1.e-4
ECCUTS 1.e-4 1.e-4 1.e-4 1.e-4 1.e-4
SCCUTS 1.e-4 1.e-4 1.e-4 1.e-4 1.e-4
```

MAGTYPE 2

```

MAGSCALE 0.500 0.000
PTGIFIELD 0
STTYPE 1
STZOFF -90.0
TGPOS 0. 0. 0.
TARGET 'g11a'
TGMATE 'PROT'
POSBEAM 0.0 0.0

GEOM 'ALL' 'ST'
NOGEOM 'MINI' 'PTG '
BEAM 5.714
DCAY 1
KINE 1
MULS 1
AUTO 1

RUNG 56855
TIME 1000000 1000000 1000000
TRIG 1000000
STOP
====END=====FFREAD.G12=====

```

and for electrons/positrons the FFREAD file should read

```

=====FFREAD.G12=====
CUTS 5.e-3 5.e-3 5.e-3 5.e-3 5.e-3
CCCUTS 1.e-3 1.e-3 1.e-3 1.e-3 1.e-3
DCCUTS 1.e-4 1.e-4 1.e-4 1.e-4 1.e-4
ECCUTS 1.e-4 1.e-4 1.e-4 1.e-4 1.e-4
SCCUTS 1.e-4 1.e-4 1.e-4 1.e-4 1.e-4

```

```

UPSTPOS 0. 0. 0.
MAGTYPE 2
MAGSCALE 0.500 0.000
PTGIFIELD 0
STTYPE 1
STZOFF -90.0
TGPOS 0. 0. 0.
TARGET 'g11a'
TGMATE 'PROT'
POSBEAM 0.0 0.0
GEOM 'ALL' 'ST'
NOGEOM 'MINI' 'PTG'
BEAM 5.714
DCAY 1

```

```

PAIR 1
HADR 1
MULS 1
KINE 1
AUTO 1
RUNG 10
TRIG 200000
STOP
=====

```

The tracking and digitization done by `gsim` is ideal and there is no smearing done. To get the simulated data to mimic the detector resolution the “`gsim` post-processor” (`gpp`) is used. For `g12`, and following the above example, one should use this command for protons, pions and kaons:

```
gpp -Y -s -S -a2.73 -b1.7 -c1.93 -f1 -R56855 -P0x7f -oevents.gpp events.gsim
```

and for electrons and positrons

```
gpp -Y -s -S -a2.73 -b1.7 -c1.93 -f1 -R10 -P0x7f -oevents.gpp events.gsim
```

The values passed to the `gpp` command line options, `-a`, `-b`, `-c`, helps match the tracking resolution of the simulated data to that of the real events in the regions 1,2 and 3 of the CLAS Drift Chambers. They accomplish this by smearing the DOCA values and hence `gpp` is able to match the DC residuals for the simulated CLAS tracks to that of the real CLAS tracks on a region-by-region basis. The `gpp` option `-f` smears the Time-of-Flight tdc values and during analysis the default `gpp` smearing for TOF was found to be adequate. The smearing should be run with a good `g12` run number; run 56855 has all the necessary constants in the database to get the tagger timing smearing done correctly. Also, interested parties can add accidentals to the TAGR bank by using the `-A` option like so:

```
gpp -Y -s -S -a2.73 -b1.7 -c1.93 -f1 -R56855 -P0x7f -oevents.gpp \
-A/path/to/output/from/filter_tagr events.gsim
```

The program `filter_tagr` scans through real data files and outputs a `bos` file containing only the TAGR banks. These files are then supplied to `gpp` with the `-A` option, and `gpp` puts the contents of these banks as accidentals in the MC TAGR bank. Output from `filter_tagr` for run 56855 can be found at:

```
/home/clasg12/local/etc/clas6/gpp_tagger_profile.bos
```

As stated earlier, the goal of using GPP is to simulate the experimental conditions as close as possible. So we smear the values of the DOCA for the simulated tracks with a single Gaussian whose width is equal to the events weighted sum of the widths of the two Gaussians fitted to the data from the run 56855. This makes the residual for a superlayer in the simulated data approximately equal to the weighted residual from the real data. The default available options for GPP specifies only three parameters ‘`-a`, `-b`, `-c`’ for DC DOCA smearing, where each parameter is responsible for the smearing of two superlayers (in one Region) of all six sectors. Hence, we choose a set of parameters based on the following fits as seen in Figs. 94 and 95, which gives us the best match on average between the different superlayers in the six sectors (see Fig. 96).

The smearing parameter ‘`-f`’ for the Time of Flight timing resolution is one of the GPP parameters that is usually used to match the quality of data and simulation. Using the reference run 56855, we observe that the default GPP smearing is adequate (see Figure 97).

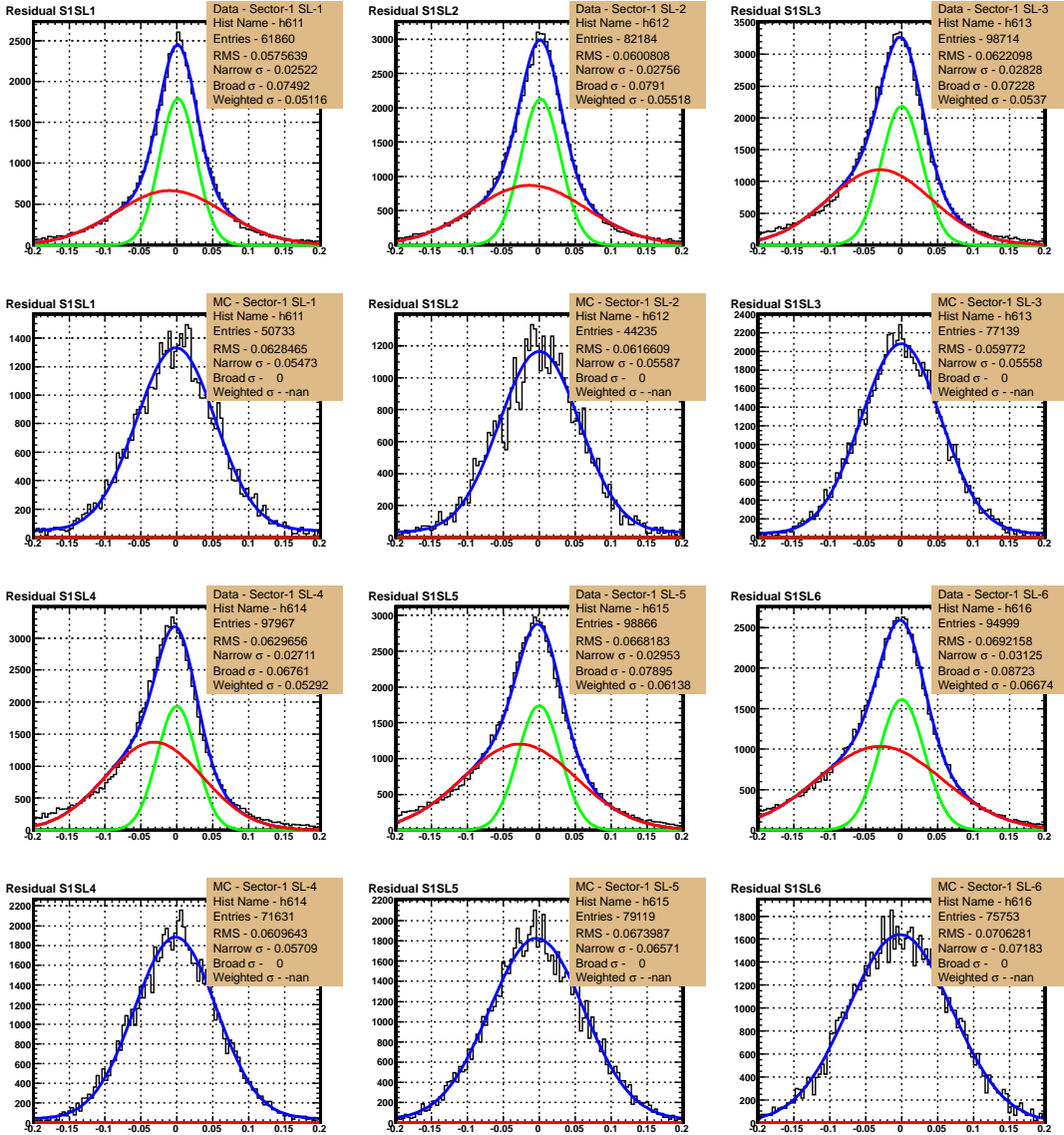


**Figure 94:** Plots and Fits used to match the residuals (resolution) for Drift Chamber superlayers in CLAS Sector 1, between the Data and the Simulation. Data is an empirical fit to a convolution of two gaussians. The simulated distribution is a single gaussian with its simulated width approximately equal to the weighed sum of the widths of the two gaussians fitted to the data. This simulation uses the best estimated smearing parameters to match the DC residuals, between the Data and the Simulation.

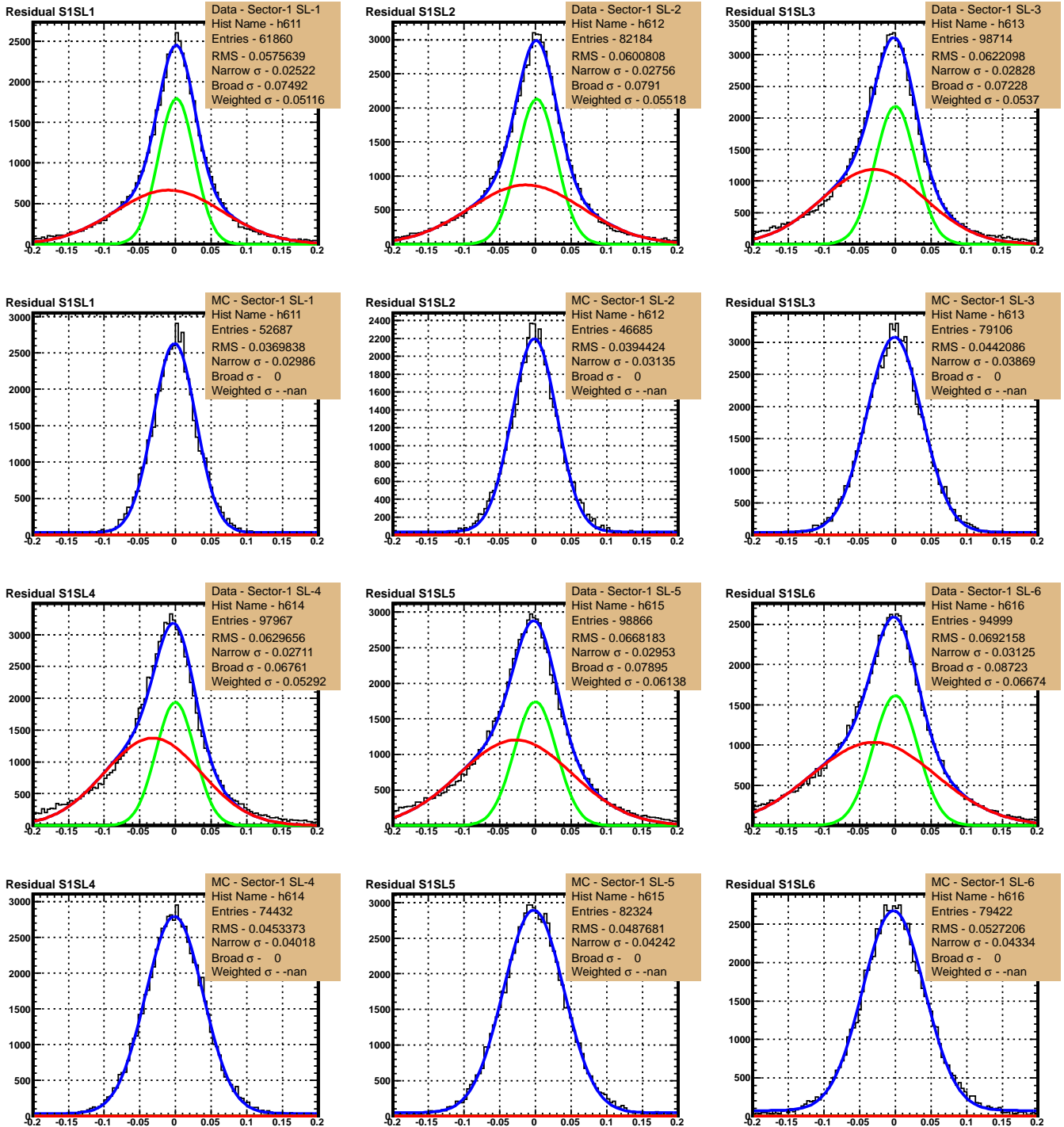


**Figure 95:** Plots and Fits used to compare the residuals (resolution) for Drift Chamber superlayers in CLAS Sector 1, between the Data and the Simulation using the default GPP smearing.

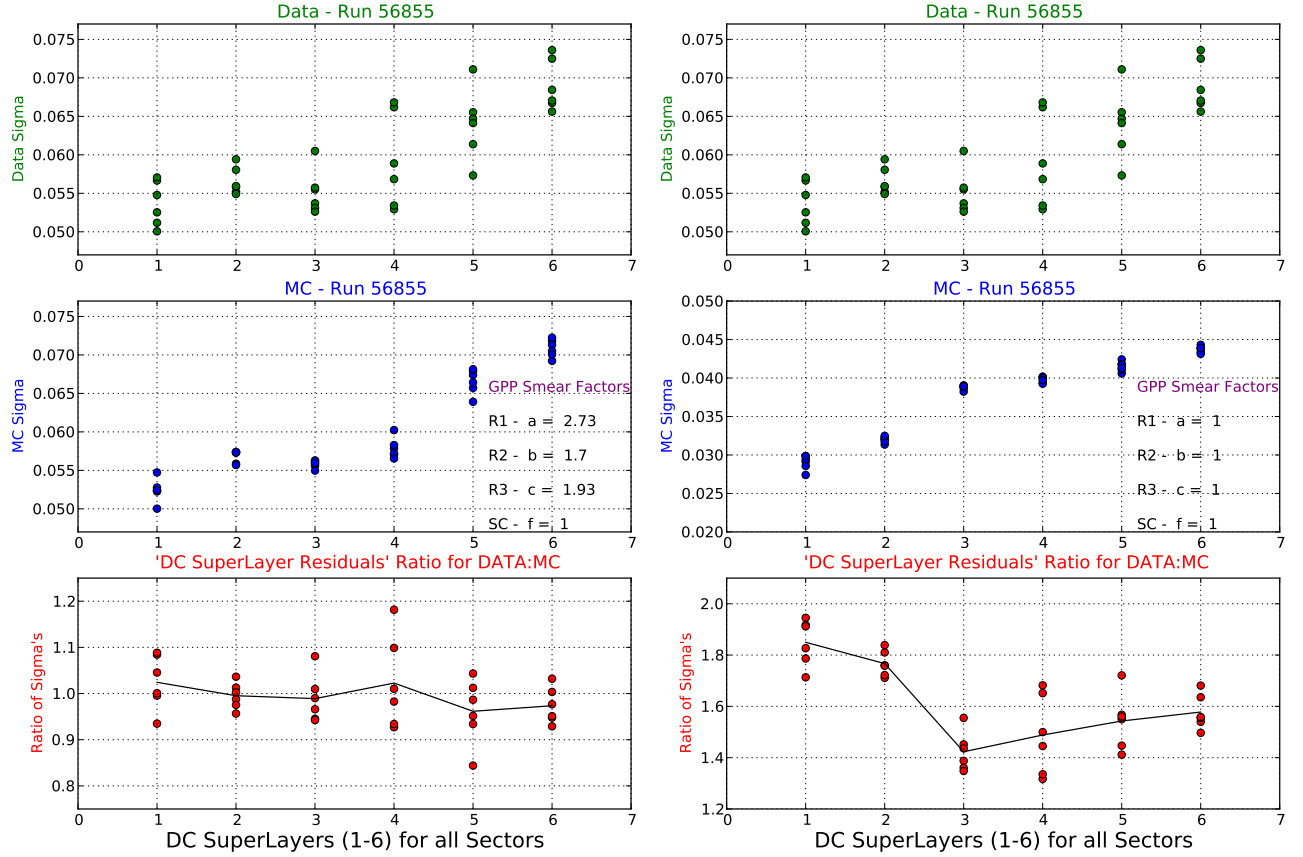


**Figure 96:** Comparison of the DC residuals on a superlayer basis for all the CLAS sectors for real as well as simulated events. The left plots use the best estimated smearing parameters for the DC DOCA to match the real and simulated data shown in Figure 94., whereas the right plots use the default GPP smearing shown in Figure 95.

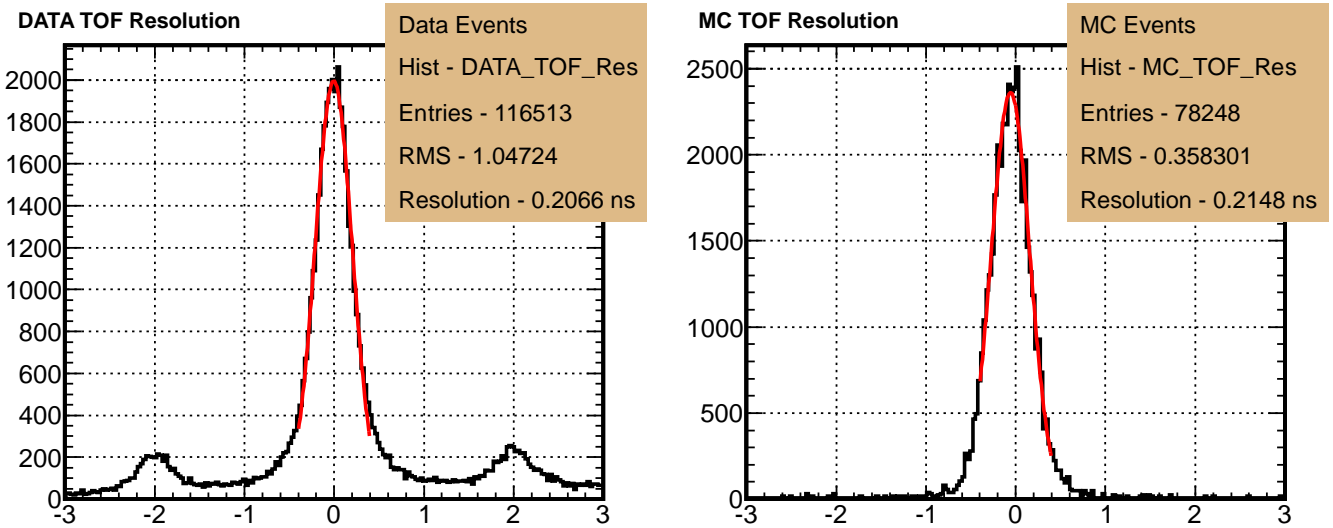


**Figure 97:** Plots and Fits used to match the TOF timing resolution. The default smearing of GPP was found to be adequate in this case.

**Table 26:** Measure of Track Reconstruction Efficiency for sets of gpp parameters

Events Generated	Events Accepted	Reconstruction Acceptance	gpp Smearing Factors
-a	-b	-c	-f
90000	1217	1.352%	1 1 1 1
90000	1161	1.29%	2.73 1.7 1.93 1
90000	1053	1.17%	2.73 1.7 1.93 2

These smearing parameters affect the reconstruction efficiency for the tracks in CLAS during simulations. A rudimentary analysis quantifying the effect is presented in Table 26. As expected, as the Drift chamber response becomes more noisy due to smearing of DOCA (higher DC residuals), the reconstruction and tracking efficiency in CLAS goes down.

### 5.3 Fiducial Region Selection

We derived *Geometric fiducial cuts* for the g12 data, which are cuts based on the exclusion of events laying outside regions where acceptance is well behaved and reliably reproduced in simulation. Such regions for all g12 data are expressed as an upper and lower limit of the difference in azimuthal angle between the center of a given sector, and a particle track. Because of the hyperbolic geometry of CLAS and the presence of the toroidal magnetic field, the fiducial boundaries on the angle  $\phi$  are functions of momentum ( $p$ ), charge, and polar angle ( $\theta$ ) of each track. The boundaries were evaluated separately in each sector, nominally defined as the  $\phi$  values in which occupancy drops below 50% of that in the respective sector's flat region. The flat regions were defined as  $-10^\circ < \phi < 10^\circ$ . The nominal upper and lower  $\phi$  limits depend strongly on particle charge,  $p$  and  $\theta$ , hence the need for functional characterization and extrapolation.

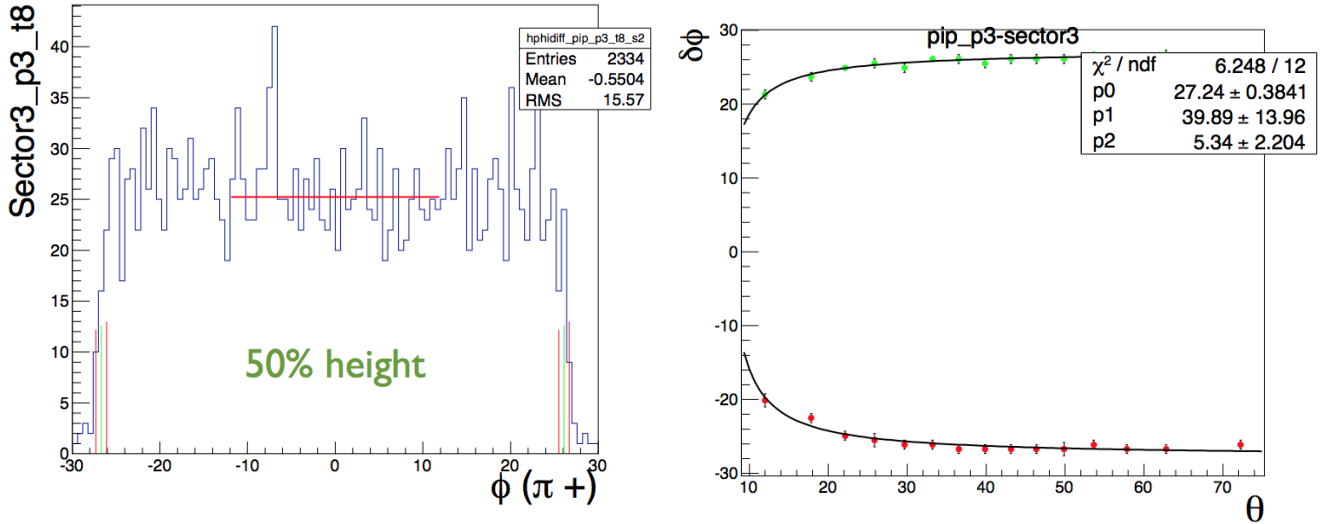


**Figure 98:** Left: shows the  $\pi^+$   $\phi$  distribution for sector-three in one  $p$  and  $\theta$  bin along with the upper and lower limits of the fiducial region represented by the green vertical line. Right: a second-generation plot, fit to a hyperbola.

In order to determine the fiducial limits for charged hadrons, a sample of exclusive  $\gamma p \rightarrow p \pi^+ \pi^-$  events were sliced into  $5 \times 15 \times 6$  bins in  $p$ ,  $\theta$ , and sector respectively. The  $\phi$  distributions for  $\pi^+$  and  $\pi^-$  were plotted separately in each bin. The upper and lower  $\phi$  limits of these *first-generation* plots were found according to the nominal fiducial definition of 50% occupancy as illustrated in Fig. 98. The results from the first-generation fits were represented in *second-generation* plots of  $\phi_{min}$  and  $\phi_{max}$  vs  $\theta$  as also shown in Fig. 98. The data in the second-generation plots were fit with hyperbolas, chosen since they replicate the projection of the detector. Second-generation fitting parameters were then plotted vs  $p$  in *third-generation* plots. These third generation plots were fit to power functions as shown in Fig. 99. Results of the third-generation fits define the sought after functional form  $\phi_{min}(\theta, p)$  and  $\phi_{max}(\theta, p)$  for each sector. The sector integrated results for positive and negative hadron tracks compose the nominal fiducial region. *Tight cuts* and *loose cuts* were defined as a contraction and expansion respectively, by  $4^\circ$  from the nominal fiducial cuts. Figs. 100-103 show the effects of the cuts.

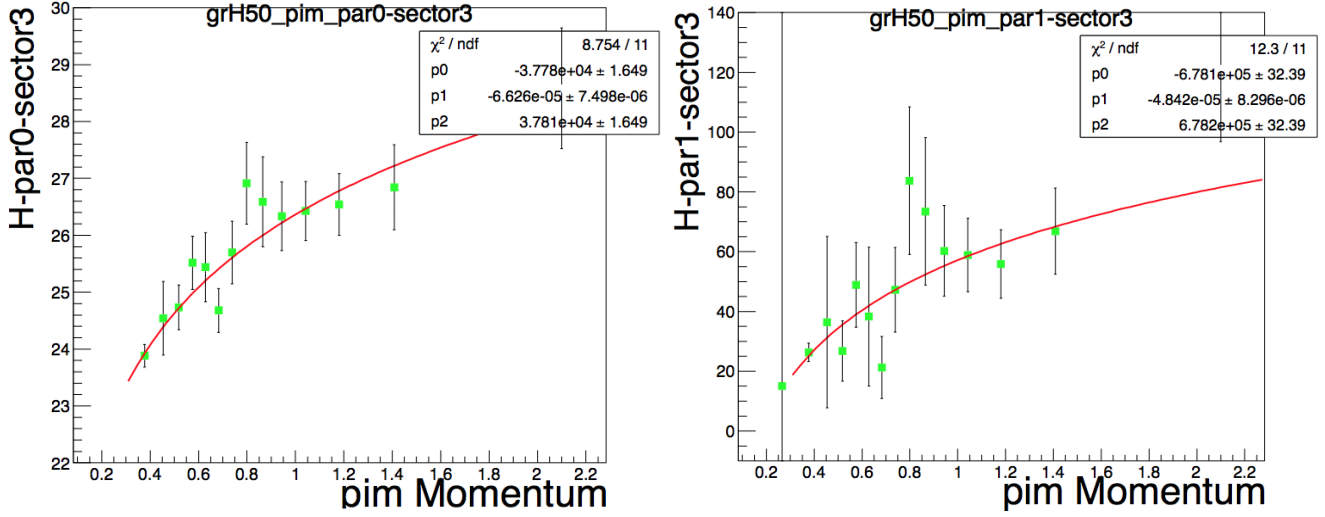


**Figure 99:** Third-generation plots of the fitting parameters from second-generation fits for sector three. The data are fit to power functions.

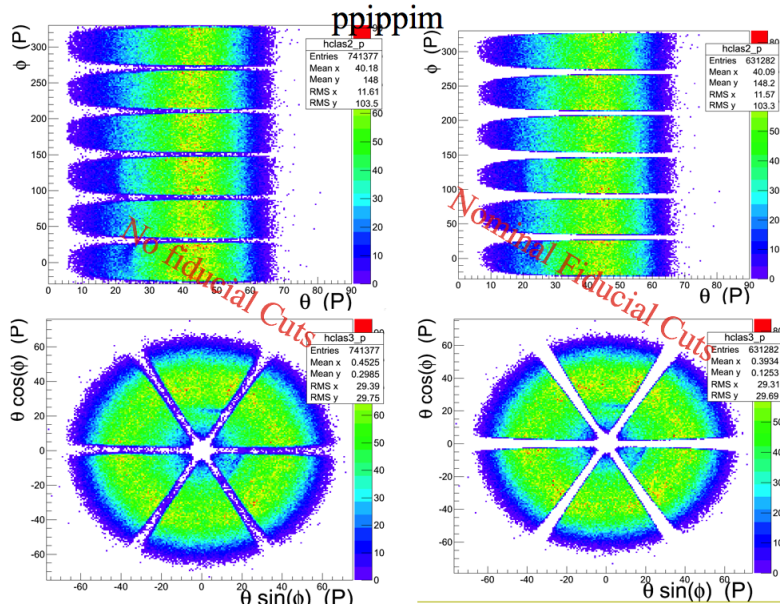


**Figure 100:** The angular distribution of the proton from exclusive  $p\pi^+\pi^-$  events is shown. In the top,  $\phi$  vs  $\theta$  is plotted, the bottom plots conveys similar information mapped to mimic the geometry of CLAS. Left: No fiducial cuts. Right: nominal fiducial cuts on the proton.

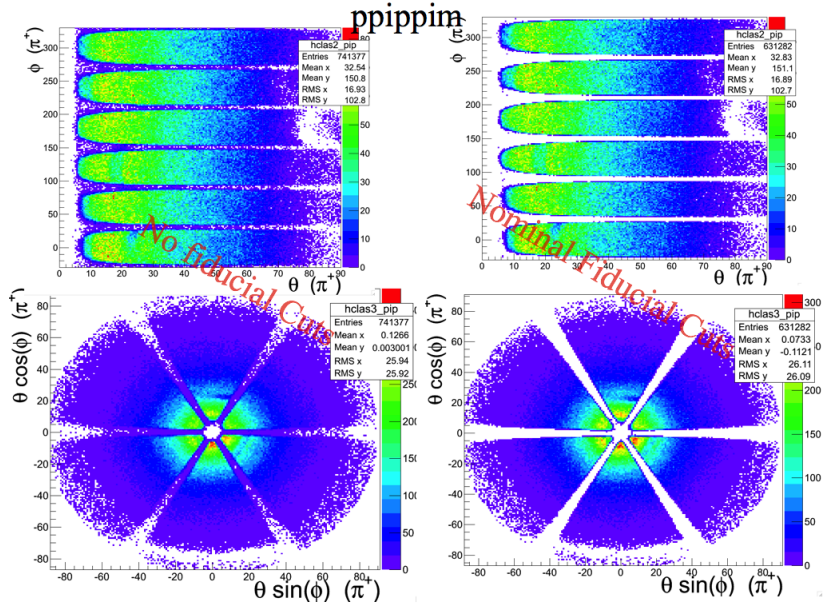


**Figure 101:** The angular distribution of the positive pion from exclusive  $p\pi^+\pi^-$  events is shown. In the top,  $\phi$  vs  $\theta$  is plotted, the bottom plots conveys similar information mapped to reflect the geometry of CLAS. Left: no fiducial cuts. Right: nominal fiducial cuts on the positive pion.

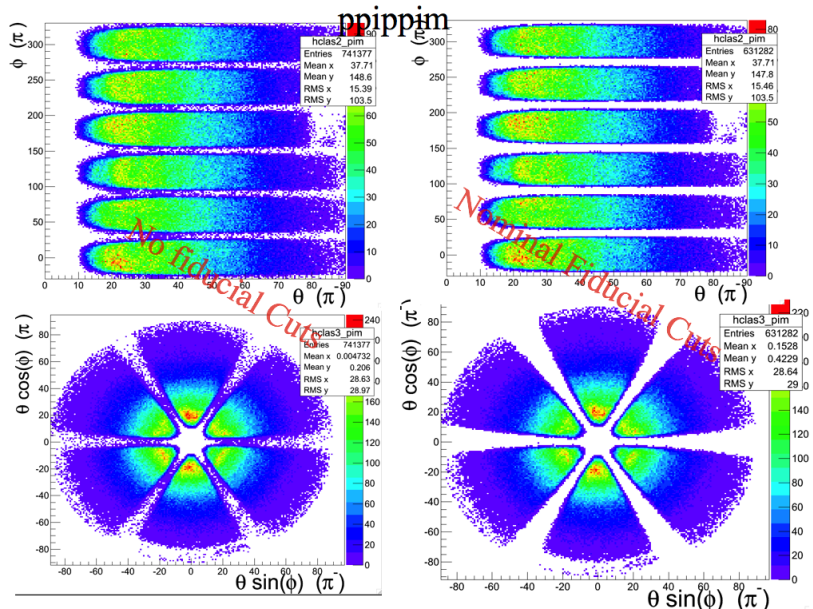


**Figure 102:** The angular distribution of the negative pion from exclusive  $p\pi^+\pi^-$  events is shown. In the top,  $\phi$  vs  $\theta$  is plotted, the bottom plots conveys similar information mapped to reflect the geometry of CLAS. Left: no fiducial cuts. Right: nominal fiducial cuts on the negative pion.

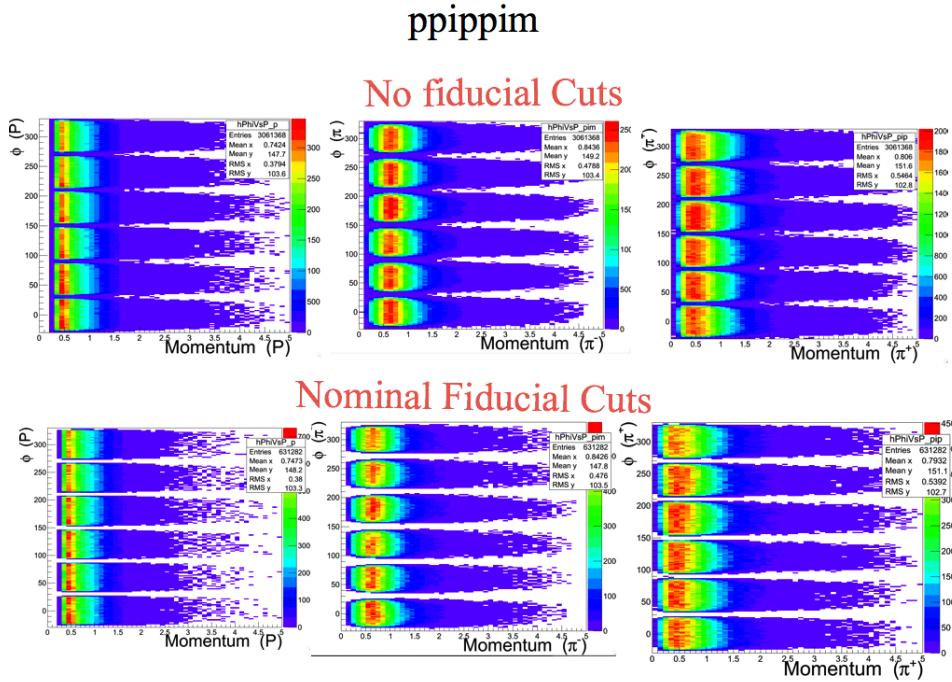


**Figure 103:** From left to right:  $\phi$  vs momentum for the proton, negative pion and positive pion for  $p\pi^+\pi^-$  events. Top: no fiducial cuts. Bottom: nominal fiducial cuts.

To perform fiducial cuts for the G12 data use the header files:

```
https://jlabsvn.jlab.org/svnroot/clas/users/mkunkel/clas \
/g12_corrections/g12_NegParticle_fiducial_cuts.hpp
```

and

```
https://jlabsvn.jlab.org/svnroot/clas/users/mkunkel/clas \
/g12_corrections/g12_PosParticle_fiducial_cuts.hpp
```

The user needs the particle momentum, polar angle  $\theta$ , and azimuthal angle  $\phi$ . To use:

```
clas::g12:: \
g12_PosParticle_fiducial_cuts(particle_P, particle_Theta, particle_Phi,"nominal") \
clas::g12:: \
g12_NegParticle_fiducial_cuts(particle_P, particle_Theta, particle_Phi,"nominal")
```

There are 3 types of options for the keyword depending on the desired cut, "nominal", "tight", and "loose". The header will return false if particle was not within fiducial region, true if particle was within fiducial region.

## 5.4 Reconstruction of Simulated Data

The reconstruction of simulated data requires a slightly different tracking function and is taken care of by adding the option -X0 to the reconstruction program. For protons, pions and kaons:

```
a1c -T4 -ct1930 -cm0 -cp0 -X0 -d1 -F -P0x1bff -z0,0,-90 \
-Aprlink_tg-90pm30.bos -oevents.a1c events.gpp
```

and for electrons and positrons:

```
a1c -R10 -T4 -ct1930 -cm0 -cp0 -X0 -d1 -F -P0x1bff -z0,0,-90 \
-Aprlink_tg-90pm30.bos -oevents.a1c events.gpp
```

The help output of a1c says this about the `-X#` option:

```
[-X#]      use a different x vs. t function in tracking (def = 2, MC = 0)
```

## 5.5 Simulating the Lepton Trigger

During the collection process, for an event to be written by the DAQ it must have passed at least one of the trigger “bits” defined in Sec. 1.1. The process of lepton triggering required a coincidence between the EC and the CC subsystems. This coincidence was established by using the voltage sum of the CC for a sector and the voltage sum of the EC for the same sector and comparing each sum to a preset threshold described in Table 6. However when GSIM simulates tracks through the CC and EC, it does not account for the minimum voltage threshold that was required for data collection, moreover the simulation of the trigger must match the trigger efficiency seen for a selected reaction, i.e. the lepton trigger efficiency for  $\pi^0$  candidates discussed in [10].

Simulation of the CC and EC trigger “bit 6”, Table 3, was performed by writing an algorithm that attempted to mimic the method in which triggered data was recorded. To accomplish this a modified function, written by Simeon McAleer from FSU, was written into the simulation reconstruction algorithm. The routine returned the sector and a boolean of 0 or 1 (pass or fail), that simulated the trigger based on the following criteria;

1. The sector with the highest EC summed energy over threshold.
2. The sector with the highest EC Inner Layer summed energy over threshold.
3. The sector with the highest CC summed energy over threshold.
4. All three above conditions must be in same sector.

Thresholds as described in Table 6 are 80 mV, 60 mV and 20 mV for EC *inner*, EC*total* and CC respectively. The CC trigger threshold was applied to groups of eight CC PMTs, called “sim bits”. The “sim bits” were staggered by four PMTs so that each PMT goes into two “sim bits”, after which all “sim bits” were “OR”’d together. If any “sim bit” calculated as above threshold, that specific sector was then compared to the remaining sectors to establish the condition listed in 3.

The EC *inner* and EC *total* trigger thresholds were applied to all EC strips in a sector. This was done by summing over the energy for every strip in every orientation of the EC per sector. If the energy summation for the EC *inner* was above threshold, that specific sector was then compared to the remaining sectors to establish the condition listed in 2. If the energy summation for the EC *total* was above threshold, that specific sector was then compared to the remaining sectors to establish the condition of the sector with the highest EC summed energy over threshold.

### 5.5.1 Validity of Trigger Simulation

The actual triggered data could have been triggered by the following scenarios;

1.  $e^-$  CC and EC hit above preset thresholds,
2.  $e^+$  CC and EC hit above preset thresholds,
3.  $e^-$  CC hit above preset thresholds and  $e^+$  EC hit above preset thresholds in the same sector,
4.  $e^-$  EC hit above preset thresholds and  $e^+$  CC hit above preset thresholds in the same sector.

The lepton trigger “bit 6” was 100% efficient, for  $\pi^0$  candidates (see [10] Sec. *Lepton Trigger Efficiency for  $\pi^0$  Candidates*), when the data was cut using all the conditions listed above (1, 2, 3, 4) using an “OR” flag. This means that a  $\gamma p \rightarrow pe^+e^-$  event must satisfy at least one of the listed conditions. The reduction in events when at least one of the conditions was satisfied was 69.91%. Prior to simulating the trigger, cutting the MC with the listed conditions reduced the event yield by 81.91%. Simulating the trigger and cutting on the MC events with the listed conditions reduced that event yield to 69.48%. This indicates that the trigger simulation is properly mimicking the trigger configuration used when data is collected.

## 6 Comparison of Data to Known States and Cross Sections

In this section we show a series of figures depicting known resonances with the g12 data. The reader is encouraged to compare the masses and widths measured with the PDG[20]. The masses of the narrow states in g12 are all measured to be consistent with the known values, such as  $\eta$  in Fig. 104 using the missing mass technique,  $\pi^0$  reconstructed using two photons Fig. 105,  $\rho/\omega$  reconstructed using two leptons Fig. 106, as well as  $\Xi^-$  from the reaction of  $\gamma \pi \rightarrow K^+ K^- (X)$  shown in Fig. 107. Fig. 108 shows the invariant mass of the  $K^*$  from  $K^+ [\pi^0]$ . In addition to these missing masses, we have already shown a good  $K_s$  signal from  $\pi^+ \pi^-$  in Fig. 62 on page 71. The  $K^{*+}$ , shown in Fig. 108, and the  $\phi(1020)$  shown in Fig. 109, are also spot on when compared with the PDG values.

### 6.1 Track dependent inefficiency correction

If the efficiencies of the detectors and the triggers have been measured and modeled perfectly, then it’s reasonable to expect that the reconstruction efficiency can be faithfully reproduced in simulation on a track-by-track basis. For the charged particles, this has been investigated thoroughly using the reaction  $\gamma p \rightarrow p\pi^+\pi^-$  events, using the following 3 topologies:

$$\begin{aligned} \gamma p &\rightarrow p\pi^+(\pi^-) \\ \gamma p &\rightarrow p\pi^-(\pi^+) \\ \gamma p &\rightarrow \pi^+\pi^-(p) \end{aligned} \tag{20}$$

The efficiency map was derived for each particle, as a function of momentum, angles ( $\theta, \phi$ ) in the lab frames, as well as the vertex positions, in the same manner for  $p, \pi^+, \pi^-$ . The results of pions can be applied to kaons for analyses involving detected kaons. For example, for  $\pi^+$ , the reconstruction efficiency can be derived using the  $\gamma p \rightarrow p\pi^-(\pi^+)$ . If  $\pi^+$  can be reconstructed using the missing mass techniques and

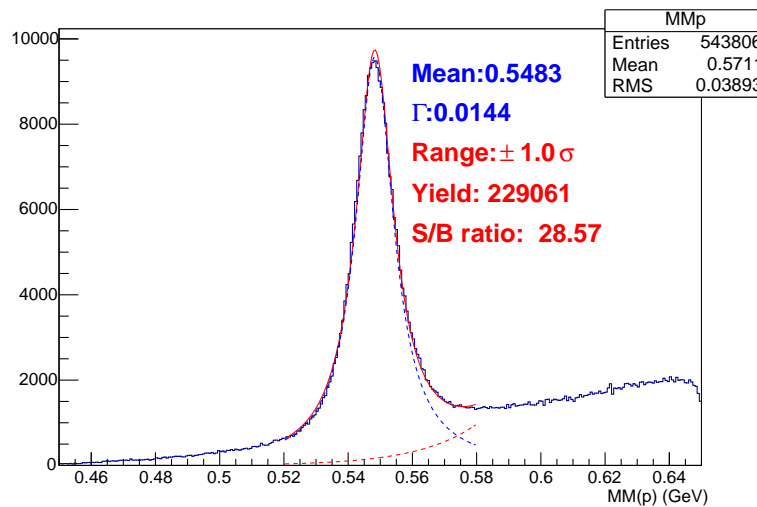


**Figure 104:** Missing mass off proton showing the  $\eta$  resonance with a measured mass of 548 MeV.

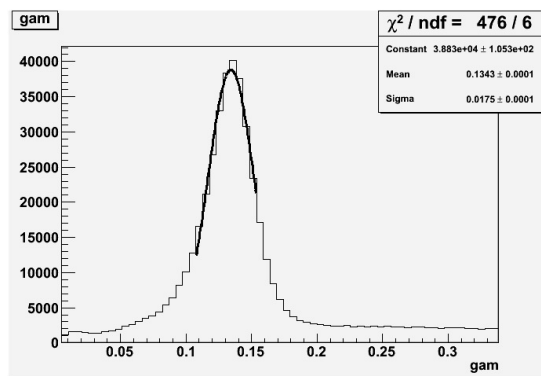


**Figure 105:** Invariant mass of two final-state photons showing the  $\pi^0$  meson.

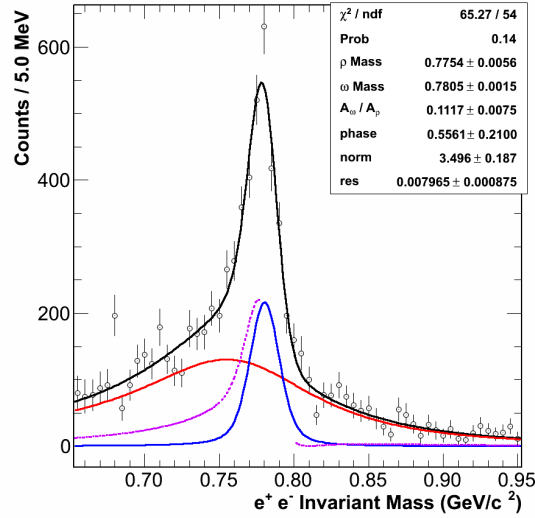


**Figure 106:** Invariant mass of electron and positron pair showing the (mixed)  $\rho$  and  $\omega$  mesons.

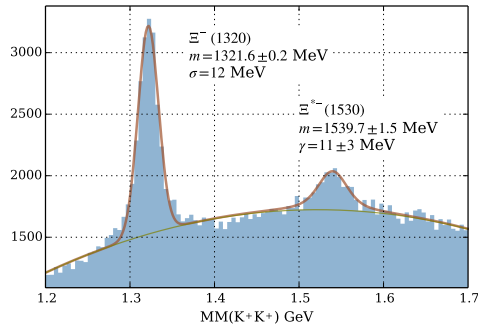


**Figure 107:** Missing mass off  $K^+K^+$  showing the ground state and first-excited  $\Xi^-$  resonances. The ground state is fit to a Gaussian with a width shown as  $\sigma$ , while the first excited state is fit to a Voigtian with a (scaled) Gaussian width taken from the ground state. The value  $\gamma$  shown is the Lorentzian width of the fit.

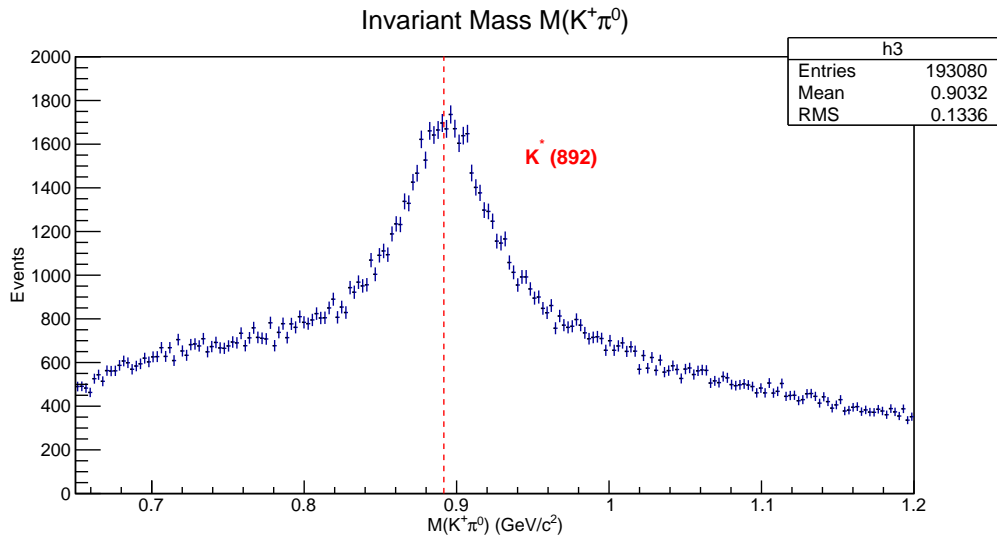


**Figure 108:**  $K^+ [\pi^0]$  invariant mass spectrum in the reaction  $\gamma p \rightarrow K^+ \Lambda(\pi^0)$ , where  $\pi^0$  was constrained to the PDG mass. The line indicates the PDG value of  $K^{*+}$  mass.  $\Lambda \rightarrow p\pi^-$  events are selected.

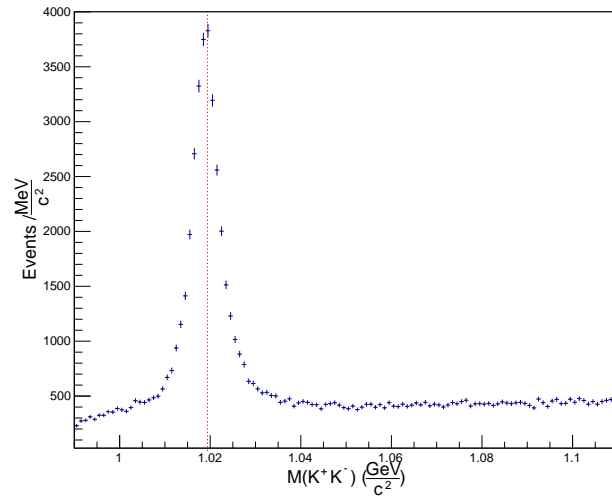


**Figure 109:**  $K^+K^-$  invariant mass spectrum in the reaction  $\gamma p \rightarrow K^+K^- p$ , where all particles are detected by CLAS. The line indicates the PDG value of  $\phi(1020)$  mass.

also pass the kinematic fitting probability cut  $> 1\%$ , then the data was checked to see if the  $\pi^+$  was actually detected. This was done exactly the same way in both simulation and real data. In a perfect world, the ratio of the two efficiency map (Simulation devided by the real data) should be exactly 1 everywhere. However, as can be seen in Fig. 110, the ratio is usually larger than 1, indicating the simulation has an over efficiency on the order of 5%. Similar over efficiency can also be seen for the  $\pi^-$  and the proton, as shown in Fig. 111 and 112. For a final state that requires three charged tracks, this will lead to an correction that is on average about 18% globally. This correction accidentally is very similar to the g11 global normalization correction factor. However, the g12 correction is a function of momentum, angles and vertex positions, and is applied dynamically on a event-by-event basis. The standard g12 procedure for applying the above corrections can be applied using the routines found in the jlab SVN repository (<https://jlabsvn.jlab.org/svnroot>) here:

```
clas/users/mkunkel/clas/g12_corrections/g12_trackEfficiency.hpp
```

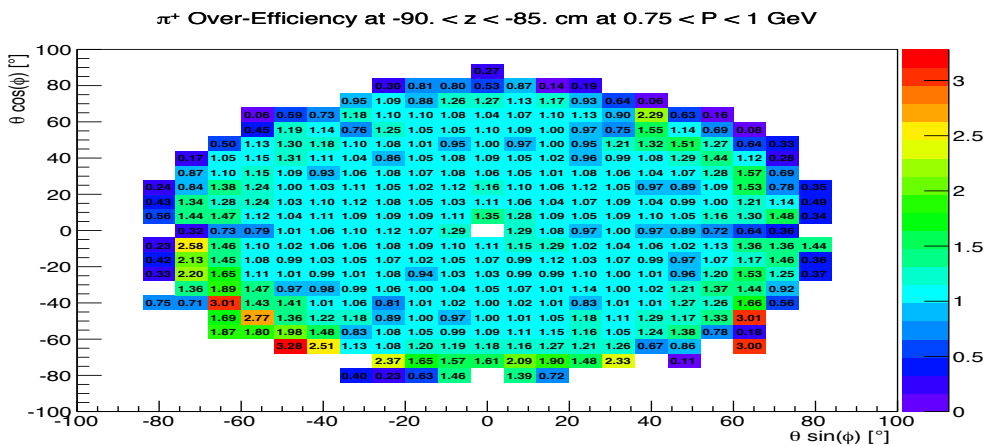


**Figure 110:**  $\theta \cos \phi$  vs.  $\theta \sin \phi$  plot showing the over-efficiency of simulating the  $\pi^+$  with z-vertex  $z \in [-90, -85]$  cm and momentum  $p \in [0.75, 1]$  GeV from a 2 charged track reaction.

Further details about this procedure can be found in Reference [10]. It is important to point out that this track-dependent efficiency correction is also tied to the multiple photon correction, and can be derived by either accounting for events lost to multiple photons, or using all photons in the chosen time bucket. The difference between these two methods can be used to estimate the systematic uncertainty of this correction. For a three-charged tracks topology, the uncertainty is estimated to be around 3%.

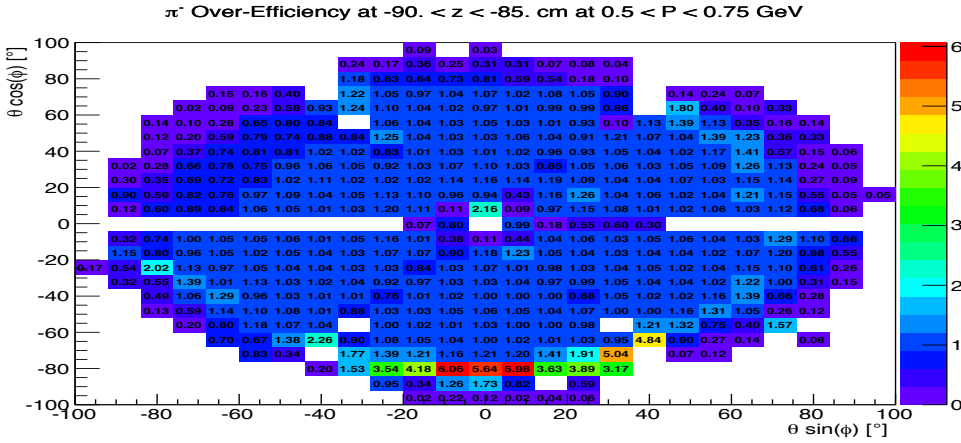


**Figure 111:**  $\theta \cos \phi$  vs.  $\theta \sin \phi$  plot showing the over-efficiency of simulating the  $\pi^-$  with z-vertex  $z \in [-90, -85]$  cm and momentum  $p \in [0.75, 1]$  GeV from a 2 charged track reaction.

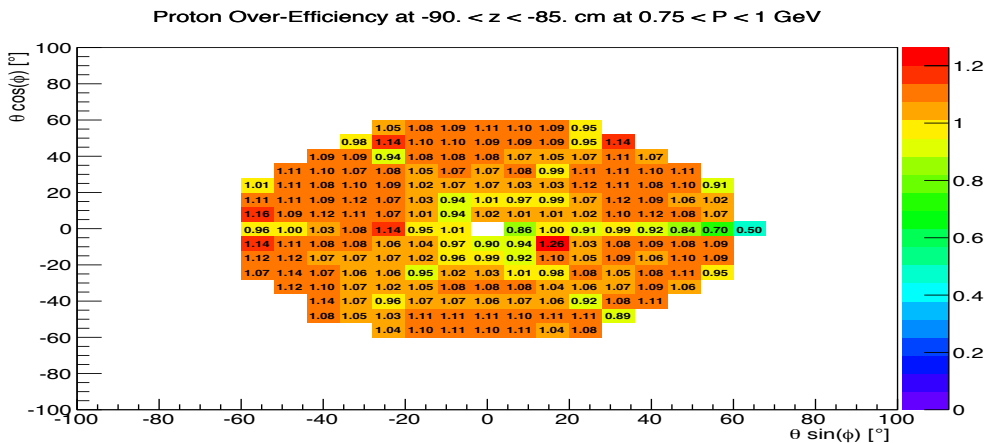


**Figure 112:**  $\theta \cos \phi$  vs.  $\theta \sin \phi$  plot showing the over-efficiency of simulating the proton with z-vertex  $z \in [-90, -85]$  cm and momentum  $p \in [0.75, 1]$  GeV from a 2 charged track reaction.

## 6.2 Comparison of Data to Known Cross Sections

Various cross sections have been extracted using the g12 data set, all showing consistent results when compared with prior CLAS measurements if available, such as the  $\omega$ , the  $\Lambda$ , as well as  $\pi^0$ . In particular, the  $\omega$  cross section results(FSU) , measured using  $\gamma p \rightarrow p \pi^+ \pi^- (\pi^0)$ , are presented here and compared with the g11 results and are consistent across the g12 photon energy range. Although some disagreements do show up at particular kinematic bins, it's safe to say that g12 does not have an overall normalization issue.

Figures 113 and 114 show the differential cross sections for the reaction:  $\gamma p \rightarrow p \omega$ , based on the dominant decay mode:  $\omega \rightarrow \pi^+ \pi^- \pi^0$ . For this analysis, we have selected events with two positively-charged tracks for the proton and the  $\pi^+$  as well as one negatively-charged track for the  $\pi^-$ . The selection has used runs 56520 - 56572, 56573 - 56594, and 56608 - 56646 (Table 3), which were *event-sorted* according to **2-2pos1neg\_not\_1ckaon1ctrk** (Section 3.2). The analyzed run ranges comprise all g12-events that require in the trigger at least three charged tracks in three different sectors but were not subjected to *pre-scaling* to enhance events with high photon energies. This removed an additional layer of complication for studying normalization issues.

For the  $\omega$  events, the standard eloss corrections but tuned momentum corrections to the proper shape of the pull distributions in the kinematic fitting of the reaction:  $\gamma p \rightarrow p \pi^+ \pi^-$  (no missing particle). (For these particular results, the g12 beam energy correction is not applied) After all initial kinematic corrections, the three-track events were then subject to 1C kinematic fitting imposing energy and momentum conservation as well as requiring a missing  $\pi^0$  in the reaction; events have then been selected with a confidence-level (CL) cut of 0.001 which essentially only demands fit convergence. In the final step,  $\omega \rightarrow \pi^+ \pi^- \pi^0$  events were identified in the invariant  $\pi^+ \pi^- \pi^0$  mass. The signal and background separation was achieved by applying the Q-value method which assigns a quality factor to each event indicating the likelihood for the event to be signal. The high efficiency of this method justifies the relatively small CL cut. At this point, we have not yet applied the fiducial cuts discussed in this note. However, we do not expect any significant impact on our final results.

For the differential cross sections, the  $\omega$  yields have been determined for 50-MeV wide energy bins and 20 bins in the corresponding angular distributions (of the  $\omega$  in the overall center-of-mass system). Shown in Figs. 113 and 114 is the energy range 1.50 - 3.80 GeV, along with the ratio distribution in Fig. 115. The angular distributions of the ratios are also shown in 116 and 117. The angular distributions of the  $\omega$  production were acceptance corrected by studying the reaction in GEANT-based simulations. These acceptance corrections include a simulation of the geometrical trigger configuration requiring three different tracks in three different sectors. We have compared normalized and acceptance-corrected  $\omega$  yields from the production runs (at 60 nA) as well as single-sector runs (at 24 nA) and observed a near perfect agreement over the full run range used in this analysis. From this we conclude that the current and trigger corrections are under control. The full energy range for the  $\omega$  cross sections, obviously, will be discussed by the corresponding analysis note of this particular results by FSU.

In terms of the photon multiplicity, at 60-65nA of the production current, about  $87 \pm 1\%$  of the data has only one photon in the same time bucket chosen for the event, around 12% has exactly two photons, and approximately 1% has more than two photons. This has a slight beam energy dependence, however, the variance is on the percent level. The photon multiplicity must be addressed since it is significant. One can correct the cross sections, if those events with multiple photons are all included in their analyses and the photon was chosen randomly, or they were all excluded. However, one can also address this issue by looping over all photons, and that would not require additional corrections. Since this correction depends on the preference of the individuals, we do not prescribe this as a universal procedure by itself.

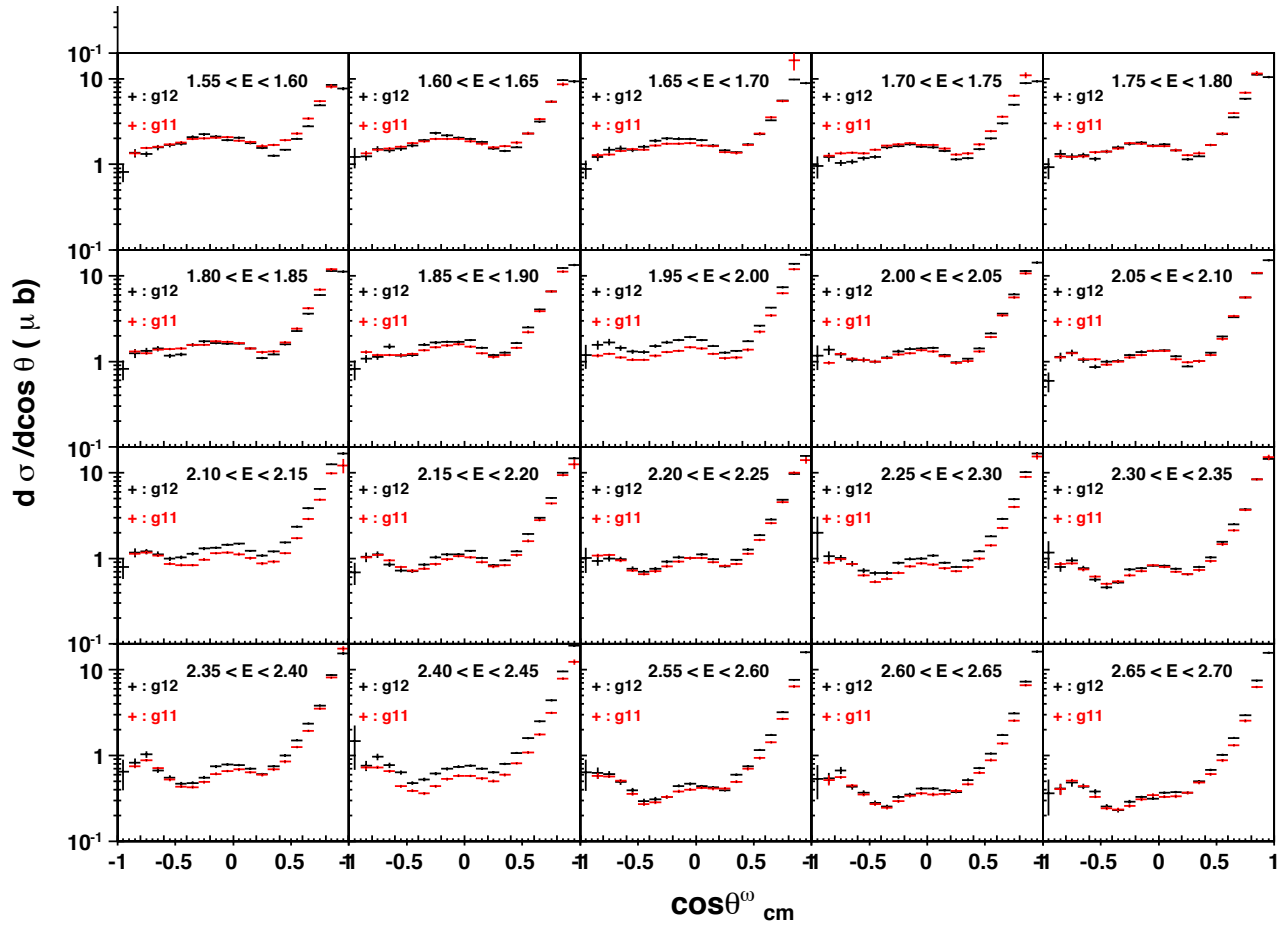


**Figure 113:** Differential cross sections for the reaction  $\gamma p \rightarrow p \omega$  based on the dominant decay mode  $\omega \rightarrow \pi^+ \pi^- \pi^0$  with a beam energy from 1.55 to 2.7 GeV, compared to g11 (red).

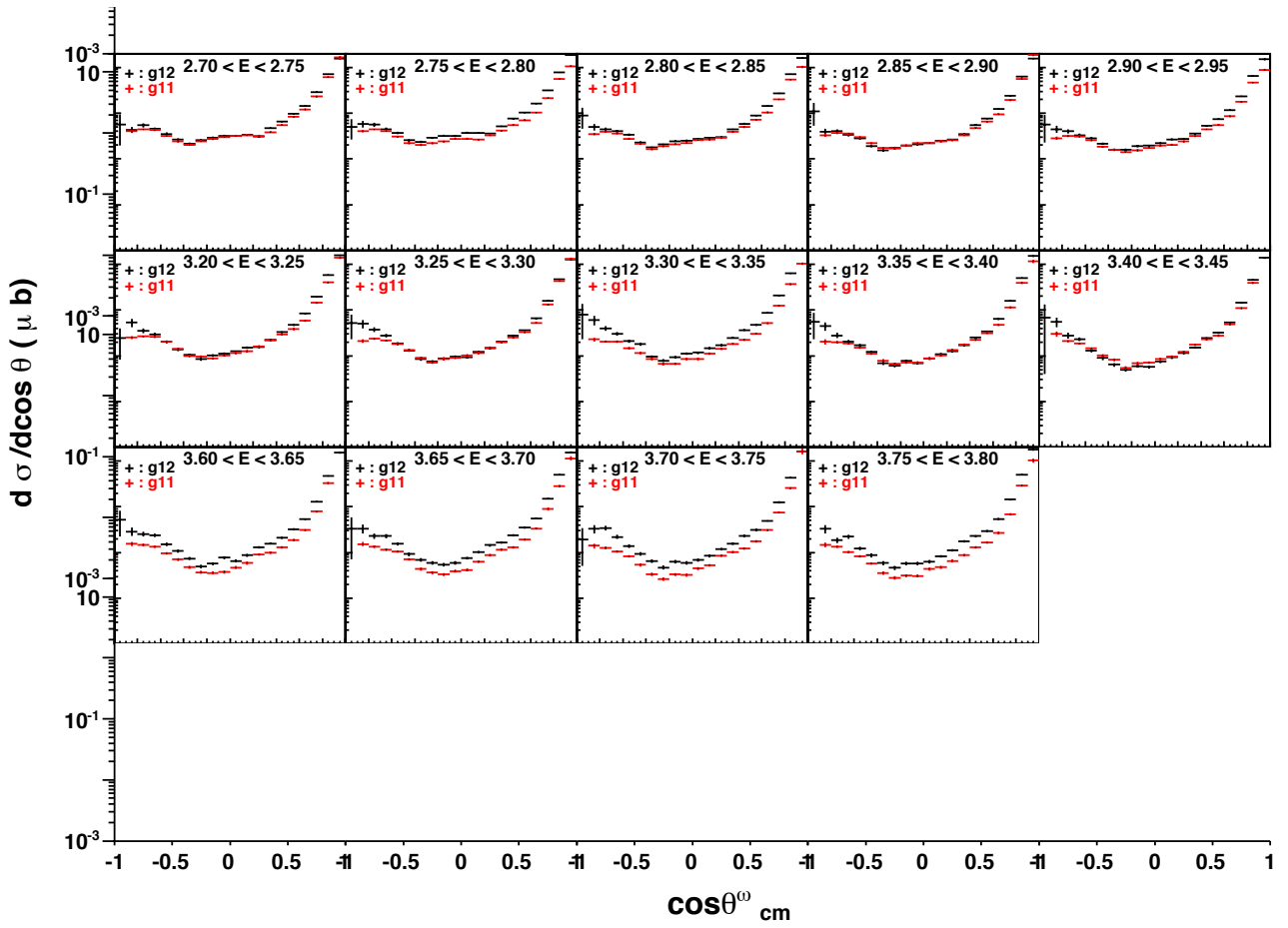


**Figure 114:** Differential cross sections for the reaction  $\gamma p \rightarrow p \omega$  based on the dominant decay mode  $\omega \rightarrow \pi^+ \pi^- \pi^0$  with a beam energy from 2.75 to 3.8 GeV. Comparison to g11 is in red.

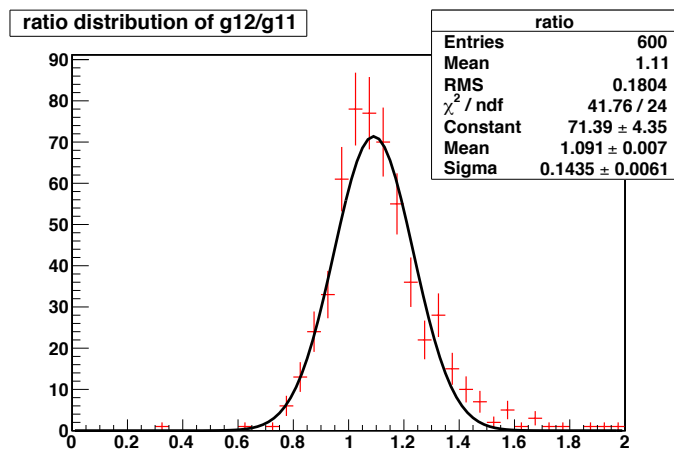


**Figure 115:**  $g_{12}/g_{11}$   $\omega$  cross section ratio distribution for the data shown in Figs. 113 and 114.

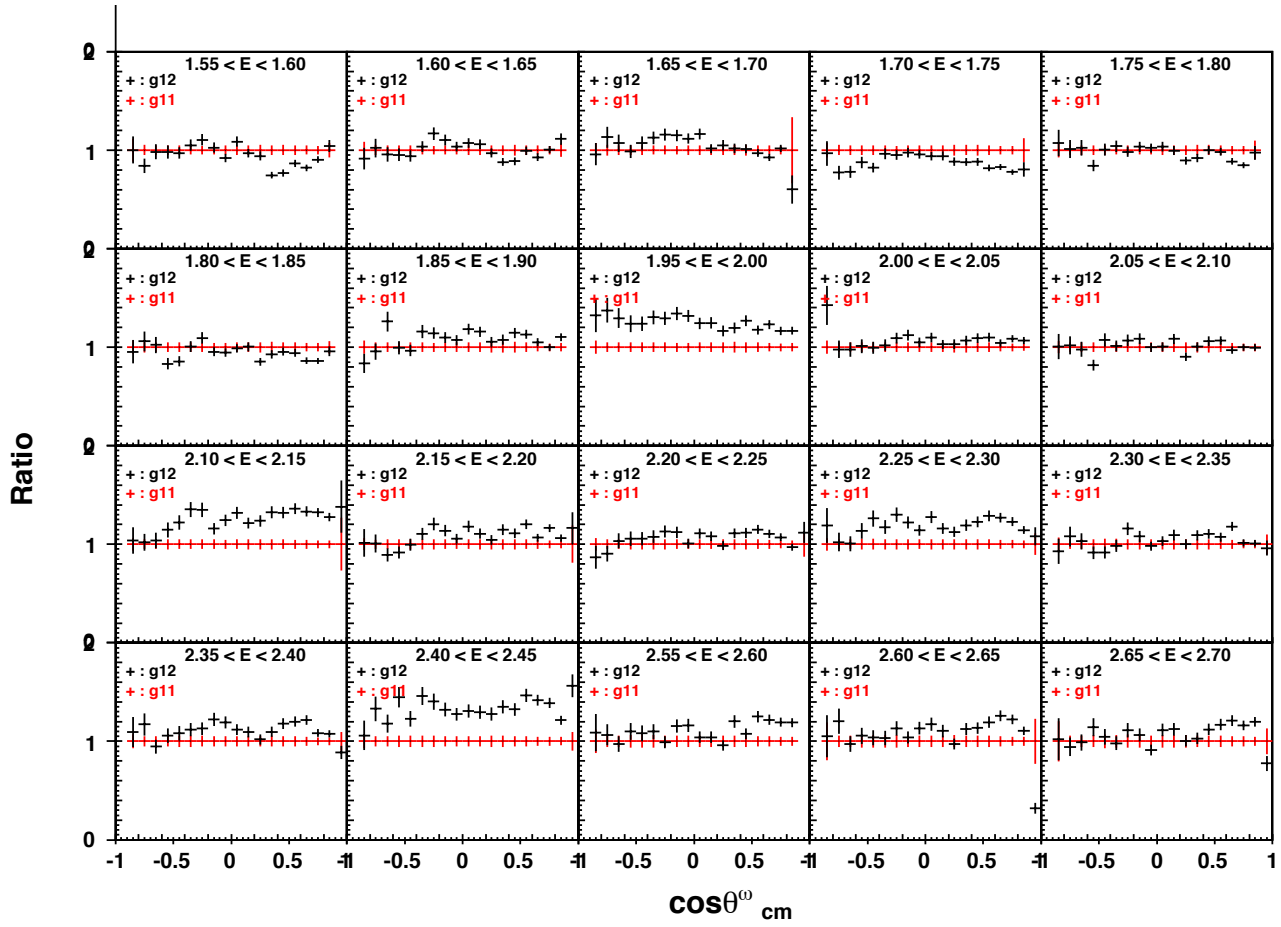


**Figure 116:** Ratio of the  $\omega$  (g12 divided by g11) differential cross sections for the reaction  $\gamma$  p  $\rightarrow$  p  $\omega$  based on the dominant decay mode  $\omega \rightarrow \pi^+ \pi^- \pi^0$  with a beam energy from 1.55 to 2.7 GeV.

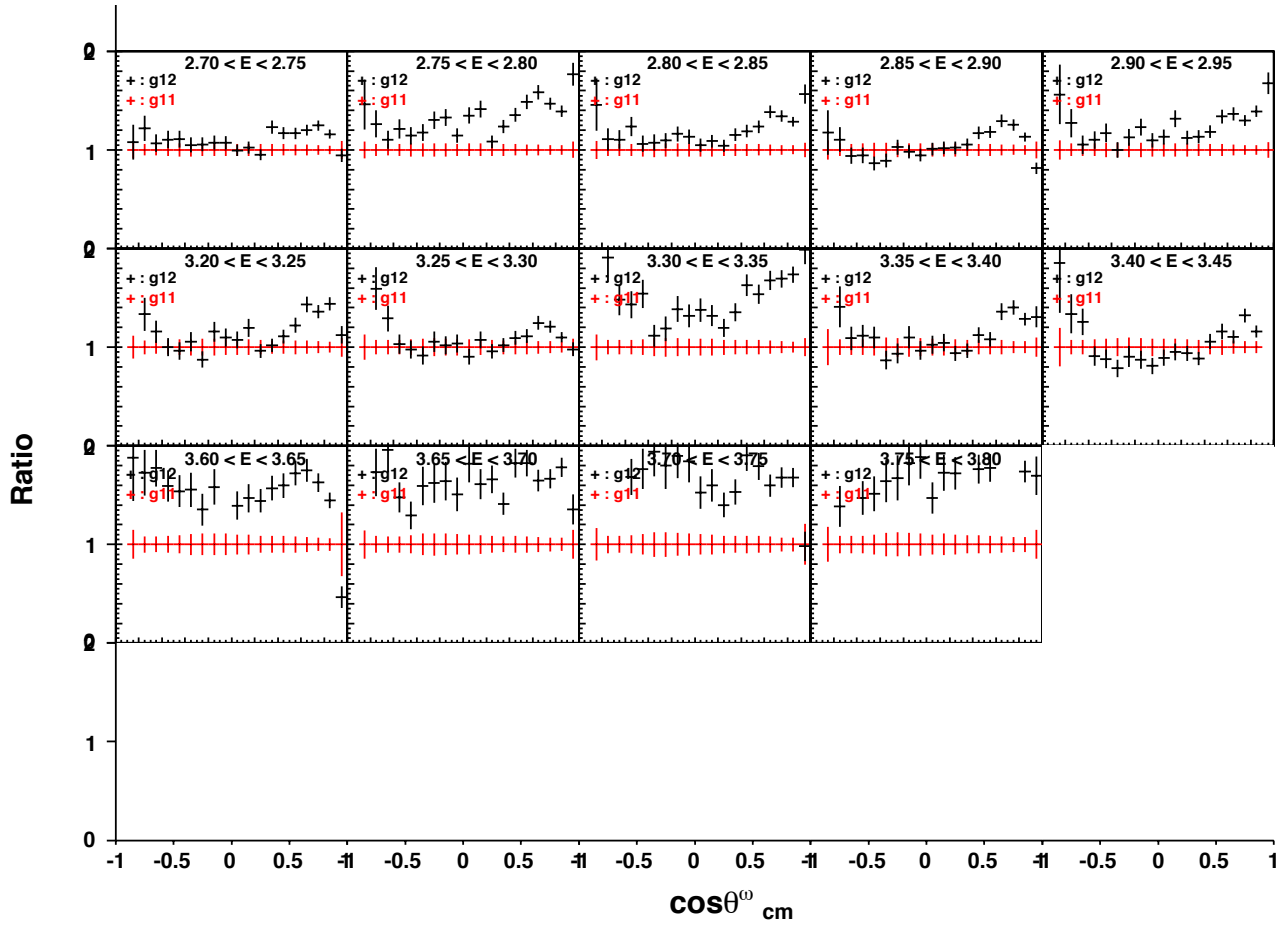


**Figure 117:** Ratio of the  $\omega$  (g12 divided by g11)differential cross sections for the reaction  $\gamma$  p  $\rightarrow$  p  $\omega$  based on the dominant decay mode  $\omega \rightarrow \pi^+ \pi^- \pi^0$  with a beam energy from 2.75 to 3.8 GeV.

The  $\Lambda(1115)$  differential cross section was measured and compared to the  $g11a$  results shown in Figs. 118 and 119 with the pull distribution in Fig. 120. The  $g12$  data employed tight timing and fiducial cuts to minimize systematic uncertainty at the expense of larger statistical uncertainty and very low statistics at high energy and large angle.

In this analysis,

$$\gamma p \rightarrow [\Lambda] K^+ \rightarrow p \pi^- K^+ \quad (21)$$

was simulated with a  $t$ -slope off the  $K^+$  set to unity. The divisions in polar angle were fine enough so that the acceptance was approximately linear in each bin. All three final state particles ( $p \pi^- K^+$ ) were reconstructed and the trigger was modeled to require two particles to be in two different sectors for the high-energy part of the tagger and three particles in three different sectors for the low-energy part of the tagger. Additionally, the tagger was populated with noise generated from the data using gpp's -A option (see Sec. 5.2, page 97). An associated start counter hit was required for each final-state particle and a timing cut against the RF was set to  $\pm 3\sigma$ .

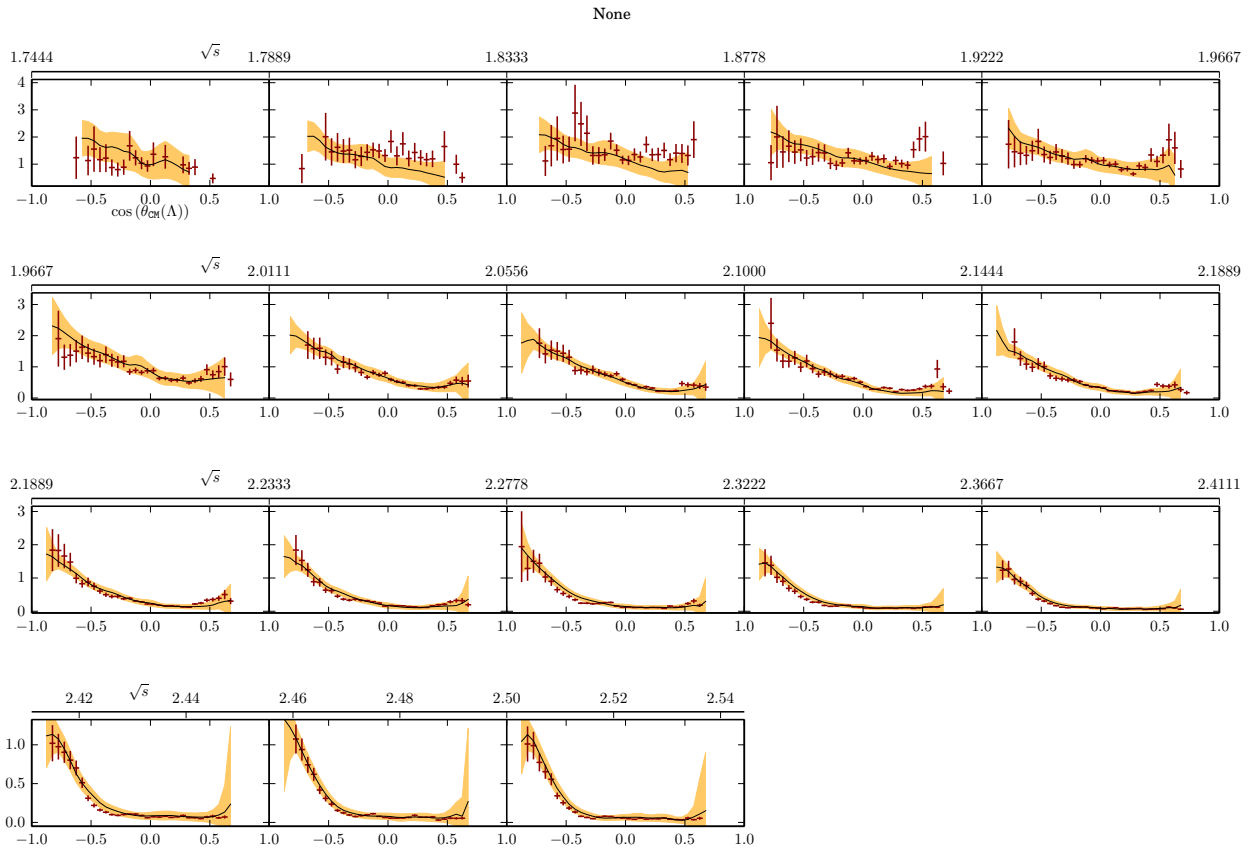


**Figure 118:** Differential cross section of  $\Lambda K^+$  photoproduction in red with a comparison to  $g11a$  with the black line and yellow band at  $3\sigma$  of their quoted statistical uncertainty.

The  $\pi^0$  differential cross-section, shown in Figs. 121 and 122, was measured in the reaction

$$\gamma p \rightarrow p [\pi^0] \rightarrow p e^+ e^- [\gamma] \quad (22)$$

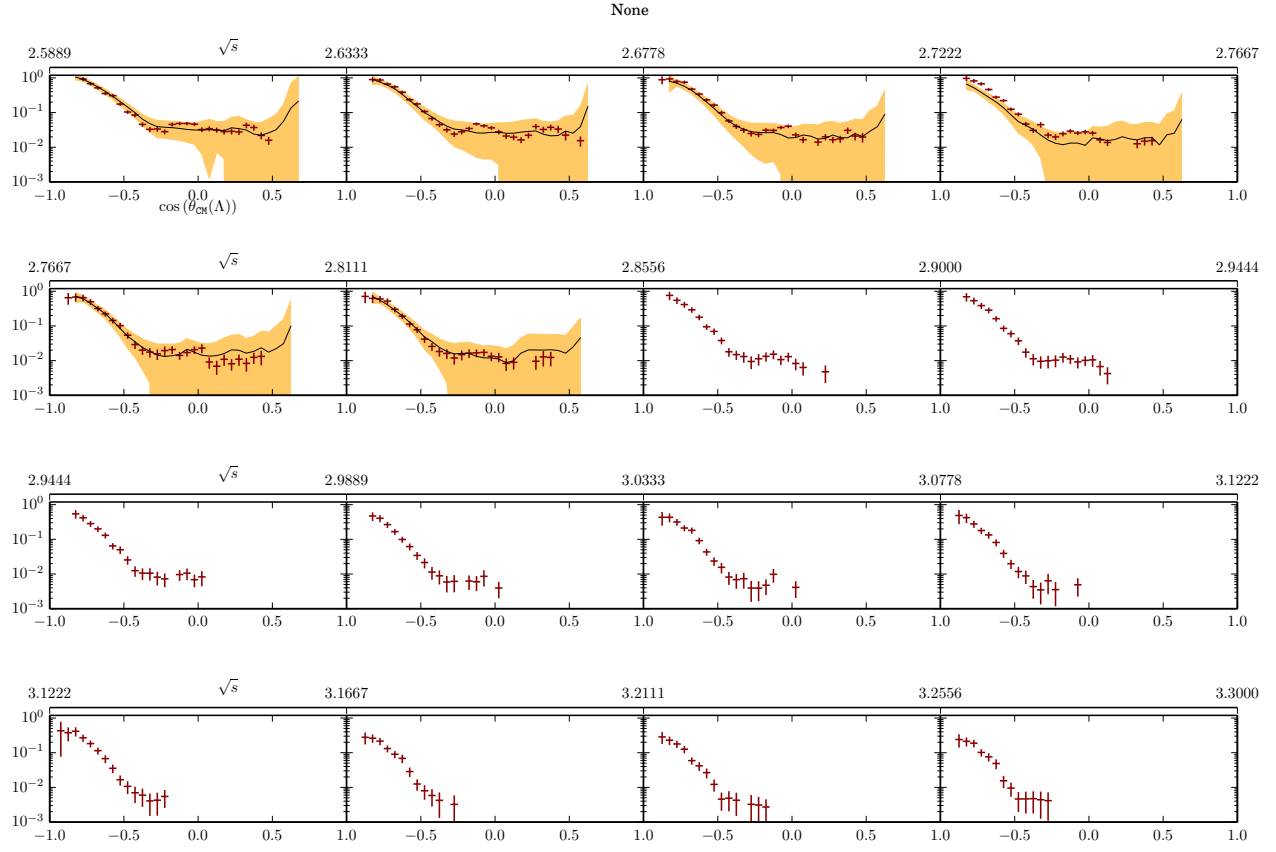


**Figure 119:** Differential cross section of  $\Lambda K^+$  photoproduction in red with a comparison to  $gIIa$  with the black line and yellow band at  $3\sigma$  of their quoted statistical uncertainty.

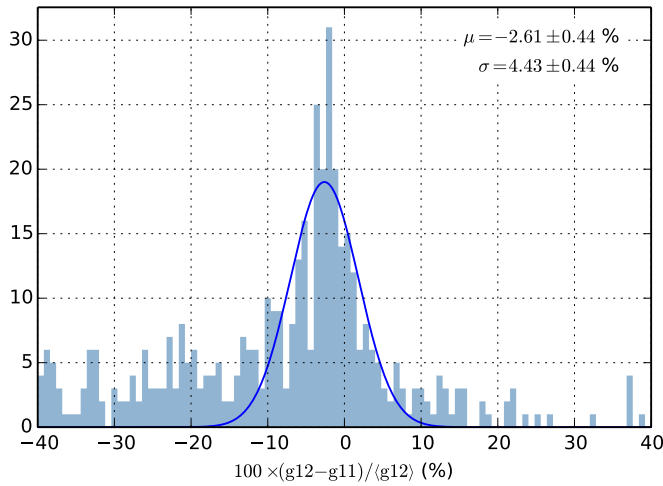


**Figure 120:** Pull distribution against the  $gII$  data shown in Figs. 118 and 119.

where the detected final state particles were one proton, one positron and one electron, while the final state photon was identified through kinematic fitting. The pull distribution against  $g1c$  data is shown for this data in Fig. 123. For the identification of the leptons, where the incident photon beam energy was less than 3.6 GeV, the use of the trigger configuration 6 (see Table 3 on page 6) was employed. To ensure proper simulation of trigger configuration 6, a trigger model was used which mimicked the discrimination of low voltage from the Cherenkov and Electromagnetic calorimeter PMT's. Simulation was performed using PLUTO++ to generate phasespace of 22. All incident beam photons that were within 2.004 ns of the timed particles were analyzed, meaning if an event had 2 or more incident beam photons that were in time with the detected particles within 2.004 ns, then each photon was analyzed as a separate event along with the quantities of the detected particles.

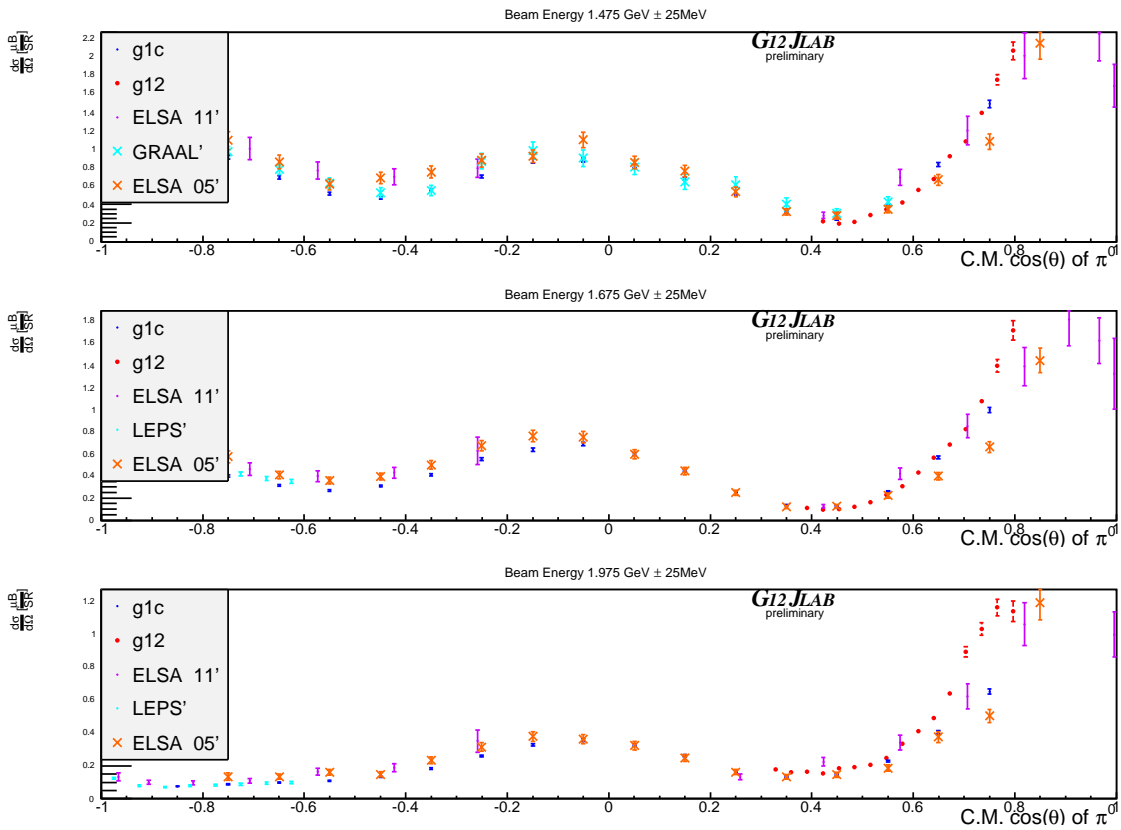


**Figure 121:** Differential cross section of the  $\pi^0$  up to a beam energy of approximately 2 GeV, using the lepton decay channel.

To summarize, the  $g12$  data set does not show any significant beam-intensity-dependent inefficiency, and the overall normalization, when all corrections documented in this note are applied, can be validated by the consistency between the cross sections such as  $\omega$ ,  $\pi^0$  and  $\Lambda$  when compared with prior results. Table 27 shows a list of various contributions to the overall systematic uncertainty which should be quoted in virtually every analysis using  $g12$  data.

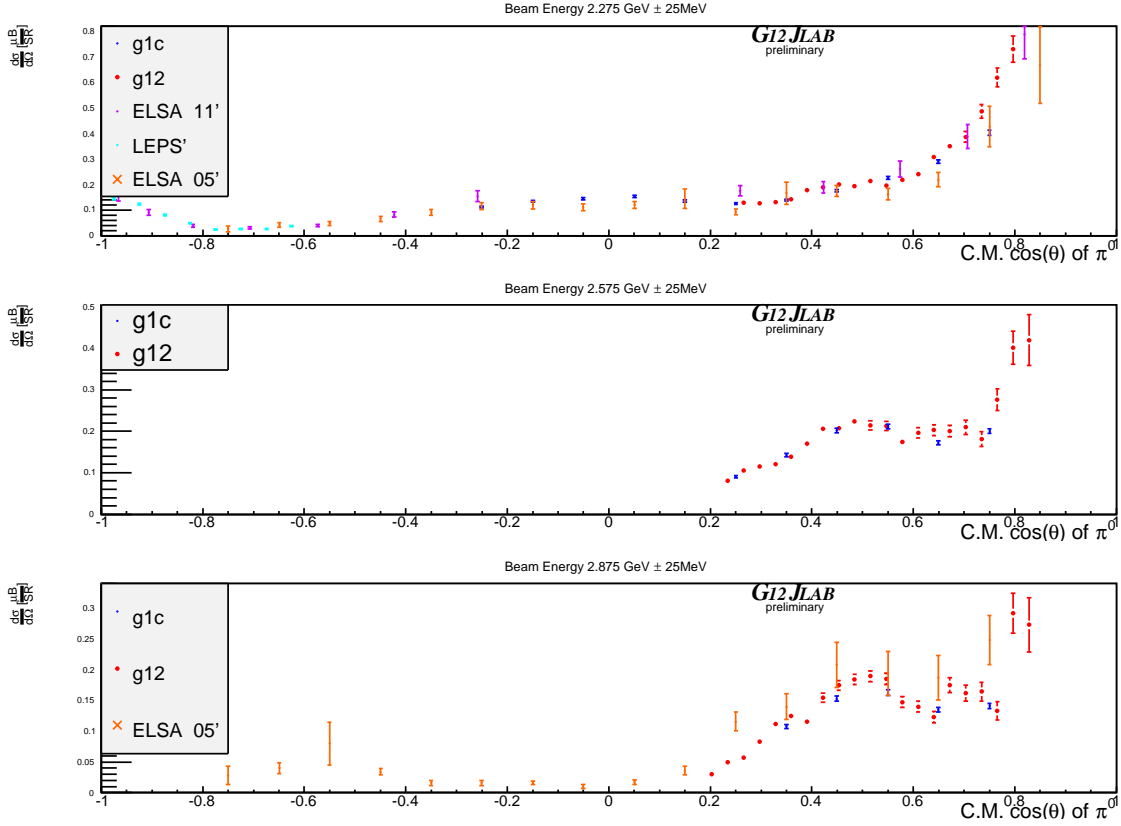


**Figure 122:** Differential cross section of the  $\pi^0$  starting from a beam energy of approximately 2 GeV, using the lepton decay channel.

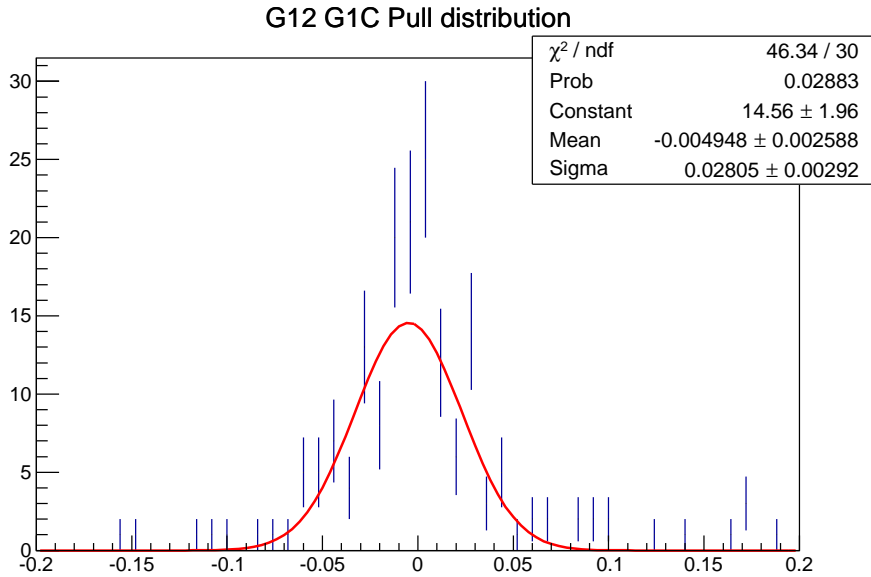


**Figure 123:** Pull distribution for g12/g1c comparison of data shown in Figs. 121 and 122.

**Table 27:** List of systematic uncertainties for  $g12$ . Fiducial selection is only approximate and should be calculated for each specific topology or analysis. The normalization uncertainty is the average of the systematic shifts seen in the three differential cross section results shown in this section.

Source	% Uncertainty
Sector by Sector	5.9
Flux	1.7
Per-Track Inefficiency	3.0
Beam Polarization	3.3
Target	0.5
$z$ -vertex	0.4
Fiducial Selection	$\sim 2.4$
Normalization Uncertainty	1.8

## References

- [1] Craig Bookwalter. “A Search for Exotic Mesons in  $\gamma p \rightarrow \pi^+ \pi^+ \pi^- n$  with CLAS at Jefferson Lab”. PhD thesis. Florida State University, 2012.
- [2] Diane Schott. “A Search for an Exotic Meson in the  $\gamma p \rightarrow \Delta^{++} \pi^- \eta$  Reaction”. PhD thesis. Florida International University, 2012.
- [3] C. W. Salgado and D. P. Weygand. “On the Partial-Wave Analysis of Mesonic Resonances Decaying to Multiparticle Final States Produced by Polarized Photons”. In: *Physics Reports* 537 (1 Apr. 2014), pp. 1–58.
- [4] P. Eugenio et al. *Search for New Forms of Hadronic Matter in Photoproduction*. Tech. rep. CLAS Analysis Proposal PR04-005, 2003.
- [5] D. Weygand et al. *Study of Pentaquark States in Photoproduction off Protons*. Tech. rep. CLAS Analysis Proposal PR04-017, 2004.
- [6] W. Chen et al. *The  $\gamma p \rightarrow \pi^+ n$  Single Charged Pion Photoproduction*. Tech. rep. CLAS Analysis Proposal PR08-003, 2008.
- [7] John T. Goetz. “ $\Xi$  Hyperon Photoproduction from Threshold to 5.4 GeV with the CEBAF Large Acceptance Spectrometer”. PhD thesis. University of California Los Angeles, 2010.
- [8] Mukesh Saini. “Search for New and Unusual Stangonia using CLAS”. PhD thesis. Florida State University, 2013.
- [9] Jason Bono. “First Time Measurements of Polarization Observables for the Charged Cascade Hyperon in Photoproduction”. PhD thesis. Florida International University, 2014.
- [10] Michael C. Kunkel. “Photoproduction of  $\pi^0$  on hydrogen with CLAS from 1.1 GeV - 5.45 GeV using  $e^+ e^- \gamma$  decay”. PhD thesis. Old Dominion University, 2014.
- [11] Shloka Chandavar. “Photoproduction of Scalar Mesons Using the CEBAF Large Acceptance Spectrometer (CLAS)”. PhD thesis. Ohio University, 2015.
- [12] R. Bradford and R.A. Schumacher. “Liquid Hydrogen Density in the G1C CLAS Cryotarget”. In: *CLAS-NOTE* (2002-003).
- [13] X. Zheng. *LD2 target thickness analysis for EG2*. [https://userweb.jlab.org/~xiaochao/eg2/main\\_072503.ps](https://userweb.jlab.org/~xiaochao/eg2/main_072503.ps). 2003.
- [14] P. et al Klaer. “Spin-polarized photoelectrons resonantly excited by circularly polarized light from a fractional Ag film on GaAs(100)”. In: *Phys. Rev. B* 88 (21 Dec. 2013), p. 214425. doi: [10.1103/PhysRevB.88.214425](https://doi.org/10.1103/PhysRevB.88.214425).
- [15] Haakon Olsen and L. C. Maximon. “Photon and Electron Polarization in High-Energy Bremsstrahlung and Pair Production with Screening”. In: *Phys. Rev.* 114 (3 May 1959), pp. 887–904. doi: [10.1103/PhysRev.114.887](https://doi.org/10.1103/PhysRev.114.887).
- [16] B. Mecking et al. “The CEBAF large acceptance spectrometer (CLAS)”. In: *Nucl. Instrum. Methods A* 503, 513 (2003).
- [17] D. S. Carman. “2002-018 (unpublished)”. In: *CLAS Note* (2002).

- [18] Strauch and Berman *et al.* “Beam-Helicity Asymmetries in Double-Charged-Pion Photoproduction on the Proton”. In: *Phys. Rev. Lett.* 95 (16 Oct. 2005), p. 162003. doi: [10.1103/PhysRevLett.95.162003](https://doi.org/10.1103/PhysRevLett.95.162003).
- [19] E. Pasyuk. “Energy loss corrections for charged particles in CLAS”. In: (2007).
- [20] K.A. Olive et al. “The Review of Particle Physics”. In: *Chin. Phys. C* 38.090001 (2014). (Particle Data Group).
- [21] M. Dugger, P. Roy, and N. Walford. “Momentum corrections for  $\pi^+$  and protons in g9b data”. In: (2013).
- [22] R. Nasseripour et al. “Search for Modification of Vector Meson Properties in Nuclei”. In: *CLAS-NOTE* (2006).
- [23] E. Pasyuk J. Ball. “Photon Flux Determination Through Sampling of “out-of-time” Hits with the Hall B Photon Tagger”. JLab. Jan. 2005.